THESIS

UNDERSTANDING CARBON NANOPARTICLE TRANSPORT IN SATURATED POROUS MEDIA: THE INFLUENCE OF DISSOLVED ORGANIC MATTER

Submitted by

Tyler Gilkerson

Department of Geosciences

In partial fulfillment of the requirements

For the Degree of Master of Science

Colorado State University

Fort Collins, Colorado

Spring 2020

Master's Committee:

Advisor: William Sanford

Yan Li
Michael Ronayne

Copyright by Tyler Craig Gilkerson 2020

All Rights Reserved

ABSTRACT

UNDERSTANDING CARBON NANOPARTICLE TRANSPORT IN SATURATED POROUS MEDIA: THE INFLUENCE OF DISSOLVED ORGANIC MATTER

Nanoparticles (NPs), or objects with all dimensions between 1 nanometer (nm) and 100 nm, are ubiquitous in atmospheric, aquatic, and terrestrial settings. The ability to engineer NPs and utilize their unique size-dependent physicochemical properties has resulted in the rise of nanotechnology as a prominent component of twenty-first century research and industry. Engineered nanoparticles (ENPs) commonly reach groundwater systems after being released to the environment as byproducts of various human goods and activities or agents of groundwater remediation. While ENPs are released at a significant rate, the transport mechanisms controlling their fate are poorly understood. Furthermore, some ENPs are toxic and capable of facilitating contaminant transport and bioavailability. Evaluating the ways in which ENPs are transported in groundwater is critical to effectively managing and regulating their release to and removal from natural systems.

A NP with characteristics of an ideal groundwater tracer would enable powerful investigations of NP fate and transport processes in saturated porous media. Similar to applied conservative solute tracers, this NP could also be used to estimate aquifer and groundwater flow parameters. Recent studies indicate engineered carbon nanoparticles (CNPs) are ideal groundwater tracer candidates. With diameters from 2 nm to 5 nm, CNPs are nearly spherical carbon cores functionalized with a fluorescent coating. Additionally, these NPs are nontoxic, environmentally benign, highly hydrophilic, inexpensive, easily synthesized, and conveniently detected at low concentrations. Owing to their size, stability, and near-zero zeta potential, CNPs are transported conservatively

and mostly unimpaired in saturated porous media under diverse environmental conditions (e.g. dual-porosity and positively charged sediment; high temperatures, pressures, and salinities; and alongside other ENPs and common solute tracers). Nonetheless, CNP transport in natural settings cannot be adequately understood without evaluating the influence of dissolved organic matter (DOM).

This study executed four one-dimensional column experiments to investigate the influence of DOM on CNP transport in homogeneous coarse-grained silica sand. To compare CNP transport to that of a conservative solute tracer, CNPs were transported alongside bromide (Br) in each column experiment. Solution pHs of 4 and 7 were each maintained for two experiments to further evaluate the influence of DOM. Breakthrough curves (BTCs) were generated from effluent samples and analyzed via temporal moment methods (TMMs) and inverse modeling using the CXTFIT 2.1 code. These analyses enabled estimation of CNP and Br mass recovery and transport parameters such as velocity, retardation, and dispersion. Such estimates indicated that CNP transport and Br transport were similar and mostly conservative under all experimental conditions. However, while apparently enhanced by DOM, CNP transport was slightly retarded by reversible equilibrium and nonequilibrium adsorption to silica sand in all experiments.

These findings generally agree with previous studies suggesting CNPs will transport conservatively in natural groundwater systems. While CNP transport is slightly impaired relative to Br under these experimental conditions, this research suggests CNPs could be used to elucidate how less-mobile nanoscale objects are transported in saturated porous media. Therefore, CNPs are tentatively regarded as ideal NP tracers.

ACKNOWLEDGEMENTS

Attempting to overcome the many challenges I faced as a graduate student would have been a futile effort without the assistance provided by my family, friends, Colorado State University (CSU) faculty and staff, donors, and professional mentors. This is especially true regarding the support of my wife, Megan, my best (four-legged) friend, Cassie, and my parents. I will forever be grateful for the physical and psychological support they, as well as my siblings, grandparents, and friends, have supplied over the last three years.

Earning this graduate degree was also made possible by the many talented academic and administrative professionals at CSU. I am especially thankful for the time and guidance I received from my advisor, Dr. Bill Sanford, and committee members, Drs. Yan "Vivian" Li and Mike Ronayne. I am also grateful for the outstanding education and opportunities to develop professional skills that were provided by the Department of Geosciences and its many respectable faculty. Additionally, previous research by Charlie King; laboratory assistance by Connor Kounnas; and analytical support and deionized water offered by CSU's AIRIE and NREL laboratories and Central Instrument Facility were critical to this study. Finally, this research would not have been possible without the financial support of gracious donors like Bob Stollar, Jeff Ware, the AEG Foundation, and the Martin L. Stout Fund.

TABLE OF CONTENTS

LIST OF TABLES

LIST OF FIGURES

LIST OF SYMBOLS

Abbreviations

1D	one-dimensional
2D	two-dimensional
3D	three-dimensional
ADE	advection-dispersion equation
Br	bromide
BTC	breakthrough curve
CNP	carbon nanoparticle
DI	deionized (water)
DLVO	Derjaguin-Landau-Verwey-Overbeek (theory)
DOM	dissolved organic matter
E1	Experiment 1
E2	Experiment 2
E3	Experiment 3
E4	Experiment 4
ENP	engineered nanoparticle
HDPE	high-density polyethylene
NO	nano-object
NP	nanoparticle
PPHA	Pahokee Peat humic acid
PZC	point(s) of zero charge
TEM	transmission electron microscope
TMM	temporal moment method

Units

Å	angstrom
cm	centimeter

°C	degree Celsius
g	gram
m	meter
min	minute
mL	milliliter
mm	millimeter
mM	millimolar
mV	millivolt
µm	micron
nm	nanometer
ppm	part(s) per million
PV	pore volume
RFU	relative fluorescence unit

Variables and Parameters

A	column cross-sectional area
α	first-order kinetic rate coefficient
α_L	longitudinal dispersivity
β	partitioning coefficient for nonequilibrium adsorption
C	effluent or standard concentration
C_0	influent concentration
C_1	tracer concentration adsorbed to equilibrium sites
C_2	tracer concentration adsorbed to kinetic sites
CEC_{aws}	cation-exchange capacity for acid-washed sand
CEC_s	cation-exchange capacity for water-rinsed sand
d	diameter
D	dispersion coefficient
D_m	molecular diffusion coefficient
D_p	nanoparticle diffusion coefficient
f	fraction of equilibrium adsorption sites

γ	zero-order production term
ID	inside diameter
k_b	Boltzmann constant
K_d	empirical distribution constant
L	length
L_s	length of saturated sand within column
λ_{em}	emission wavelength
λ_{ex}	excitation wavelength
m_0	zeroth temporal moment
m_1	first temporal moment
m_2	second temporal moment
m_{exc}	excess sediment mass
m_i	temporal moment of i^{th} order
m_{ini}	initial sediment mass
m_{inj}	injected tracer mass
m_s	mass of sand added to column
M_1	normalized first temporal moment
MPV	(number of injected influent) mobile pore volumes
MSE	mean squared error
μ	viscosity
μ_2	second central moment (variance of tracer arrival times)
μ_d	first-order decay coefficient
ω	mass transfer coefficient for kinetic adsorption
P	Peclet number
PV	(number of injected influent) pore volumes
ϕ	average matrix porosity
ϕ_g	gravimetric matrix porosity
ϕ_v	volumetric matrix porosity
%MR	percent mass recovery
Q	volumetric flow rate

r^2	coefficient of determination
R	retardation factor
RSD	relative standard deviation
ρ_b	bulk matrix density
ρ_s	material density of silica
s_k	tracer concentration adsorbed to kinetic sites
SA	surface area
SD	standard deviation
t	column experiment time
t_{ar}	average tracer arrival time
t_c	corrected effluent timestamp
t_{eff}	elapsed transport time from column outlet to fraction collector sampling outlet
t_f	final sample time
t_i	experiment start time when dual-tracer solution reaches column inlet
t_{inf}	elapsed transport time from valve to column inlet
t_{inj}	dual-tracer solution injection time
t_j	uncorrected timestamp of j^{th} sample
T	temperature
T_d	dimensionless time
v	average tracer transport velocity
v_w	average pore water velocity
V	volume
V_p	pore volume at the point of saturation
V_P	total column pore volume
V_t	total volume of saturated sand in column
V_T	total volume of packed column
V_w	volume of water
x	distance from column inlet
X	dimensionless length

LIST OF EQUATIONS

CHAPTER 1: INTRODUCTION

Introduction to Nano-Objects

Based on the International System of Units' definition for the prefix "nano," one nanometer (nm) is equal to one-billionth (10^{-9}) of a meter (m) (ASTM Standard E2456). Accordingly, nanoscale objects, or nano-objects (NOs), are often defined as materials with at least one dimension ranging from 10^{0} nm to 10^{2} nm (Figure 1.01) (Hochella Jr., 2002; US Environmental Protection Agency, 2007; Christian et al., 2008; Klaine et al., 2008; Auffan et al., 2009; Hofmann and von der Kammer, 2009; Frimmel and Delay, 2010; British Standards Institution, 2011; Hartland et al., 2013; de Mello Donegá, 2014; Njuguna et al., 2014; Boverhof et al., 2015; Kumar and Kumbhat, 2016; National Science and Technology Council, 2016; Khan et al., 2019). In comparison, atomic sizes and light wavelengths are commonly reported in angstroms (Å), a unit equal to 10^{-10} m or 10^{-1} nm. Prior to their discrete recognition, NOs were indirectly discussed in the context of colloids.

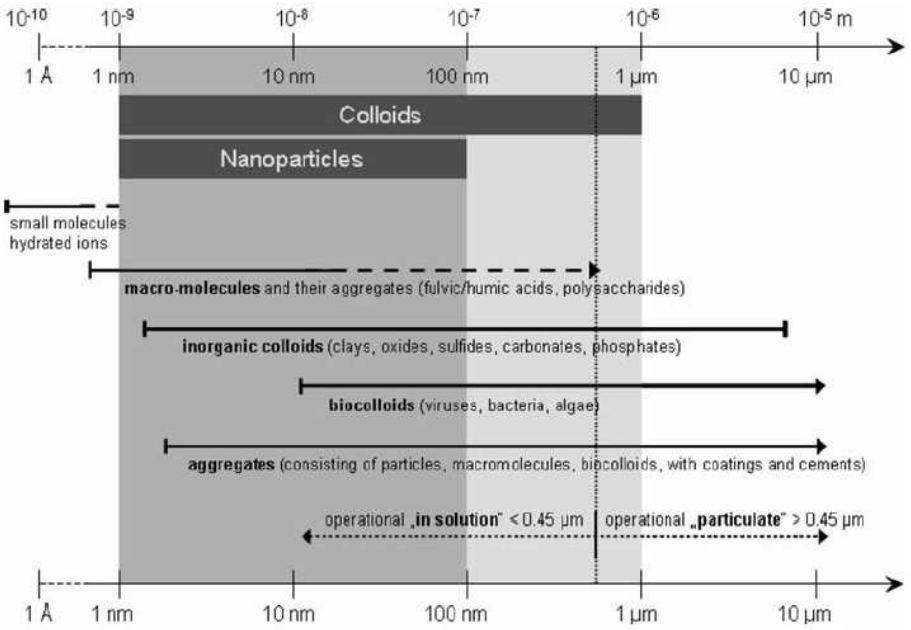

Figure 1.01: Size of common natural nanoparticles and colloids. Vertical dashed line represents division between dissolved and particulate matter (0.45 microns (µm)) (from Christian et al., 2008).

The term “colloid” is defined as a two-phase system composed of solid, liquid, or gas particles with at least one dimension between 10^0 nm and 10^3 nm, or 10^0 micron, dispersed in a different solid, liquid, or gas medium (Figure 1.01) (Christian et al., 2008; International Union of Pure and Applied Chemistry, 2014). Aerosols and aqueous dispersions, or dispersions of solid particles in air and water, respectively, are the two most common natural colloidal systems (Christian et al., 2008). Hereafter, the term “dispersion” will be used in the context of NOs and nanoparticles (NPs).

Size Considerations

Chemical, mechanical, optical, magnetic, and (or) electrical NO properties are commonly distinct from those exhibited by their macroscale counterparts. In addition to shape and composition, these unique nanoscale properties are fundamentally related to their size (Figure 1.02) (Hochella Jr., 2002; de Mello Donegá, 2014; Njuguna et al., 2014; Kumar and Kumbhat, 2016; Khan et al., 2019). However, a given object with any number of dimensions less than 10^2 nm does not necessarily exhibit properties that are distinguishable from bulk matter. Depending on its

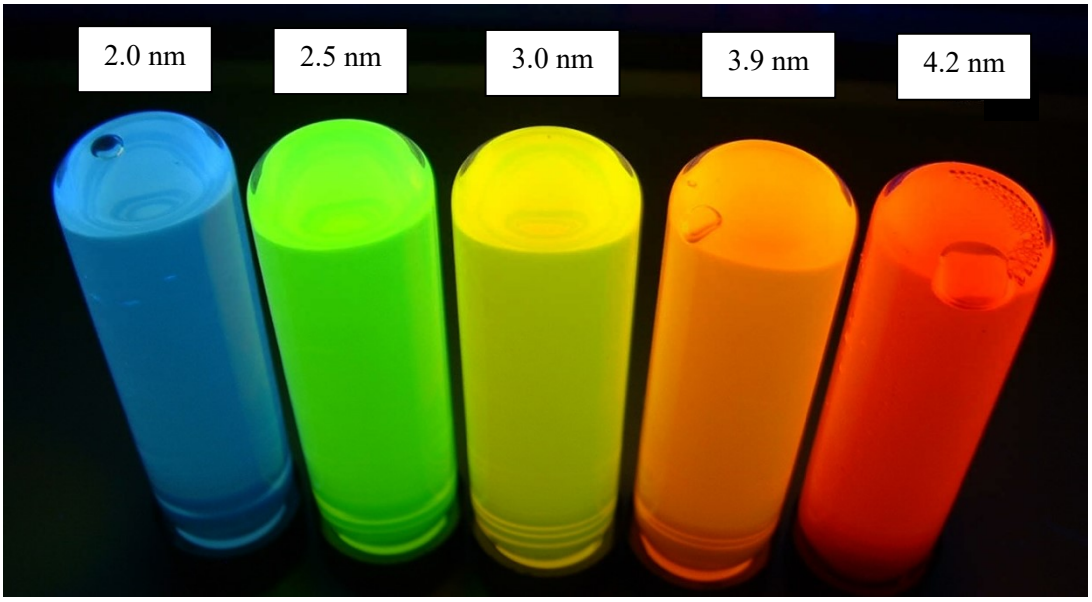

Figure 1.02: Size-dependent fluorescence of CdSe NPs with diameters ranging from 2.0 nm to 4.2 nm (modified from Wong, 2013).

composition and nanoscale dimensions, a NO has at least one critical length at which unique properties are observed (Gilbert and Banfield, 2005; Auffan et al., 2009; de Mello Donegá, 2014; Njuguna et al., 2014). Thus, the commonly accepted NO size range is somewhat arbitrary but represents a convenient and quantifiable geometric definition and most likely encompasses any given NO's critical length(s) (Klaine et al., 2008; Boverhof et al., 2015).

Unique size-dependent NO properties cannot be explained by Newtonian physics and are attributed to quantum effects and (or) relatively large surface-area-to-volume ratios (Gilbert and Banfield, 2005; Roduner, 2006; Klaine et al., 2008; Hartland et al., 2013; de Mello Donegá, 2014; Njuguna et al., 2014; Kumar and Kumbhat, 2016). Quantum effects relate to the negligible influence of gravity on NOs relative to electromagnetic forces and increased electron confinement (Gilbert and Banfield, 2005; Hartland et al., 2013; de Mello Donegá, 2014; Kumar and Kumbhat, 2016). Describing NO behavior requires consideration of quantum mechanics since these objects are physically more analogous to atoms than bulk masses (Kumar and Kumbhat, 2016).

As a NO's size and number of atoms increase, the proportion of surface atoms decreases (Figure 1.03). Surface atoms have fewer atomic neighbors than their internal counterparts. Consequently, atoms comprising a NO have greater binding energies than atoms within a compositionally analogous macroscale object (Roduner, 2006; de Mello Donegá, 2014). Therefore, NOs are often electrically charged and more reactive and mobile than larger-scale materials (Hartland et al, 2013; de Mello Donegá, 2014; Njuguna et al., 2014). Similar to quantum effects, the influence of high surface area varies by physicochemical property and depends on a given NO's shape and composition (de Mello Donegá, 2014; Kumar and Kumbhat, 2016).

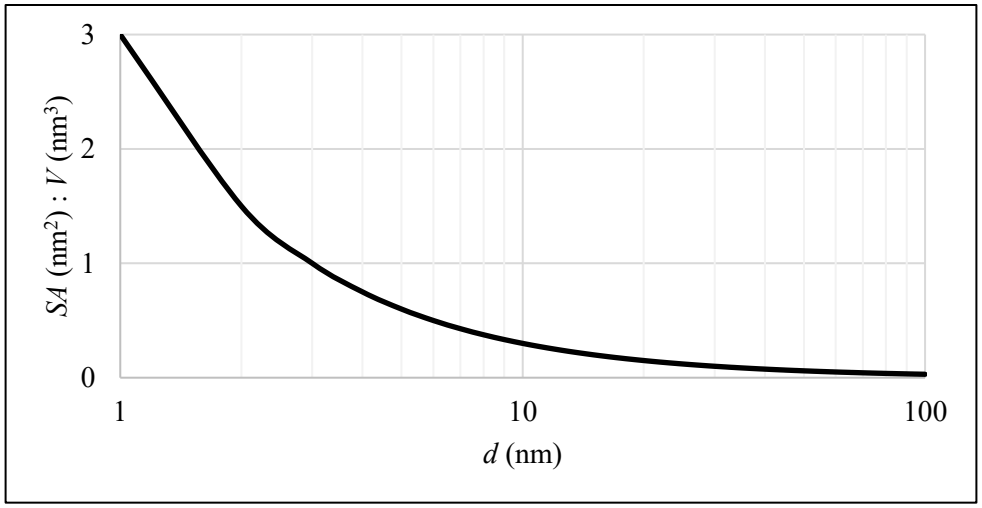

Figure 1.03: Relationship between NP diameter (*d*) and the ratio of NP surface area (*SA*) to volume (*V*). Note the logarithmic scale of the x-axis.

Classifying NOs

One-, two-, and three-dimensional (1D, 2D, and 3D, respectively) NOs exist in numerous sizes and shapes. One-dimensional NOs, such as nanofilms, nanoplates, and nanocoatings, have one external dimension (i.e. thickness) between 10^0 nm and 10^2 nm. Nano-objects with two external nanoscale dimensions, or 2D NOs, include nanorods, nanofibers, and nanotubes (e.g. asbestos fibers, nanopore filters, and carbon nanotubes) (British Standards Institution, 2011; de Mello Donegá, 2014; Njuguna et al., 2014). With all dimensions between 10^0 nm and 10^2 nm, 3D NOs include NPs and quantum dots (British Standards Institution, 2011; ASTM Standard E2456; de Mello Donegá, 2014; Njuguna et al., 2014; Kumar and Kumbhat, 2016).

Compositionally, NOs can be categorized as organic, inorganic, carbonaceous, or composite. Organic NOs are mostly biological and include polymers, dendrimers, proteins, nucleic acids, viruses, enzymes, bacteria, nanocarbohydrates, lipids, and humic substances (Nowack and Bucheli, 2007; Klaine et al., 2008; Hartland et al., 2013; de Mello Donegá, 2014; Kumar and Kumbhat, 2016; Khan et al., 2019). Inorganic NOs are commonly composed of metals (e.g. copper,

gold, iron, platinum, silver, etc.) and metal oxides (e.g. aluminum oxide, cerium dioxide, iron oxides, silicon dioxide, titanium dioxide, zinc oxide, etc.). This compositional class also includes ceramics, volcanic fumes, smog, forest fire emissions, and nanominerals (e.g. clays, zeolites, sea salt aerosols, nanoscale desert sands, asbestos fibers, etc.) (Gilbert and Banfield, 2005; Nowack and Bucheli, 2007; Hochella Jr. et al., 2008; Klaine et al., 2008; Kumar and Kumbhat, 2016; Khan et al., 2019). Carbonaceous, or carbon-based, NOs include carbon nanotubes, fullerenes, graphene, carbon nano-onions, carbon nanofibers, carbon black, nanodiamonds, and carbon nanoparticles (CNPs) (US Environmental Protection Agency, 2007; Klaine et al., 2008; Kumar and Kumbhat, 2016; Khan et al., 2019). Composite NOs are combinations of two or more organic, inorganic, and carbonaceous nanoscale constituents (US Environmental Protection Agency, 2007).

Nanoparticles in the Environment

The ability to design and create NOs with desired attributes has established a prominent and auspicious role for nanotechnology in twenty-first century research and industry (Njuguna et al., 2014; Bergmann et al., 2015; Boverhof et al., 2015; National Science and Technology Council, 2016). However, the significant rate at which NOs are being produced and released to natural settings without a firm understanding of associated environmental impacts highlights a critical need for NO-focused research across ecologic, toxicologic, atmospheric, geologic, and hydrologic disciplines (Hofmann and von der Kammer, 2009; Petosa et al., 2010; Keller et al., 2013; Njuguna et al., 2014). While myriad scientific investigations and technological advancements involve NOs of many sizes, shapes, and compositions, NPs will be discussed exclusively hereafter.

Natural NPs

Nanoparticles have existed naturally throughout Earth's history and are ubiquitous in atmospheric, aquatic, and terrestrial settings (Hochella Jr., 2002; Nowack and Bucheli, 2007; Hochella Jr. et al., 2008; Klaine at al., 2008; Frimmel and Delay, 2010; Aiken et al., 2011; British Standards Institution, 2011; Njuguna et al., 2014; Bergmann et al., 2015; Boverhof et al., 2015; National Science and Technology Council, 2016; Khan et al., 2019). In fact, natural NPs are regarded as fundamental components of life and planetary development (Nowack and Bucheli, 2007; Kumar and Kumbhat, 2016). As products of erosion, mineral formation, forest fires, volcanic eruptions, acid mine drainage, photochemical reactions, and biological processes, natural NPs include nanoscale dust and soot, clays and other nanominerals, metals and metal oxides, cellulose fibers, organic acids, proteins, enzymes, viruses, and bacteria (Nowack and Bucheli, 2007; Hochella Jr. et al., 2008; Klaine et al., 2008; de Mello Donegá, 2014; Njuguna et al., 2014; Kumar and Kumbhat, 2016).

Natural NPs play key roles in abiotic and biotic processes such as soil development, clay swelling, mineral growth and weathering, faulting, atmospheric carbon dioxide regulation, cloud formation, organismal sensing, biomineralization, camouflaging, mating, and superhydrophobic self-cleaning (Hochella Jr., 2002; Wilson et al., 2005; Hochella Jr. et al., 2008; Klaine et al., 2008; Niessner, 2010; Hartland et al., 2013; Kumar and Kumbhat, 2016) Environmentally, natural NPs are especially important due to their abilities to facilitate metal and contaminant transport and uptake of nutrients and toxins (Hochella Jr., 2002; Hochella Jr. et al., 2008; Klaine et al., 2008; Hartland et al., 2013). Nonetheless, science is far from fully explaining how natural NPs interact with Earth systems (Nowack and Bucheli, 2007; Hochella Jr. et al., 2008; Hofmann and von der Kammer, 2009).

Anthropogenic NPs

Anthropogenic NPs include engineered NPs (ENPs) and incidental NPs. While incidental NPs are produced unintentionally, ENPs are those designed and manufactured to serve one or more particular functions (Nowack and Bucheli, 2007; British Standards Institution, 2011). The rise of nanotechnology and the ability to exploit nanoscale-dependent properties has inspired the use of ENPs throughout agricultural, automotive, construction, cosmetic, electronic, energy, environmental, medical, and other industries (Lee et al., 2010; Coelho et al., 2012; Gruère, 2012; Keller et al., 2013; Njuguna et al., 2014; National Science and Technology Council, 2016; Khan et al., 2019). In 2010, between 260,000 and 309,000 metric tons of ENPs were produced globally. Based on maximum production estimates, roughly 70% of these ENPs were used in coatings, paints, and pigments; electronics and optics; cosmetics; and energy and environmental industries (Figure 1.04) (Keller et al., 2013).

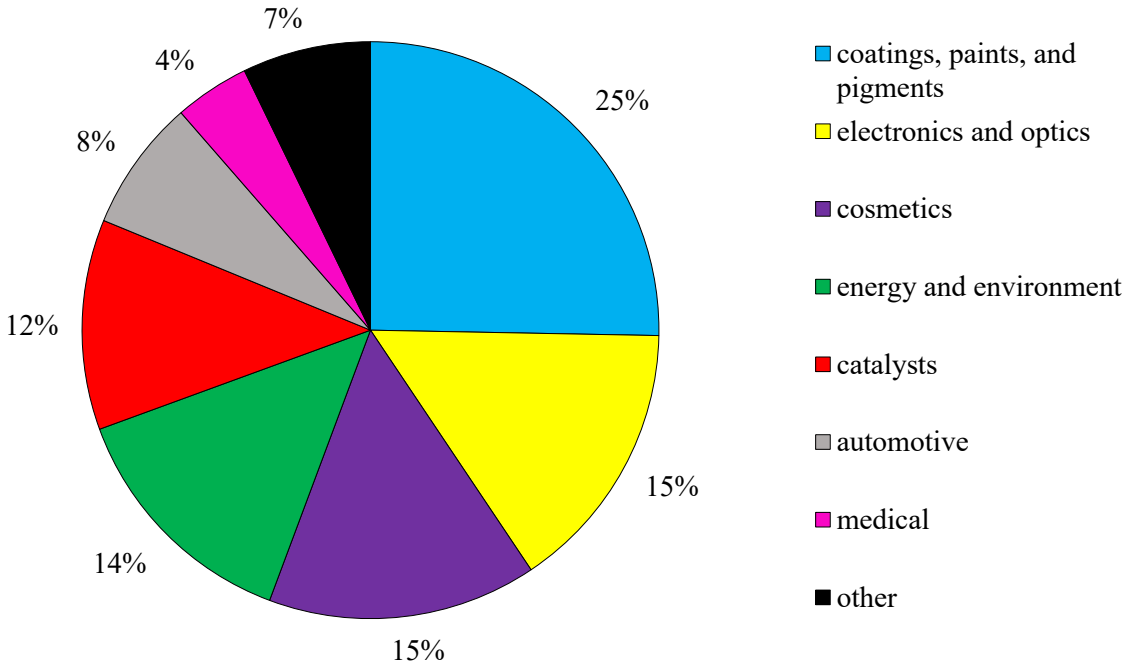

Figure 1.04: Applications of most-commonly produced (globally, by mass) ENPs in 2010 (Keller et al., 2013).

Silicon dioxide, titanium dioxide, iron and iron oxides, aluminum oxide, and zinc oxide represent over 90% of the ten most-commonly produced ENPs in 2010 (Figure 1.05) (Keller et al., 2013). Silicon dioxide and titanium dioxide NPs are commonly used in coatings and paints to increase material strength and weathering resistance. Silicon dioxide NPs are also used to clarify beverages and insulate buildings, while titanium dioxide NPs are incorporated in solar cells as photocatalysts. Titanium dioxide and zinc oxide NPs are widely used in cosmetics and other consumer goods for their antimicrobial properties and ability to block ultraviolet radiation (Klaine et al., 2008; Keller et al., 2013; Kumar and Kumbhat, 2016). Aluminum oxide NPs are incorporated in polymers, coatings, cutting tools, windows, and flooring to increase abrasion resistance; automotive catalytic

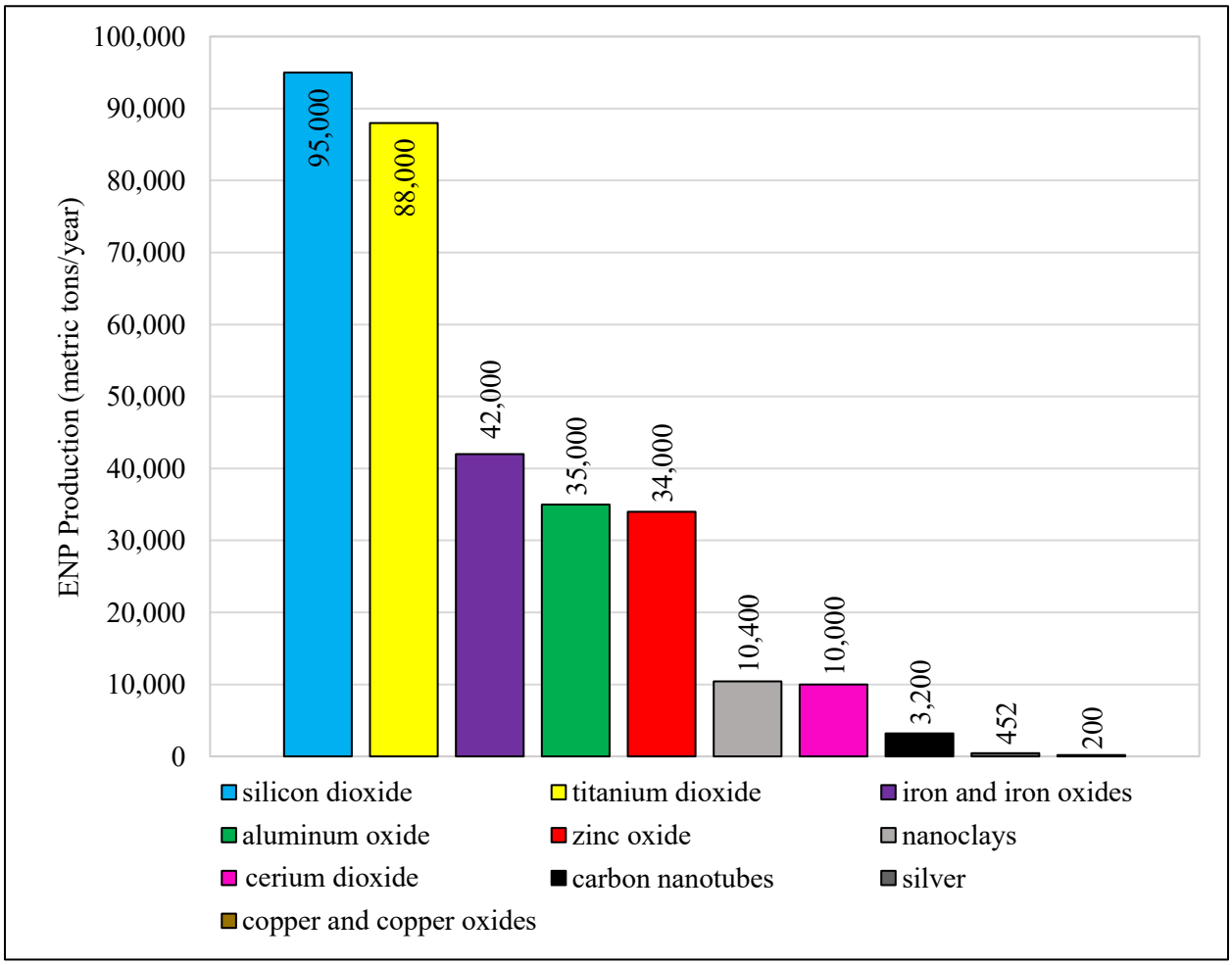

Figure 1.05: Ten most-commonly produced (globally, by mass) ENPs in 2010 (Keller et al., 2013).

converters as catalysts; and slurries for polishing electronic and optical components. Iron and iron oxide NPs are commonly used as paint and cosmetic pigments and in magnetic recording tapes (Kumar and Kumbhat, 2016). Additionally, ENPs (i.e. zero-valent iron, silicon dioxide, titanium dioxide, and silver NPs) are employed to remediate contaminated water resources and treat potable water supplies (Skubal et al., 2002; Pitoniak et al., 2005; US Environmental Protection Agency, 2007; Fu et al., 2013; Prathna et al., 2018).

Release of Anthropogenic NPs

Incidental NPs are those inadvertently released to terrestrial, aquatic, and atmospheric systems as byproducts of goods and human activities. Such processes as combustion of fossil and renewable fuels, smoking, cooking, paint degradation, mechanical abrasion, and textile washing represent nonpoint sources of incidental NPs (Gilbert and Banfield, 2005; Nowack and Bucheli, 2007; Wagner et al., 2014; Kumar and Kumbhat, 2016). Incidental NPs are also released to the environment from point sources such as wastewater treatment plants, landfills, waste incinerators, fossil fuel power plants, and facilities that manufacture ENPs or products containing NPs (Nowack and Bucheli, 2007; Klaine et al., 2008).

Anthropogenic NPs (i.e. ENPs) are also intentionally introduced to natural systems for designed environmental remediation and water treatment purposes (Nowack and Bucheli, 2007; Keller et al., 2013; Prathna et al., 2018). Reactivity, transport, and sequestration qualities of certain ENPs are being tuned to enable time- and cost-efficient air, soil, and water remediation (Zhang, 2003; US Environmental Protection Agency, 2007; Sánchez et al., 2011). Zero-valent iron NPs are incorporated into permeable reactive barriers to facilitate in situ reduction of aqueous chlorinated hydrocarbons in contaminated groundwater (US Environmental Protection Agency, 2007). These

NPs might also be capable of remediating groundwater and soil contaminated with metals, pesticides, organic dyes, arsenic, nitrate, and dense non-aqueous phase liquid chlorinated hydrocarbons (Zhang, 2003; US Environmental Protection Agency, 2007; Trujillo-Reyes et al., 2014). Furthermore, zero-valent iron NPs are used in wastewater treatment processes to reduce metal and dye releases (Fu et al., 2013). Ultrafiltration of metals, such as copper, could be enhanced by deploying certain chelating dendrimer NPs (Diallo et al., 2005). Composites of nanoscale silicon dioxide and titanium dioxide are effective adsorbents and oxidants of mercury in vapors (Pitoniak et al, 2005). Independently, titanium dioxide NPs are capable of removing dissolved cadmium (Skubal et al., 2002). Additionally, silver NPs are known disinfectants used to treat potable water supplies (Prathna et al., 2018). Aside from environmental remediation and water treatment applications, ENPs can also benefit natural systems when used as fertilizers, water filters, and agents of energy efficiency and environmental sensing (US Environmental Protection Agency, 2007; Raliya et al., 2018).

Environmental Concerns of ENPs

While some ENPs are intentionally introduced to improve environmental conditions, others threaten natural systems that might struggle to coexist with or adapt to their unnatural and (or) toxic properties (Hartland et al., 2013). Due to their enhanced reactivity and mobility, some ENPs are capable of increasing pollutant bioavailability and facilitating contaminant transport (Hochella Jr., 2002; US Environmental Protection Agency, 2007; Hofmann and von der Kammer, 2009; Baumann, 2010). Engineered NPs are also capable of diffusing through and disrupting cell membranes. Furthermore, some ENPs can harm humans and animals by releasing sorbed contaminants, creating reactive oxygen species, and damaging proteins and DNA (Klaine et al., 2008). Certain ENPs with enhanced antimicrobial properties (e.g. silver, titanium dioxide, and

copper NPs) can also impact microorganism communities (Klaine et al., 2008; Trujillo-Reyes et al., 2014).

Humans and animals regularly inhale and ingest NPs, and exposure to ENPs will increase with industrial and domestic applications. Inhalation of certain ENPs can cause respiratory inflammation, emphysema, fibrosis, and cancer. Their ability to translocate throughout organisms can impact immune systems. For example, silicon dioxide and titanium dioxide NPs can decrease viral and bacterial resistance. Accumulation of ENPs containing iron, aluminum, copper, and zinc in nervous systems damages brain cells and can lead to neurodegenerative diseases. Ingestion of certain ENPs might also correspond to lymphatic, circulatory, and gastrointestinal injuries (Kumar and Kumbhat, 2016). Additionally, aluminum oxide and zinc oxide can hinder root elongation in several common vegetable crops (Yang and Watts, 2005; Lin and Xing, 2008). Such threats highlight the need for an improved understanding of ENP environmental fate, transport, and exposure pathways.

Nanoparticle Fate and Transport

Manufacturing, utilizing, and disposing certain products contributes NPs to natural systems. While ENPs are commonly released to air, land, surface water, and groundwater during and following waste incineration and wastewater treatment, most are disposed in landfills (Figure 1.06) (Keller et al., 2013). In the absence of NP-specific containment measures, a portion of landfilled NPs enter natural systems via runoff and leachate infiltration (Cullen et al., 2010). Atmospheric NPs typically deposit on land or water within, at most, days or weeks. These airborne NPs are also inhaled by humans and animals (US Environmental Protection Agency, 2007; Keller et al., 2013). Nanoparticles released to soil and surface water can be transported to groundwater settings via

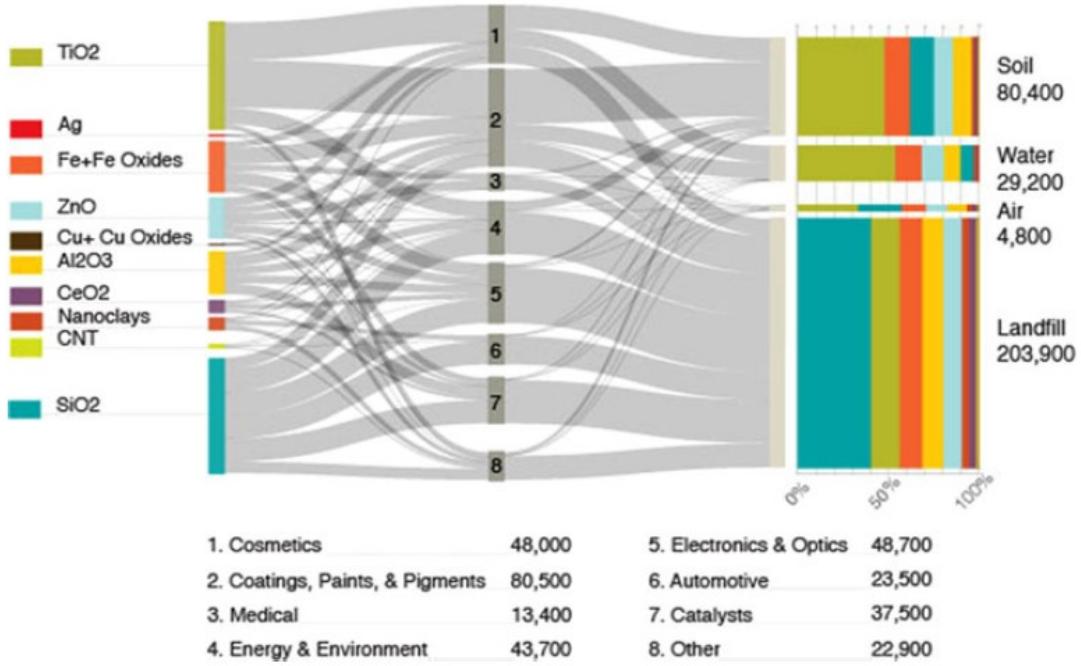

Figure 1.06: Life cycle of ten most-commonly produced (globally, by mass) ENPs in 2010 (Figure 1.05). Relative production amounts are represented by the length of bars on the left side of the figure. Gray flow paths pass through ENPs' respective application zones in route to release or disposal settings on the right side of the figure. The numbers in the middle of the figure correspond to the lower key for estimates of total 2010 production by application area (metric tons per year) (from Keller et al., 2013).

infiltration (US Environmental Protection Agency, 2007). Regardless of the natural system to which they are released, NP transport can be facilitated, retarded, or terminated by natural abiotic or biotic degradation, transformation, consumption, or sorption processes (US Environmental Protection Agency, 2007; Klaine et al., 2008; Petosa et al., 2010; Keller et al., 2013). Ultimately, NP fate is governed by various transport mechanisms that depend on intrinsic NP properties and the transport environment. While understanding potential exposure pathways requires consideration of NP transport in atmospheric, terrestrial, and aquatic settings, NPs will be discussed exclusively in a hydrogeologic context hereafter.

Understanding NP stability, or the degree to which NPs tend to agglomerate and (or) deposit on matrix surfaces, is key to predicting NP fate (Christian et al., 2008; Karathanasis, 2010; Petosa et al., 2010). Nanoparticle stability depends on fluid, matrix, and NP properties that influence surface

charges (Christian et al., 2008). In aqueous dispersions, NP stability can be estimated by measuring zeta potential (Figure 1.07). This voltage potential exists along the diffuse layer's slipping plane, or the boundary between ions that move with a NP and those that remain with the surrounding liquid (Li et al., 2014; Malvern Instruments Limited, 2017). The Stern layer, which also influences NP stability, represents an inner more-strongly bound layer of counterions along the charged NP surface (Christian et al., 2008; Malvern Instruments Limited, 2017). As NPs approach their points of zero charge (PZC), destabilization and agglomeration become more likely (Christian et al.,

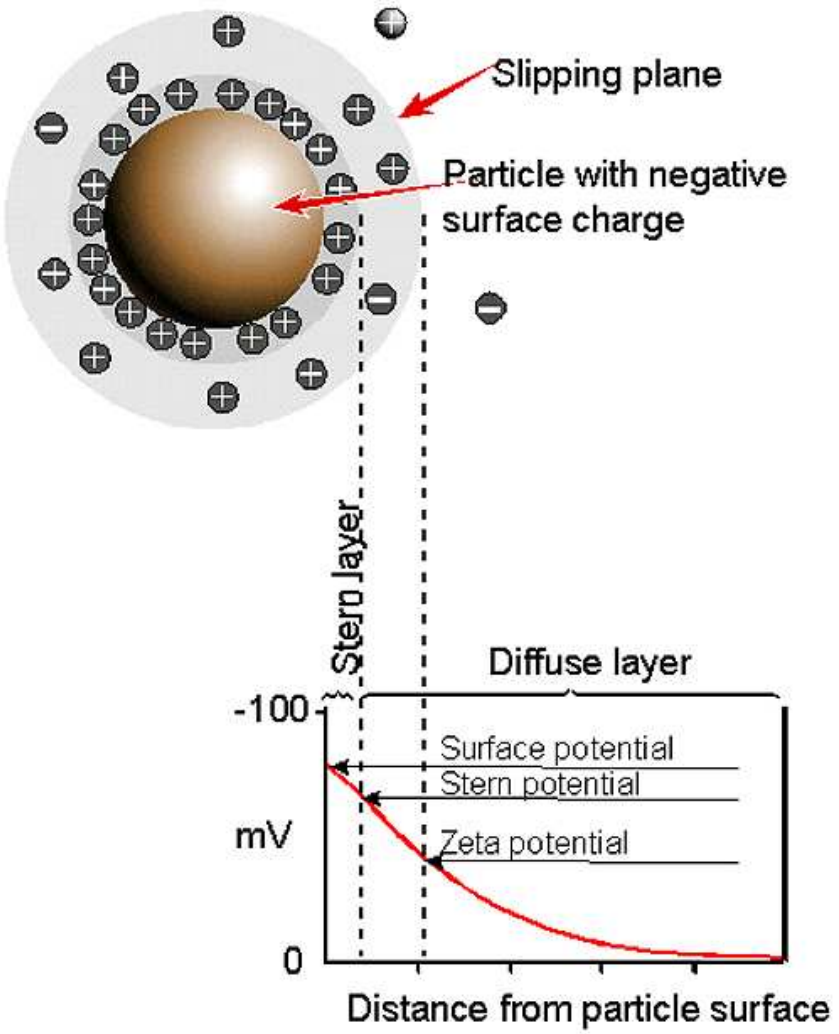

Figure 1.07: Diagram of a charged NP and surrounding Stern and diffuse layers. The dependence of voltage potentials (i.e. surface, Stern, and zeta potentials) on distance from the NP is depicted in the lower plot (from Malvern Instruments Limited, 2017).

1998). However, NPs with zeta potentials less than -30 millivolts (mV) or greater than 30 mV are expected to repel one another and form stable dispersions given certain dispersant conditions (Schwegmann and Frimmel, 2010).

Nanoparticle stability can also be estimated by comparing interfacial forces acting on or created by NPs according to the Derjaguin-Landau-Verwey-Overbeek (DLVO) theory (Grasso et al., 2002; Petosa et al., 2010; Hartland et al., 2013). Based on this theory, NPs in aqueous dispersions are simultaneously attracted to and repelled by other NPs and matrix surfaces (Derjaguin and Landau, 1941; Verwey and Overbeek, 1948; Petosa et al., 2010; Hartland et al., 2013). If the attractive van der Waals forces among NPs or between a NP and a matrix grain exceed the repulsive electrostatic forces, the dispersion is unstable. Consequently, NPs will agglomerate and (or) deposit on matrix grains (Figure 1.08). Otherwise, NP repulsion will be sufficient to maintain a stable dispersion (Petosa et al., 2010; Hartland et al., 2013).

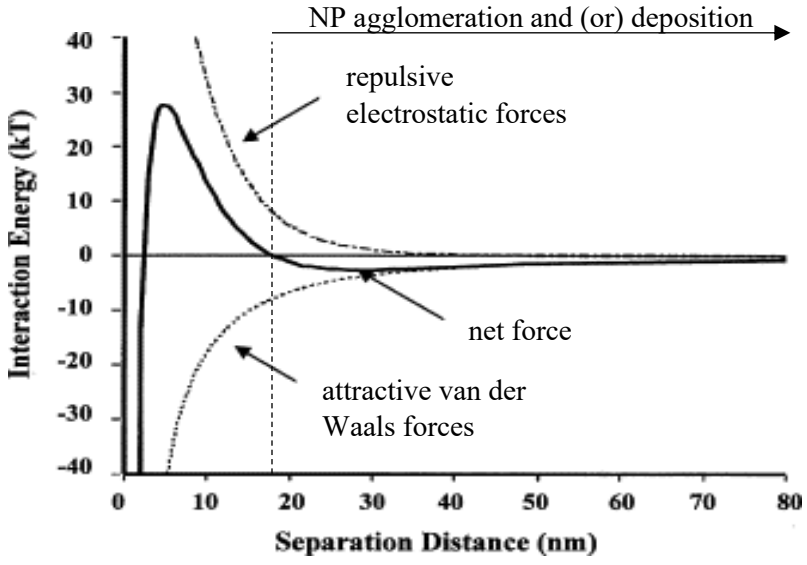

Figure 1.08: Conceptual depiction of NP stability based on DLVO theory. Nanoparticle agglomeration occurs to the right of the vertical dashed line as a result of van der Waals forces exceeding electrostatic forces (modified from Adair et al., 2001).

The magnitudes of these balancing forces are influenced by dispersant ionic strength and pH. As ionic strength increases, repulsive electrostatic forces among NPs decrease and the dispersion becomes less stable (Grasso et al., 2002; Christian et al., 2008; Karathanasis, 2010; Wagner et al., 2014). Near pH 7, most NPs possess negative zeta potentials (Hartland et al., 2013). Therefore, as dispersants acidify below pH 7, NPs generally approach their PZC and become less stable. However, realistic degrees of environmental complexity require consideration of non-DLVO forces such as magnetic forces, hydrogen bonding, steric interactions, and Lewis acid base interactions (Grasso et al., 2002; Petosa et al., 2010; Hartland et al., 2013; Wagner et al., 2014). Stability greatly influences NP mobility and the mechanisms by which NPs are transported (Karathanasis, 2010; Petosa et al., 2010).

Although associated effects are neglected by DLVO theory, the presence of dissolved organic matter (DOM) in saturated porous media often has a critical impact on NP stability and mobility (Chen and Elimelech, 2008; Petosa et al., 2010; Aiken et al., 2011; Wagner et al., 2014). Nanoparticles coated with a nanoscale layer of DOM tend to form stable dispersions (Baalousha and Lead, 2007; Baumann, 2010; Logan, 2012). Furthermore, ENP aggregation and deposition is commonly reduced in saturated porous media containing DOM (Aiken et al., 2011). Humic acid, a common constituent of DOM, generally reduces NP agglomeration by inducing negative surface charges below a NP's PZC. Absent DOM, NPs usually have positive surface charges below their PZC and, therefore, are electrostatically attracted to one another (Christian et al., 2008; Wagner et al., 2014). Increasing humic acid concentrations has shown to enhance steric stabilization of fullerene, carbon nanotube, hematite, and titanium dioxide NPs (Chen et al., 2007; Hyung et al., 2007; Baalousha et al., 2008; Chen et al., 2012). Generally, NP stability and mobility are also enhanced by the presence of DOM by means of electrostatic stabilization (Jekel, 1986; Chen et al.,

2012). Depending on dispersant chemistry, matrix grains coated with organic material can either retard or facilitate NP transport (Chen and Elimelech, 2008). As a bridging agent, DOM is also capable of promoting NP agglomeration (Chen et al, 2007). Despite its common stabilizing effect, reasonably predicting the influence of DOM on NP stability and transport requires consideration of dispersant pH, ionic strength, and DOM composition (Chen and Elimelech, 2008; Christian et al., 2008; Wagner et al., 2014).

Nanoparticles are transported by advection, dispersion, and diffusion (Yao et al., 1971; Elimelech and O'Melia, 1990; Tufenkji and Elimelech, 2004; Petosa et al., 2010). In surface water and fractured bedrock aquifer settings, transport of stable NPs is primarily unimpeded (Hartland et al., 2013). Nanoparticle transport in saturated porous media is commonly retarded or terminated by deposition mechanisms described by colloid filtration theory (Yao et al., 1971; Tufenkji and Elimelech, 2004; Hartland et al., 2013). This theory suggests three transport mechanisms (i.e. interception, sedimentation, and Brownian motion) are responsible for deposition of suspended particles (Yao et al., 1971; Tufenkji and Elimelech, 2004). However, the degree to which these mechanisms retard NP transport relative to average pore water velocity varies (Logan, 2012). Depending on surface reactivities under certain environmental conditions, collisions from interception, sedimentation, or Brownian motion could cause NP adsorption to matrix grains (Yao et al., 1971).

Interception occurs when a particle contacts a matrix grain due to the particle's size instigating such a collision (Yao et al., 1971; Tufenkji and Elimelech, 2004). Based on this concept, larger NPs are more likely to be trapped in or excluded from pore throats than smaller NPs (Logan, 2012; Wagner et al., 2014). Sedimentation occurs when a particle settles on a matrix grain under gravitational forces due to the particle's density exceeding that of the dispersant. Compared to

larger NPs, smaller NPs deposited by sedimentation require lower pore water velocities for re-entrainment. These two transport mechanisms effectively remove micron-scale particles from their streamlines and direct them to surrounding matrix grains (Yao et al., 1971; Tufenkji and Elimelech, 2004). Therefore, while these depositional mechanisms tend to not affect individual stable NPs, agglomerations of unstable NPs are likely to experience interception and sedimentation (Tufenkji and Elimelech, 2004; Klaine et al., 2008).

Brownian motion is the primary driver of deposition for individual stable NPs (Yao et al., 1971; Tufenkji and Elimelech, 2004; Christian et al., 2008; Petosa et al., 2010). Analogous to gaseous diffusion, Brownian motion describes particle diffusion resulting from the random movement of suspended particles as they collide with surrounding fluid molecules. According to the Stokes-Einstein equation [E1.01], a NP's diffusion coefficient (D_p), or the rate at which it experiences Brownian motion, is inversely related to NP diameter (d) and dispersant viscosity (μ) and directly related to the product of dispersant temperature (T) and the Boltzmann constant (k_b) (Yao et al., 1971; Christian et al., 2008; Logan, 2012).

$$D_p = \frac{Tk_b}{3\pi d\mu} \quad \text{[E1.01]}$$

Following [E1.01], smaller NPs or those dispersed in warmer or less viscous groundwater will diffuse at greater rates (Christian et al., 2008; Logan, 2012). Therefore, NPs are more diffusive than larger particles and, thus, are more likely to be deflected into surrounding matrix grains (Yao et al., 1971; Njuguna et al., 2014). Furthermore, NPs will migrate into and out of immobile pore spaces and other low-concentration areas faster than larger particles (Njuguna et al., 2014).

Ultimately, NP fate and transport is influenced by NP size, composition, stability, and reactivity; groundwater velocity, temperature, pH, ionic strength, and types and concentrations of DOM, ions, and other NPs; and matrix composition, porosity, and permeability (Christian et al., 2008; Ghosh et al., 2008; Baumann, 2010; Karathanasis, 2010; Petosa et al., 2010; Wagner et al., 2014). Such variables, the complexity of natural systems, and the recent emergence of nanotechnology lend to the limited understanding of NP fate and transport processes in saturated porous media (Hofmann and von der Kammer, 2009; Keller et al., 2010; Petosa et al., 2010). Expeditiously elucidating such processes is key to prudent ENP management and regulation (Aiken et al., 2011).

Carbon Nanoparticles

Identifying a NP with qualities characteristic of an ideal groundwater tracer could enable a novel approach to estimating hydrogeologic conditions and transport behaviors of poorly understood NPs. Ideal tracers are readily dissolved or dispersed in water; inexpensive, inert, and nontoxic; and easily sampled, analyzed, and detected over a wide range of concentrations. Additionally, they leave no lasting impacts on hydrogeologic systems and are either absent from or exist at low concentrations in application areas (Davis and de Wiest, 1967; Sanford et al., 1996). Solutes, such as chloride and bromide (Br), are frequently used as groundwater tracers and commonly exhibit several characteristics of ideal tracers (Sanford et al., 1996). Compared to most solutes, NPs are less diffusive in saturated porous media and, thus, are less susceptible to diffusion-related retardation (McKay et al., 2000). Furthermore, inert NPs are not subject to deposition via infiltration and sedimentation (Yao et al., 1971). Nonetheless, the inherent reactivity of many NPs, especially certain ENPs, typically discourages their use as groundwater tracers.

Recent studies have concluded that engineered fluorescent CNPs exhibit multiple characteristics of ideal groundwater tracers (Kanj et al., 2011; Subramanian et al., 2013; Li et al., 2014; King, 2015). These CNPs are conveniently and inexpensively synthesized in laboratory settings in a one-step thermal decomposition of ethanolamine and citric acid monohydrate. This process produces slightly hairy, nearly spherical carbon cores coated with amide fluorophores (Bourlinos et al., 2008; Krysmann et al., 2012; Li et al., 2014). With diameters less than 10 nm, these CNPs are smaller than the vast majority of natural pore spaces (Bourlinos et al., 2008; Subramanian et al., 2013). Carbon NPs are also nontoxic, environmentally benign, and surface functionalized to be highly hydrophilic (Krysmann et al., 2012; Subramanian et al., 2013; King, 2015). While their carbon cores naturally fluoresce, most CNP fluorescence can be credited to their amide-fluorophore coating (Krysmann et al., 2012). High CNP emission intensity under a defined range of excitation wavelengths enables detection at concentrations less than 1 part per million (ppm) using a spectrofluorometer (Kanj et al., 2011; Subramanian et al., 2013).

Despite the notion that NPs with near-neutral surface charges will agglomerate, CNPs maintain stable dispersions under various hydrochemical conditions. This is likely caused by the coating of hydrophilic hairs that create repulsive steric forces (Li et al., 2014). By measuring electrostatic mobility and applying dynamic light scattering theory, Subramanian and others (2013) estimated CNP zeta potential and diameter were -5 mV and 2 nm to 5 nm, respectively, in water at pH 7. Transmission electron microscope (TEM) imaging confirmed this CNP size range and indicated no significant aggregation (Figure 1.09) (Subramanian et al., 2013). Li and others (2014) reported near-zero CNP zeta potentials in deionized (DI) water at pH 7.35 and a brine solution at pH 6.34 composed of monovalent and divalent ions. Carbon NP diameter was only reduced by an average of 0.2 nm in brine (Li et al., 2014). Kanj and others (2011) concluded that CNPs remained stable

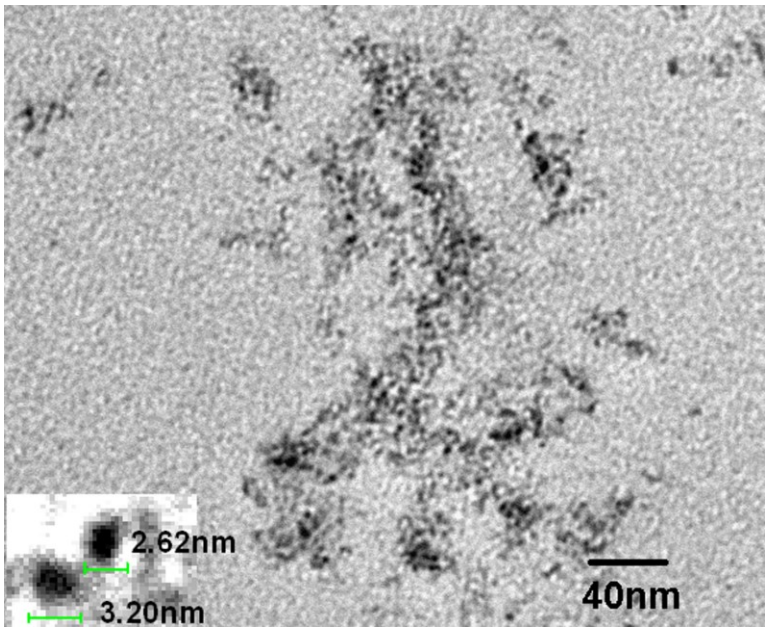

Figure 1.09: TEM image of CNPs indicating their size (from Subramanian et al., 2013).

in DI water and brine (230,000 ppm) from room temperature to 150 degrees Celsius (°C) and in the presence of oil. Such stability is attributed to their designed amide-fluorophore coating (Kanj et al., 2011). Furthermore, based on their estimated size and the Stokes-Einstein equation [E1.01], Subramanian and others (2013) concluded CNPs are less diffusive than the common conservative chemical tracer, Br, by an order of magnitude. Nonetheless, the effectiveness of CNPs as groundwater tracers greatly depends on their ability to exhibit unimpaired mass-conservative transport in a variety of hydrogeologic settings.

Carbon NP transport has mostly been studied in 1D column experiments. Subramanian and others (2013) compared transport behaviors of CNPs, Br, silica nanospheres, and Rhodamine-6G dye in 1D homogeneous columns packed with fine and coarse glass beads. While a substantial portion of injected silica nanospheres and Rhodamine-6G dye adhered to the porous media, CNP and Br transport was nearly identical and unimpeded. Minimal CNP retention was observed in subsequent column experiments designed to induce CNP and Br diffusion into fine-grained matrices

(Subramanian et al., 2013). Using 1D homogeneous columns packed with calcium carbonate sand, Li and others (2014) compared transport behaviors of Br and eight types of ENPs. Minimal sorption and retention of CNPs, enlarged CNPs, silica NPs, and polyacrylonitrile NPs was observed in dispersions of DI water, and their transport behaviors were very similar to that of Br. However, when dispersed in brine, CNPs were the only tracer that transported with minimal adsorption to the saturated porous medium. In fact, CNPs were the only tracer associated with over 95% mass recovery in low- and high-salinity dispersants. In addition to their engineered near-neutral surface charge and small size, such conservative transport likely results from CNPs' stability in the presence of negatively and positively charged porous media and high dispersant ionic strength (Li et al., 2014).

Most recently, as described in their unpublished thesis, King (2015) conducted several 1D column experiments focused on CNP transport alongside Br. In homogeneous columns packed with coarse-grained silica sand, CNP transport and Br transport were nearly identical, unimpeded, and conservative with over 95% of the injected tracer masses consistently recovered. Subsequent 1D column experiments designed to promote preferential flow along a core of coarse-grained silica sand and diffusion into a surrounding fine-grained silica sand matrix also indicated similar tracer transport. These dual-porosity trials concluded Br was more diffusive than CNPs. However, pore water velocities were too great and permeability differences between cores and surrounding fine-grained matrices were insufficient to enable the intended degree of tracer diffusion. King (2015) also compared 1D CNP and Br transport in reactive porous media consisting of coarse-grained silica sand and surface-modified zeolite designed to have a strong positive surface charge. Unlike Br, which was substantially retarded and retained by the reactive columns, CNP transport was mostly unaffected (King, 2015).

Kanj and others (2011) conducted the only field-scale tracer test with CNPs. Prior to this field trial, coreflood tests were conducted at room temperature and 150 °C using saturated low- and high-permeability samples of the oil-bearing Jurassic Arab-D limestone and dolomite formation. To further simulate CNP transport under oil reservoir conditions, coreflood tests incorporated high-salinity brine solutions (120,000 ppm) and pore and overburden pressures of 40,000 and 70,000 kilopascals, respectively. These laboratory tests revealed CNP transport was mostly unimpaired under the most complex simulated conditions; over 96% of the injected mass was recovered. Afterward, a single-well push-pull field tracer test was initiated by injecting approximately 40,500 liters of 130-ppm-CNP solution into a mostly swept portion of the Arab-D formation. The well was shut-in for roughly three days before being allowed to flow at a rate between 340 and 370 liters per minute. Despite the length of time CNPs were exposed to harsh reservoir conditions and the proximity of the injection/production well to multiple water injectors (1 to 3 kilometers), an estimated 86% of the injected CNP mass was recovered during this test (Kanj et al., 2011).

This series of laboratory and field tests indicates CNP transport is highly conservative under various simulated and natural hydrogeologic conditions. Furthermore, these tests suggest CNPs are transported more efficiently than several ENPs, Rhodamine-6G dye, and Br in column tracer tests. With their current design, CNPs are groundwater tracer candidates that show remarkable potential for identifying and quantifying preferential flow in saturated fractured bedrock and unconsolidated sediment. Due to their size and apparent stability and inertness, CNPs will likely be more effective groundwater tracers than other NPs. Carbon NPs might also enable more-accurate transport parameter estimates than solute tracers which commonly have higher diffusion coefficients (McKay et al., 2000). Therefore, CNPs could benefit multiple areas of academic and industrial geosciences including aquifer characterization, radioactive- and ENP-waste

management, groundwater remediation, contaminant transport investigations, enhanced oil recovery, and reservoir sensing (Kanj et al., 2011; Subramanian et al., 2013; Li et al., 2014; King, 2015). Additional CNP applications could arise with the ability to modify their size, shape, and other physical properties (Bourlinos et al., 2008; Krysmann et al., 2012).

Research Goals and Objectives

Past investigations demonstrate that CNP transport in saturated homogeneous and heterogeneous sediment compositions is mostly conservative and minimally retarded. Furthermore, CNPs remain stable under a range of hydrochemical conditions. Nonetheless, adequately understanding NP fate and transport in natural systems requires research focused on NP interactions with DOM (Aiken et al., 2011). Considering previous CNP investigations have ignored this ubiquitous environmental component, this study principally evaluates CNP transport in the presence of DOM.

This study has three primary objectives: (1) execute four 1D column experiments using dual-tracer solutions of CNPs and Br with specific pHs and DOM concentrations; (2) generate, analyze, and interpret CNP and Br breakthrough curves (BTCs); and (3) estimate CNP and Br transport parameters using temporal moment methods (TMMs) and inverse modeling techniques (Table 1.01). Inverse modeling will be conducted with CXTFIT 2.1, a solute transport modeling program that solves the advection-dispersion equation (ADE) for varying experimental conditions (Toride et al., 1995). Two experiments, Experiment 2 (E2) and Experiment 4 (E4), investigate CNP transport in homogeneous coarse-grained silica sand saturated with DI water at pH 4 and pH 7, respectively. Two additional experiments (i.e. Experiments 1 (E1) and 3 (E3)) are designed to investigate CNP transport in the presence of DOM (i.e. humic acid in background and dual-tracer solutions and coating matrix grains). Similar to E2 and E4, E1 and E3 are intended to study CNP

Table 1.01: Summary of study objectives, goals, and hypotheses

Objectives	• Execute four 1D column experiments using dual-tracer solutions of CNPs and Br with specific pHs and DOM concentrations • Generate, analyze, and interpret CNP and Br BTCs • Estimate CNP and Br transport parameters using TMMs and inverse modeling
Goals	• Determine the influence of DOM on CNP transport • Improve the understanding of how CNP transport and Br transport compare • Determine the feasibility of estimating CNP transport parameters with CXTFIT 2.1
Hypotheses	• E1: CNP transport will be unimpaired and conservative. • E2: CNP transport will be slightly impeded. • E3: CNP transport will be unimpaired and conservative. • E4: CNP transport will be unimpaired and conservative.

transport in water at pH 4 and pH 7, respectively. Following previous research (Subramanian et al., 2013; Li et al., 2014; King, 2015), this study is designed to analyze CNP transport alongside Br (as potassium bromide) using BTCs, or graphical representations of effluent tracer concentrations changing over time, and transport parameter estimation methods.

This study aims to accomplish three goals (Table 1.01). Ultimately, this study intends to determine the influence of DOM on CNP transport in saturated homogeneous porous media. Simultaneously, this study is designed to improve the understanding of how CNP transport compares to that of Br, a common conservative solute tracer. To satisfy these goals, CNP and Br BTCs are generated, analyzed, and interpreted to qualitatively and quantitively describe tracer transport under each set of environmental conditions. Furthermore, modeled and TMM-derived CNP and Br transport parameter estimates will be compared for each column experiment. Considering such comparisons necessitate accurate transport modeling, this study will determine the feasibility of estimating CNP transport parameters with CXTFIT 2.1. This goal will be addressed by analyzing observed BTC data from each column experiment with TMMs and CXTFIT 2.1. Since TMMs involve direct integration of observed BTC data and do not rely on a physical transport model, the validity of

modeled CNP transport parameter estimates will be determined by comparing them to those produced by TMMs (Wolff et al., 1979; Goltz and Roberts, 1987; Maloszewski et al., 1994; Das and Kluitenberg, 1996; Pang et al., 1998; Yu et al., 1999; Divine et al., 2003; Pang et al., 2003).

Previous studies have shown that CNPs transport conservatively in silica sand and glass beads without DOM (Subramanian et al., 2013; King, 2015). Carbon NPs have a slightly negative zeta potential in water near pH 7 regardless of ionic strength (Subramanian et al., 2013; Li et al., 2014). Silica sand has a strong negative zeta potential (i.e. approximately -40 mV) in water at pH 7 with an ionic strength of 10^{-3} moles per liter and becomes more negative as ionic strength and humic acid concentration increase (Jada et al., 2006; Chen et al., 2012). Furthermore, humic acid tends to make NP surface charges more negative (Christian et al., 2008; Wagner et al., 2014). Therefore, this study hypothesizes that, independent of DOM, CNP transport will be unimpaired and conservative in dispersants at pH 7 (i.e. E3 and E4) (Table 1.01).

While the influence of pH on CNP surface charge has not been directly measured, CNPs will approach their PZC as dispersant pH is decreased below 7. Considering their near-neutral zeta potential at approximately pH 7, CNPs will likely have a slightly positive zeta potential at pH 4. Since the surface charge of silica sand remains strongly negative at pH 4, CNPs might adsorb to sand without DOM. This change in CNP surface charge could also destabilize the dispersion. Therefore, this study hypothesizes that CNP transport will be slightly impeded in E2 (Table 1.01). However, since humic acid has been shown to increase NP stability and impart a negative surface charge on NPs below their PZC, this study hypothesizes that, in E1, DOM will enable conservative, unimpaired CNP transport in acidic dispersants (Table 1.01) (Christian et al., 2008; Wagner et al., 2014).

CHAPTER 2: METHODS

Introduction to Carbon Nanoparticles and Dissolved Organic Matter

Previous research has demonstrated that carbon nanoparticle (CNP) transport is minimally retarded and mostly conservative in a variety of saturated conditions: one-dimensional (1D) homogeneous and dual-porosity columns of glass beads, silica sand, and positively charged surface-modified zeolite (Subramanian et al., 2013; King, 2015); homogeneous calcium carbonate sand (Li et al., 2014); and high temperatures, pressures, and salinities in 1D column trials (Li et al., 2014) and a field-scale test targeting the oil-bearing Arab-D formation (Kanj et al., 2011). Studies have also shown that CNP transport can be similar to or more efficient than several other engineered nanoparticles (ENPs); the known conservative solute tracer, bromide (Br); and a common fluorescent dye tracer, Rhodamine-6G (Subramanian et al., 2013; Li et al., 2014; King, 2015). This consistently conservative transport indicates CNPs are inert in diverse hydrogeologic settings. Considering they are also inexpensive, conveniently synthesized, nontoxic, environmentally benign, hydrophilic, and easily detected at low concentrations, CNPs are ideal groundwater tracer candidates (Kanj et al., 2011; Krysmann et al., 2012; Subramanian et al., 2013; Li et al., 2014; King, 2015).

Despite the breadth of prior CNP transport research, the influence of dissolved organic matter (DOM) has yet to be investigated. Due to its ubiquity in nature and frequent control on nanoparticle (NP) stability and mobility, a sufficient understanding of CNP fate and transport requires research designed to evaluate the influence of DOM (Chen and Elimelech, 2008; Petosa et al., 2010; Aiken et al., 2011; Wagner et al., 2014). Generally, DOM stabilizes dispersions and enhances mobility by imparting negative charges on NP and matrix surfaces (Baalousha and Lead, 2007; Chen et al.,

2007; Hyung et al., 2007; Baalousha et al., 2008; Baumann, 2010; Aiken et al., 2011; Chen et al., 2012; Logan, 2012). Nonetheless, certain environmental conditions (e.g. DOM composition, dispersant pH, dispersant ionic strength, etc.) can instigate NP retardation via sorption, agglomeration, or other mechanisms (Chen et al, 2007; Chen and Elimelech, 2008; Christian et al., 2008; Wagner et al., 2014).

Methods Overview

This study is designed to address a critical research gap by primarily investigating the influence of DOM on CNP transport in homogeneous porous media saturated with neutral and acidic solutions. To further assess whether CNPs qualify as ideal groundwater tracers, this study aims to compare CNP transport to that of the known conservative solute tracer, Br. To accomplish these goals, four 1D column experiments (i.e. Experiments 1 (E1), 2 (E2), 3 (E3), and 4 (E4)) were conducted with dual-tracer solutions of CNPs and Br with controlled pHs and DOM concentrations. Table 2.01 summarizes the chemical and physical conditions selected for each column experiment. Such column experiments enabled observation of CNP and Br transport in saturated porous media under controlled conditions, collection of effluent tracer concentration data, and generation of breakthrough curves (BTCs).

Prior to conducting column tests, the experiment apparatus was configured and the CNP detection limit was determined. Determining this detection limit was primarily a troubleshooting measure intended to explain erratic CNP concentration data from prior column experiments. Subsequently, each column experiment was conducted in four stages: column and solution preparation (Stage 1), solution injection and sampling (Stage 2), effluent analysis (Stage 3), and data processing and

inverse modeling (Stage 4). Collectively, these experiments enabled comparison of CNP and Br transport behaviors and interpretations of how CNP transport is influenced by DOM.

Table 2.01: Summary of column experiment conditions

Experiment	Porous media	Influent background and dual-tracer solutions		Influent dual-tracer solution		
		pH	DOM concentration (ppm)	Ionic strength (mM)	Br concentration (ppm)	CNP concentration (ppm)
E1	saturated, homogenous, coarse-grained, acid-washed silica sand	4.0	4	3.13	250	2
E2		4.0	0			
E3		7.0	4			
E4		7.0	0			
mM=millimolar; ppm=parts per million						

Observed BTCs were analyzed with temporal moment methods (TMMs) and inverse modeling using the CXTFIT 2.1 code. Temporal moment methods and inverse modeling with CXTFIT 2.1 estimated CNP and Br transport parameters to explain and compare tracer transport and evaluate the influence of DOM. Briefly, CXTFIT 2.1 is a program used to model solute transport with the advection-dispersion equation (ADE) and estimate average pore water velocity (v_w), transport retardation factor (R), dispersion coefficient (D), and partitioning (β) and mass transfer (ω) coefficients describing chemical nonequilibrium sorption processes (Toride et al., 1995). To ensure tracer transport comparisons are meaningful, this study must determine whether CNP transport can be accurately modeled using the solute-specific ADE. Since TMMs rely on direct integration of observed BTC data rather than physical transport models, such methods are employed to gauge the representativeness of ADE-derived CNP transport parameter estimates

(Wolff et al., 1979; Goltz and Roberts, 1987; Maloszewski et al., 1994; Das and Kluitenberg, 1996; Pang et al., 1998; Yu et al., 1999; Divine et al., 2003; Pang et al., 2003).

Column Experiment Design

Each experiment utilized a benchtop design comprised of a cylindrical column, peristaltic pump, fraction collector, and three influent reservoirs connected by 1-millimeter (mm) inside-diameter (ID) Tygon® tubing (Figures 2.01 and 2.02). This tubing and Masterflex® C/L® peristaltic pump were used to convey deionized (DI) water, background solutions, and dual-tracer solutions from their respective reservoirs to an unused Kimble® FLEX-COLUMN® (ID=2.6 centimeters (cm), length (L)=12.3 cm) constructed of polypropylene and

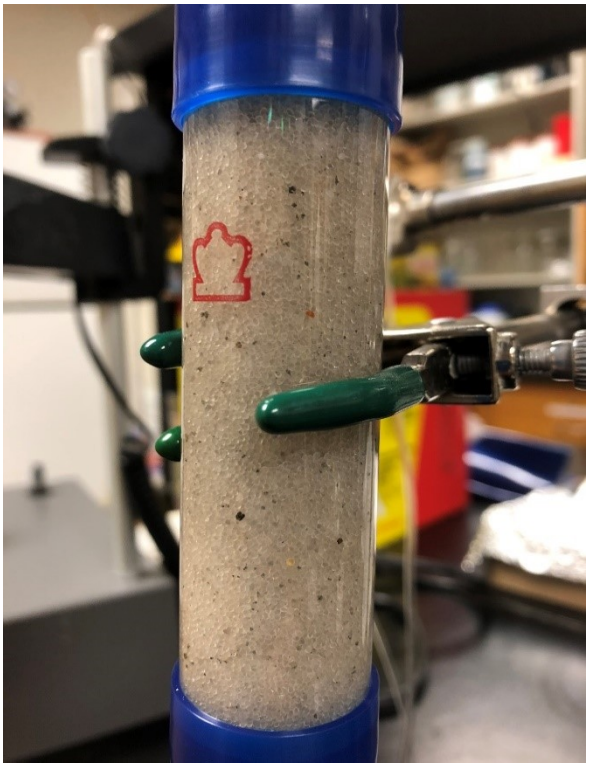

Figure 2.01: Column packed with saturated homogeneous coarse-grained silica sand.

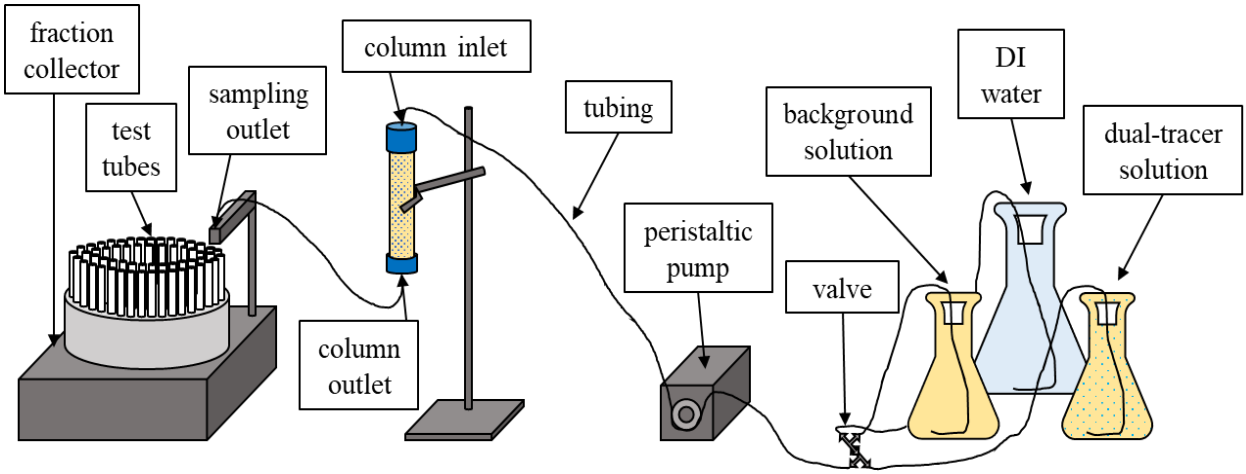

Figure 2.02: Column experiment apparatus.

borosilicate-glass (Figure 2.01). After flowing through this column, effluent solutions were directed to an Amersham Biosciences Frac-100™ fraction collector (Figures 2.02). Columns were suspended vertically by clamps and support stands and wet-packed with acid-washed ASTM 20-30 silica sand.

To avoid potentially compromising background and dual-tracer solutions, all tubing and fittings were made of chemical-resistant polymers and replaced after each experiment. Influent solutions were stored in 500-milliliter (mL) to 2,000-mL glass Erlenmeyer flasks. Round-bottom test tubes used for sample collection (outside diameter=16 mm, L=150 mm) were made of borosilicate glass. Between experiments, this glassware was washed and rinsed thoroughly with DI water.

Determining CNP Detection Limit

Prior to this study, the author attempted to reproduce King's (2015) column experiments that focused on the influence of positively charged sediment on CNP transport. Following King (2015), a dual-tracer solution consisting of Br (336 parts per million (ppm)) and CNPs (250 ppm) in DI water was pumped through 1D columns packed with a saturated mixture of surface-modified zeolite and coarse-grained silica sand. Effluent CNP concentrations (C) observed by King (2015) and the author fluctuate rapidly and dramatically above $C \approx 200$ ppm (Figure 2.03). Such results indicate either imprecise effluent CNP analyses or erratic transport behavior. Erratic data were also produced in homogeneous and dual-porosity column experiments that used silica sand and allowed CNP effluent concentrations to reach $C \approx 250$ ppm (King, 2015). Additionally, the author discovered that multiple series of CNP standard dispersions with concentrations between 2.5 ppm and 250 ppm produced unreliable nonlinear calibration curves. Therefore, the observed

questionable data likely result from the inability to define the relationship between CNP concentration and fluorescence intensity with strong linear regression equations.

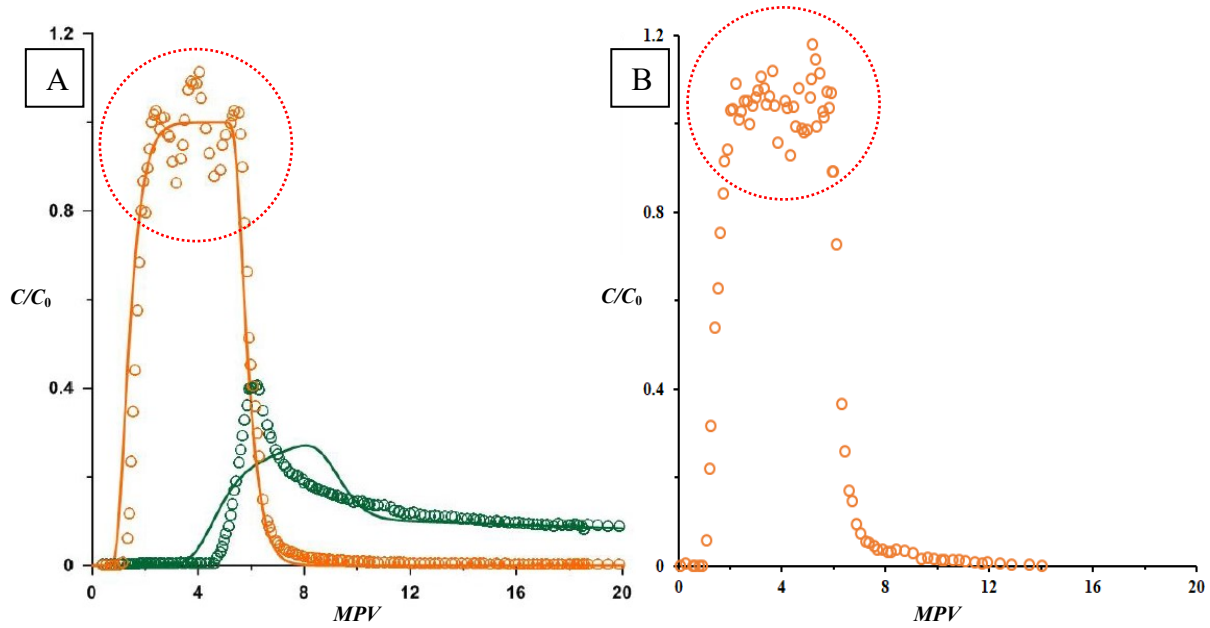

Figure 2.03: Breakthrough curves from (A) King's (2015) and (B) the author's surface-modified zeolite experiments. Red circles highlight erratic CNP concentration estimates above $C \approx 200$ ppm (modified from King, 2015). The x-axis represents mobile pore volumes of injected solutions as a dimensionless analog of time (*MPV*). The y-axis (C/C_0) represents the ratio of effluent concentration (C) to influent concentration (C_0). Both experiments used influent CNP concentrations of C_0=250 ppm.

To produce more effective calibration curves for future column experiments, a series of CNP standard dispersions ("CNP standards") were prepared for fluorescence analysis. These CNP standards represent a dilution series of CNP dispersions in DI water with concentrations spanning seven orders of magnitude from 0.001 ppm to 5,000 ppm. Each CNP standard was analyzed with a Tecan® infinite® 200 microplate reader capable of measuring fluorescence intensity (see "Stage 3: Effluent Analysis" below for additional information). While CNPs were previously detected at concentrations as low as approximately 0.01 ppm (Subramanian et al., 2013), the lowest-concentration (0.001 ppm) CNP standard was detected during this analysis (Figure 2.04). While, to the author's knowledge, this is the lowest CNP concentration ever detected, the accuracy of concentration estimates greatly improves once concentrations reach 0.01 ppm (Table 2.02).

Fluorescence intensity appears to peak at a CNP concentration of approximately 225 ppm (Figure 2.04). This concentration represents an inflection point above which CNP concentration and fluorescence intensity are negatively correlated. Kanj and others (2011) attributed such fluorescence intensity degradation to self-quenching caused by interactions among crowded CNPs.

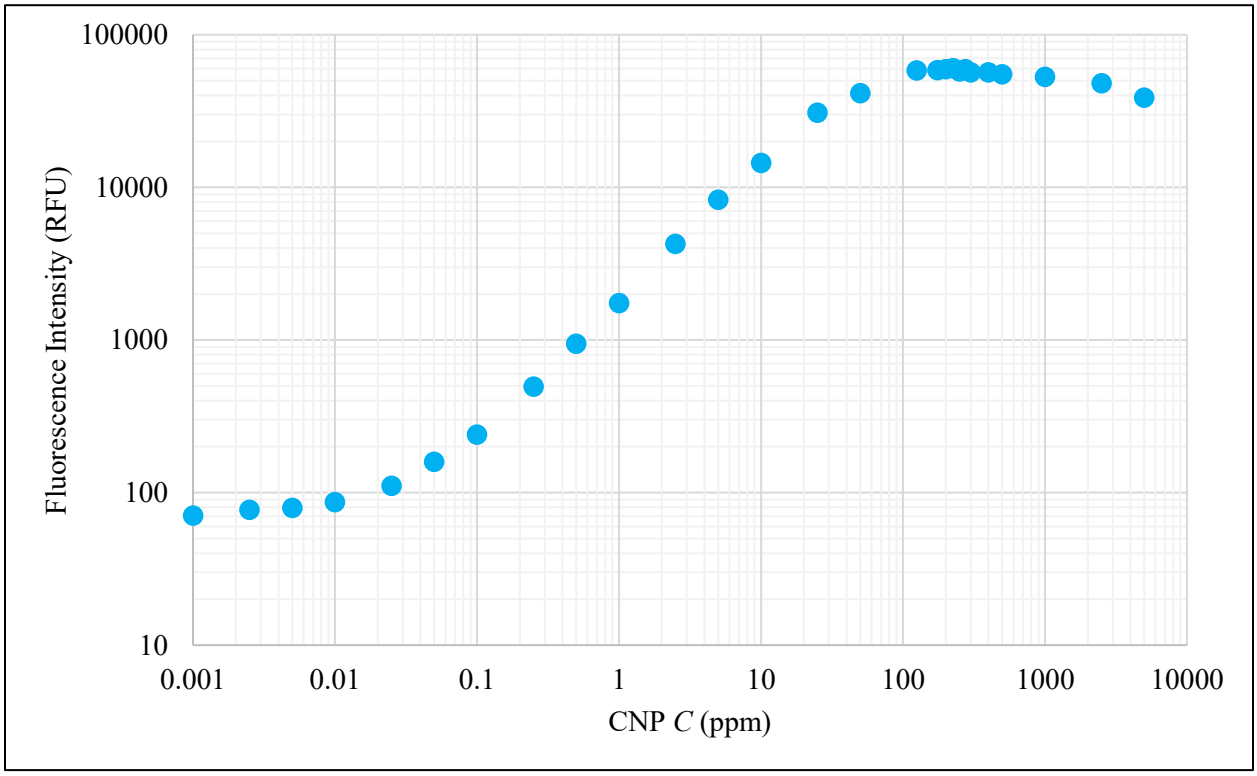

Figure 2.04: The relationship between CNP standard concentration (*C*) and fluorescence intensity. Fluorescence intensity is reported in relative fluorescence units (RFU). Note the logarithmic scales.

Table 2.02: Accuracy of CNP standard concentration estimates

CNP *C* (ppm)	**Mean estimated CNP *C* (ppm)**	**Estimated CNP *C SD* (ppm)**	**Error (%)**	***RSD* (%)**
0.0010	0.00076	0.00021	24	28
0.0050	0.0056	0.00010	12	1.8
0.010	0.010	0.00055	0.20	5.5
0.050	0.050	0.0012	0.93	2.4
0.10	0.10	0.0025	1.7	2.5
0.50	0.51	0.012	2.6	2.4
1.0	0.99	0.015	0.87	1.5
5.0	4.9	0.038	2.6	0.78
C=concentration; *SD*=standard deviation; *RSD*=relative standard deviation				

According to Li and others (2014), CNP concentration and fluorescence intensity are linearly correlated when CNP concentration is less than 100 ppm. Similarly, Kanj and others (2011) determined that the linear relationship between CNP concentration and fluorescence intensity begins degrading at CNP concentrations between 50 ppm and 100 ppm (Figure 2.05). Conversely,

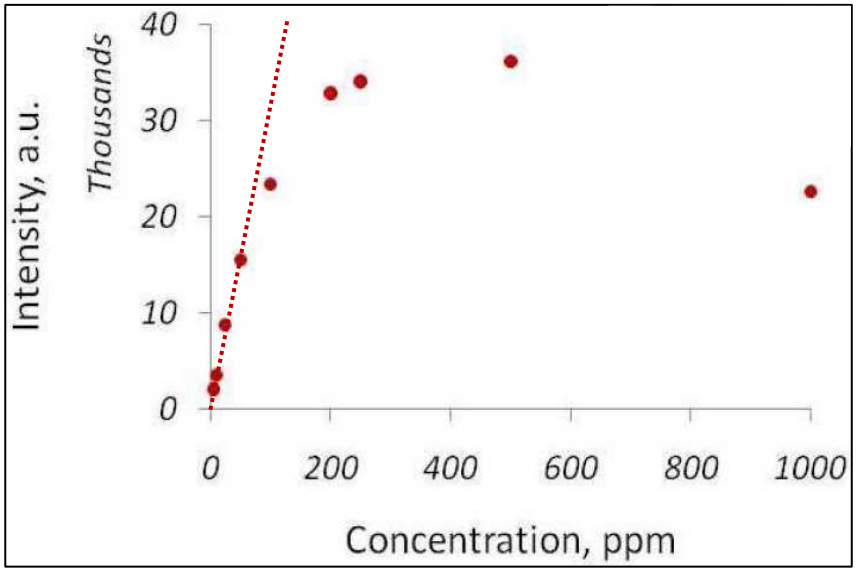

Figure 2.05: The relationship between CNP standard concentration and fluorescence intensity as determined by Kanj and others (2011). The line of best fit highlights the linear relationship breaking down as CNP concentration approaches 100 ppm (modified from Kanj et al., 2011).

this study finds that this linear correlation weakens as CNP concentrations approach 25 ppm (Figure 2.06). Thus, previous column experiments conducted by King (2015) and the author incorporated influent CNP concentrations (C_0=250 ppm) that exceeded a reasonable upper limit of detection. As indicated by a coefficient of determination (r^2) value near unity, the linear correlation between CNP concentration and fluorescence intensity is remarkably strong between 0.001 ppm and 5 ppm (Figure 2.07). This justifies the use of a relatively dilute CNP dispersion (C_0=2 ppm) for this study's column experiments. Furthermore, this preliminary investigation concludes CNP concentrations will be accurately estimated between 0.01 ppm and 2 ppm (±1.5%).

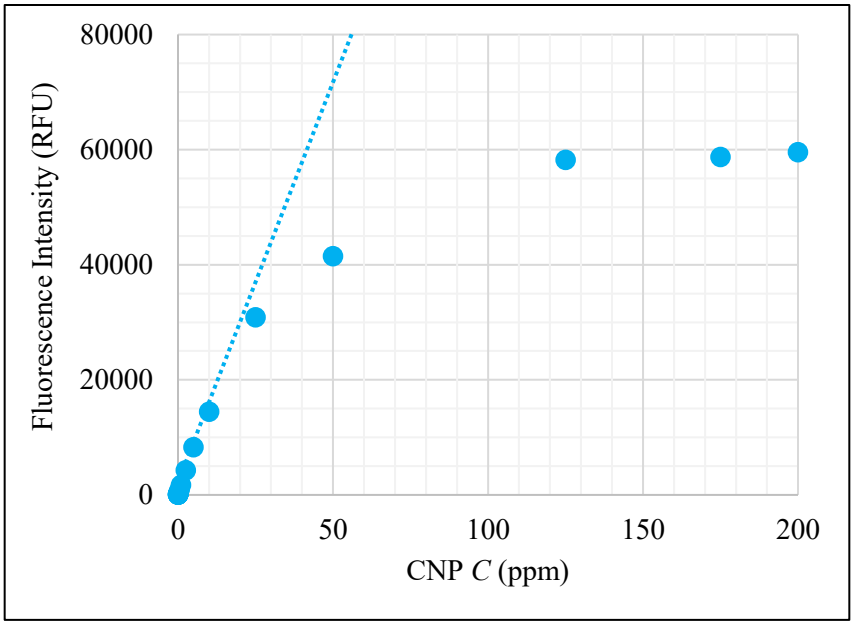

Figure 2.06: The relationship between CNP standard concentration (*C*) and fluorescence intensity for a subset of this study's data shown in Figure 2.04 (i.e. CNP standard concentrations from 0 ppm to 200 ppm). The line of best fit highlights the linear relationship breaking down as CNP concentration approaches 25 ppm.

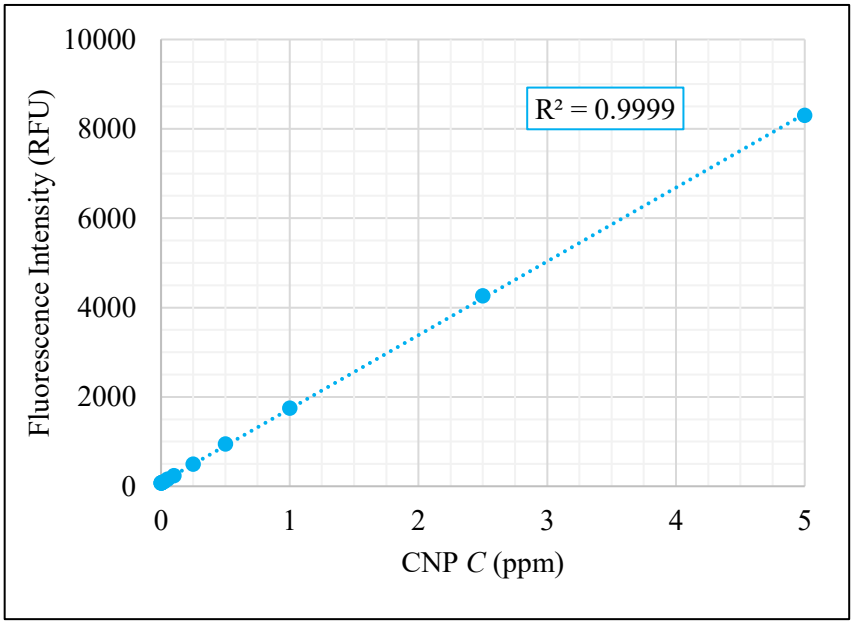

Figure 2.07: The relationship between CNP standard concentration (*C*) and fluorescence intensity for a subset of this study's data shown in Figure 2.04 (i.e. CNP standard concentrations from 0 ppm to 5 ppm). The dashed line represents the highly representative linear regression trendline.

Stage 1: Column and Solution Preparation

Porous Media

All column experiments were conducted with ASTM 20-30 silica sand (US Silica Company, Ottawa, Illinois plant) ("sand"). This well-rounded, well-sorted standard sand is graded to be mostly retained by a 600-micron (µm) (Number 30) sieve after passing through an 850-µm (Number 20) sieve (Figure 2.08) (ASTM Standard C778). Prior to being introduced to columns, the sand was acid-washed according to a method followed by Chen and others (2012). To remove minor amounts of metal oxides (e.g. aluminum oxide, iron oxide, titanium dioxide, etc.) and possible organic contaminants, this sand was soaked in 12 Normal sulfuric acid for approximately 24 hours. The sand was then rinsed repeatedly with DI water until the pH of the rinse waste was nearly neutral. The acid-washed sand was then baked for 8 hours at 800 degrees Celsius (°C) and soaked in DI water before column experiments began.

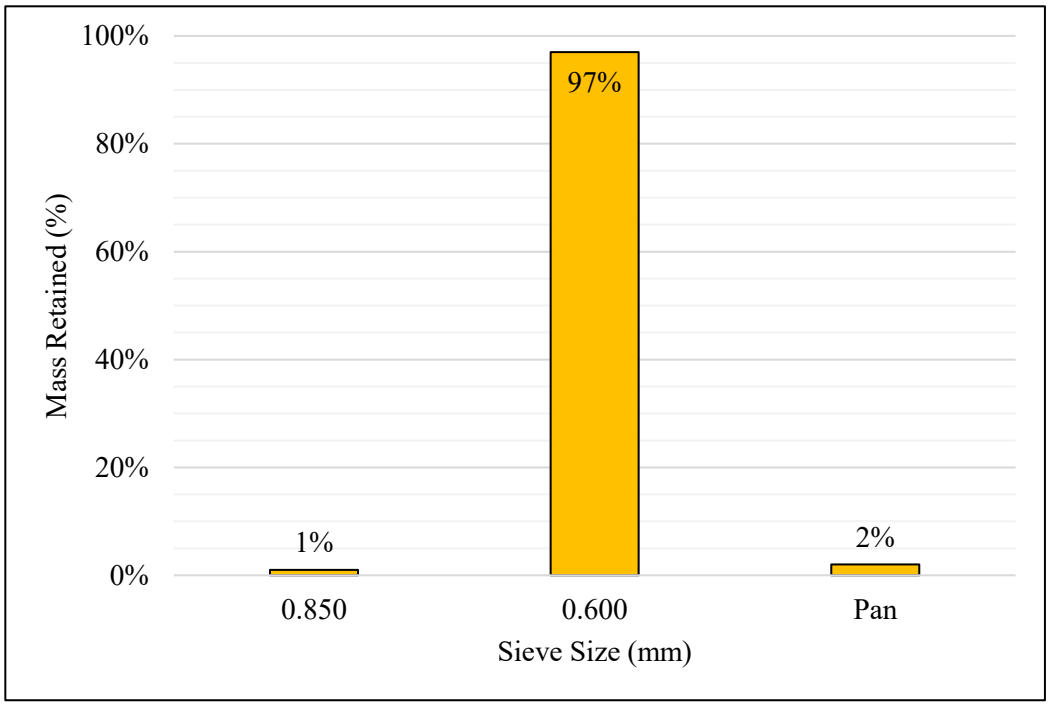

Figure 2.08: Grain size distribution of non-acid-washed ASTM 20-30 sand (US Silica Company, 1997).

Matrix Development

All columns were rinsed with DI water, air-dried, and suspended vertically before being wet-packed with acid-washed sand. To ensure matrix saturation and enable porosity estimations, a known volume of DI water (V_w=15 mL) was added to a column. The initial sediment mass (m_{ini}) was measured with a digital scale before sand was added to columns in 2-cm-thick increments. A tamping rod was used to consolidate sand and remove trapped air between each increment. Sand was added until the matrix was saturated with no excess water remaining. The mass of sand added to the column (m_s) was calculated once the excess portion (m_{exc}) of m_{ini} was measured [E2.01].

$$m_s = m_{ini} - m_{exc} \quad \text{[E2.01]}$$

The length of saturated sand (L_s) within the column and the column cross-sectional area (A) were used to calculate the total volume of saturated sand in the column (V_t) [E2.02].

$$V_t = A \times L_s \quad \text{[E2.02]}$$

The porosity of sand in the column was estimated volumetrically and gravimetrically (Table 2.03). Volumetric matrix porosity (ϕ_v) represents the ratio of pore volume at the point of saturation (V_p) to V_t [E2.03]. The wet-packing method described above permits the assumption that all pore spaces are filled with water and no excess water remains (V_w=V_p).

Table 2.03: Column porosity estimates

Experiment	ϕ_v	ϕ_g	ϕ
E1	0.38	0.35	0.36
E2	0.34	0.35	0.35
E3	0.34	0.35	0.35
E4	0.34	0.35	0.35

$$\phi_{\mathrm{v}} = \frac{V_{\mathrm{p}}}{V_{\mathrm{t}}} \quad \text{[E2.03]}$$

Gravimetric matrix porosity (ϕ_{g}) depends on the ratio of bulk matrix density (ρ_{b}) [E2.04] to the material density of silica (ρ_{s}=2.65 grams/cm^3). This ratio essentially represents the fraction of V_{t} occupied by sand. Therefore, the remaining fraction of V_{t} in a saturated system is occupied by water and represents matrix porosity [E2.05].

$$\rho_{\mathrm{b}} = \frac{m_{\mathrm{s}}}{V_{\mathrm{t}}} \quad \text{[E2.04]}$$

$$\phi_{\mathrm{g}} = 1 - \frac{\rho_{\mathrm{b}}}{\rho_{\mathrm{s}}} \quad \text{[E2.05]}$$

Volumetric and gravimetric porosities were averaged to determine a single matrix porosity estimate (ϕ) (Table 2.03). Next, following the same wet-packing procedure, additional DI water and sand were added to the column until the entire column was occupied by saturated porous media. The total volume (V_{T}) of the filled column (V_{T}=64.4 cm^3) and ϕ were used to determine the total pore volume of each column (V_{P}) [E2.06].

$$V_{\mathrm{P}} = V_{\mathrm{T}} \times \phi \quad \text{[E2.06]}$$

The volumes of influent solutions (i.e. DI water, background solutions, and dual-tracer solutions) injected into the columns were normalized to V_{P} to compensate for slight differences in ϕ and volumetric flow rates (Q). This normalization was essential for ensuring equal masses of CNPs and Br, relative to the column's V_{P}, were introduced to each column. Furthermore, CNP and Br BTCs for multiple column experiments can be compared when column experiment time (t) is represented by the number of injected influent pore volumes (PV) [E2.07].

$$PV = \frac{t \times Q}{V_P} \quad \text{[E2.07]}$$

Finally, saturated columns were capped and stored at room temperature for 24 hours to allow the sand to fully rehydrate (Chen et al., 2012).

Solution Preparation

Robust and reproducible column experiments require carefully and consistently prepared background, dual-tracer, and standard solutions. Prior to introducing dual-tracer solutions, background solutions were prepared to establish chemical equilibrium according to intended experimental conditions (i.e. pH and DOM concentration) (Table 2.01). Dual-tracer solutions consisting of CNPs (2 ppm) and Br (250 ppm) were prepared to match their respective background solution's pH and DOM concentration. Standard solutions were necessary for accurate measurement of effluent CNP and Br concentrations. For consistency, unique standards were prepared for each column experiment with pH and DOM concentrations matching their respective background and dual-tracer solutions.

Background, dual-tracer, and standard solutions required six fundamental ingredients: DI water, concentrated sulfuric acid and sodium hydroxide, a stock CNP dispersion, and stock potassium bromide and DOM solutions. All DI water was provided by the Center for Applied Isotope Research for Industry and Environment (Colorado State University, Fort Collins, Colorado), whose laboratory is equipped with a two-stage Milli-Q (MilliporeSigma) water purification and filtration system. Negligible volumes of concentrated sulfuric acid and sodium hydroxide were applied to background, dual-tracer, and standard solutions to ensure intended and consistent solution pH. Solution temperature and pH were measured with an Oakton immersion temperature

probe and double-junction pH electrode connected to an Oakton Ion6+ meter. This pH probe was calibrated with pH 4.01, 7.00, and 10.01 buffer solutions before each use; rinsed with DI water between measurements; and stored in Oakton pH electrode storage solution between uses.

The stock CNP solution (96,000 ppm) was prepared by Dr. Yan Li of Colorado State University's Department of Design and Merchandising as documented by Li and others (2014). Briefly, 378 grams (g) of citric acid monohydrate and 330 g of ethanolamine were placed in separate beakers containing 900 mL of DI water each. Once the citric acid monohydrate was completely dissolved, the dilute ethanolamine was added, and the mixture was magnetically stirred. The solution was continuously stirred, heated to approximately 70 °C, and allowed to evaporate until approximately 650 mL remained. The remaining solution was transferred to an oven, incrementally heated (10 °C per minute (min)) to 200 °C, and pyrolyzed for 8 hours. This method produces a dark, viscous CNP substance that is readily dispersible in DI water (Figure 2.09) (Li et al., 2014). The stock potassium bromide solution (1,000 ppm) was purchased (Fisher Scientific™).

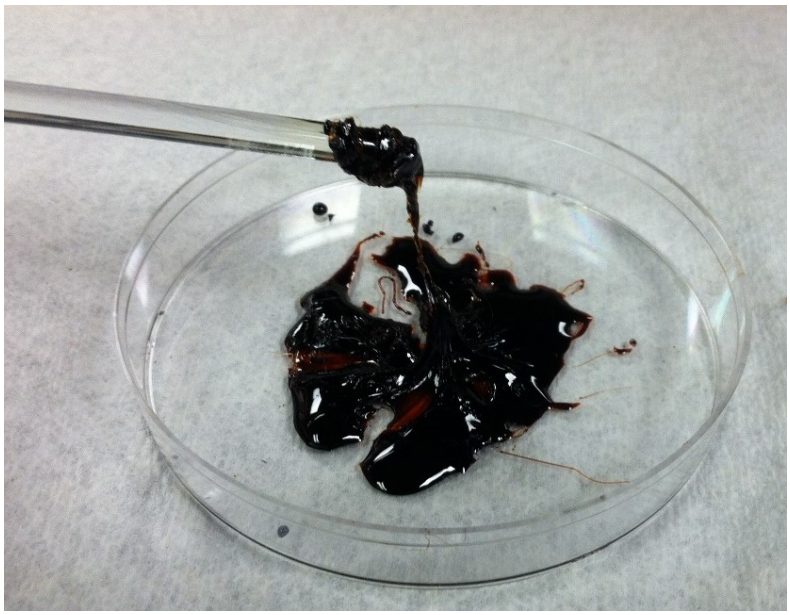

Figure 2.09: Concentrated CNP substance (from King, 2015).

The stock DOM solution was prepared from a solid Pahokee Peat humic acid (PPHA) standard (International Humic Substances Society) according to a method by Chen and others (2012). Briefly, 50 milligrams of PPHA were weighed with a digital scale and added to DI water in a glass 1,000-mL volumetric flask. To promote PPHA dissolution, a small amount of concentrated sodium hydroxide was added which increased the pH to 7.7. The solution was stirred overnight with a magnetic stir bar. Incomplete PPHA dissolution required vacuum filtration with 0.45-µm Durapore® membrane filters (MilliporeSigma) made of chemical-resistant hydrophilic polyvinylidene fluoride. Prior to filtration, membranes were labeled and individually weighed using a digital scale. The 1,000-mL solution was filtered in 250-mL increments. Following filtration, filters were baked at 75 °C for over 24 hours. Dried filters were weighed using the same digital scale, and the mass of PPHA retained by filters was calculated by subtracting the final filter mass from the initial filter mass. The mass of dissolved PPHA (operationally defined as the mass which passed through the 0.45-µm filter) was calculated as the difference between starting PPHA mass and the mass of PPHA retained by the filters. This method produced 1 liter of DOM stock solution (33 ppm).

Experiment-ready background, dual-tracer, and standard solutions were prepared by diluting stock solutions with DI water. Once solutions were stirred to ensure homogeneity, initial pH was measured and negligible volumes of concentrated sulfuric acid and (or) sodium hydroxide were added to achieve the desired final solution pH (Table 2.01). All E1 and E3 solutions were prepared to contain 4 ppm DOM, while DOM was withheld from E2 and E4 solutions. All solutions were stored in glass or high-density polyethylene (HDPE) containers at room temperature during their respective column experiments and at approximately 4 °C otherwise.

Column Equilibration

Once the matrix and solutions were prepared, the column was flushed in a downward direction with at least 10 pore volumes (PVs) of DI water (Chen et al., 2012). Prior to pumping, influent tubing was air-filled and remained disconnected from the column inlet. Once pumping began, DI water flowed from its reservoir to the three-way solution-control valve ("valve") (Figure 2.02). A stopwatch was used to measure elapsed time as DI water flowed from the valve to the column inlet (t_{inf}). Known t_{inf} and tubing lengths enabled estimation of elapsed time as effluent flowed from the column outlet to the fraction collector sampling outlet (t_{eff}) (Figure 2.02). Air within the tubing that connected the background and dual-tracer solution reservoirs to the valve was removed via siphoning. Once all air was removed from the system, the influent tubing was connected to the column inlet and the DI-water flush was initiated. This step prevented the injection of air into the saturated matrix and enabled timestamp corrections for future effluent samples.

During the DI-water flush, Q was estimated by collecting column effluent from the fraction collector sampling port with a 25-mL graduated cylinder and recording elapsed time with a stopwatch. To compensate for slight fluctuations in power supplied to the peristaltic pump, an average Q was calculated by collecting one or more known volume(s) of effluent DI water over a minimum period of 60 min. Low flow rates similar to Chen and others' (2012) (0.40 mL/min) were maintained for all column experiments (Table 2.04). Quantifying Q is essential for accurate data analysis (i.e. estimating tracer mass recovery and transport parameters); programming the fraction collector to collect an adequate sample volume; and determining appropriate solution injection durations.

Table 2.04: Column experiment flow rates

Experiment	Q (mL/min)
E1	0.39
E2	0.36
E3	0.38
E4	0.38

Once the column was adequately flushed and the background solution pH was confirmed, the valve was adjusted to simultaneously stop the flow of DI water and begin the background solution injection phase. This valve enabled continuous pumping at a constant Q. Following Chen and others (2012), at least 22 PVs of background solution were injected to equilibrate the column to a desired pH and DOM concentration before introducing tracers. As an additional precaution, the column was continuously flushed with the background solution until effluent pH matched influent pH.

Stage 2: Solution Injection and Sampling

Once chemical equilibrium was established, the pH of the dual-tracer solution was verified. Next, the fraction collector was loaded with 95 clean test tubes and programmed to collect 3.5-mL effluent samples according to a specified sampling time interval. This time interval was calculated by dividing the desired sample volume by the average Q. Each sample was assigned a discrete timestamp representing the median time of each sampling interval. For example, if the j^{th} sample was collected over a period of 5 min, from 10 min to 15 min after a column experiment began, this sample's timestamp (t_j) would be t_j=12.5 min.

Once the fraction collector was prepared, the valve was adjusted to simultaneously terminate the background solution flush and begin the dual-tracer solution injection. While the programmed fraction collector was activated immediately after the dual-tracer injection began, column

experiments did not officially begin until the dual-tracer solution reached the column inlet (t_i). To ensure sample times only accounted for intracolumn tracer transport, t_j was corrected (t_c) by subtracting the sum of t_{inf} and t_{eff} [E2.08].

$$t_c = t_j - (t_{inf} + t_{eff}) \quad \text{[E2.08]}$$

Similar to Chen and others (2012), approximately 5 PVs of dual-tracer solution were injected. This volume was designed to be sufficient for C to reach C_0. Subsequently, the valve was readjusted to terminate the dual-tracer solution injection and resume the background solution injection. Over 9 PVs of background solution were injected into each column to ensure maximum tracer removal and mass recovery. Continuous use of the fraction collector during the dual-tracer solution injection and subsequent background solution flush produced 95 samples per column experiment. In summary, CNPs and Br were introduced to and subsequently flushed from columns with pulses of influent dual-tracer solutions and tracer-free background solutions, respectively.

Stage 3: Effluent Analysis

Select samples were analyzed for Br and CNP concentrations using an Orion™ Br ion selective electrode (ISE) (Thermo Scientific™) and a Tecan® infinite® 200 microplate reader, respectively. Prior to analyses, all samples were stored in labeled 25-mL HDPE bottles, and Br and CNP standards were passively warmed to ambient temperatures. A three-point calibration of the Br ISE was performed prior to each use with 1-ppm, 10-ppm, and 100-ppm Br standards. To generate a CNP calibration curve and verify C_0 for each experiment, a clean Nunc™ MicroWell™ 96-well transparent-bottom polystyrol microplate (Thermo Scientific™) was loaded with several 0.35-mL

aliquots of influent dual-tracer solution and nine CNP standards with concentrations spanning four orders of magnitude (Figure 2.10).

Figure 2.10: Microplate (96 wells) loaded with CNP standards and effluent samples.

Samples were selected to sufficiently characterize periods of rapid effluent Br and CNP concentration changes. A 0.35-mL aliquot of each selected sample was added to the microplate for future CNP analysis. The remaining 3.15 mL of each sample were transferred to a glass 10-mL beaker and treated with ionic strength adjustor (2% of sample volume) (Thermo Scientific™). The beaker was moved to a magnetic plate to maintain solution homogeneity. The Br ISE and temperature probe were submerged in the sample and allowed to stabilize before measurements were recorded. For quality assurance, standard solution and sample temperatures were required to be within 1 °C of one another.

Once filled with standard solutions and samples, the microplate was capped, sealed with plastic wrap, and covered with aluminum foil to prevent evaporation and photodegradation. The microplate reader was prepared for accurately measuring CNP fluorescence by selecting the ideal emission (λ_{em}) and excitation (λ_{ex}) wavelengths. As determined by Krysmann and others (2012),

the most intense CNP fluorescence is emitted at λ_{em}=455 nanometers (nm) when aqueous CNP dispersions at pH 4 to 12 are excited at λ_{ex}=375 nm (Figure 2.11). While such specific λ_{em} and λ_{ex} settings are not available for this microplate reader, Figure 2.11 indicates the λ_{em} (460 nm) and λ_{ex} (355 nm) selected for this study will enable sufficient CNP fluorescence measurements.

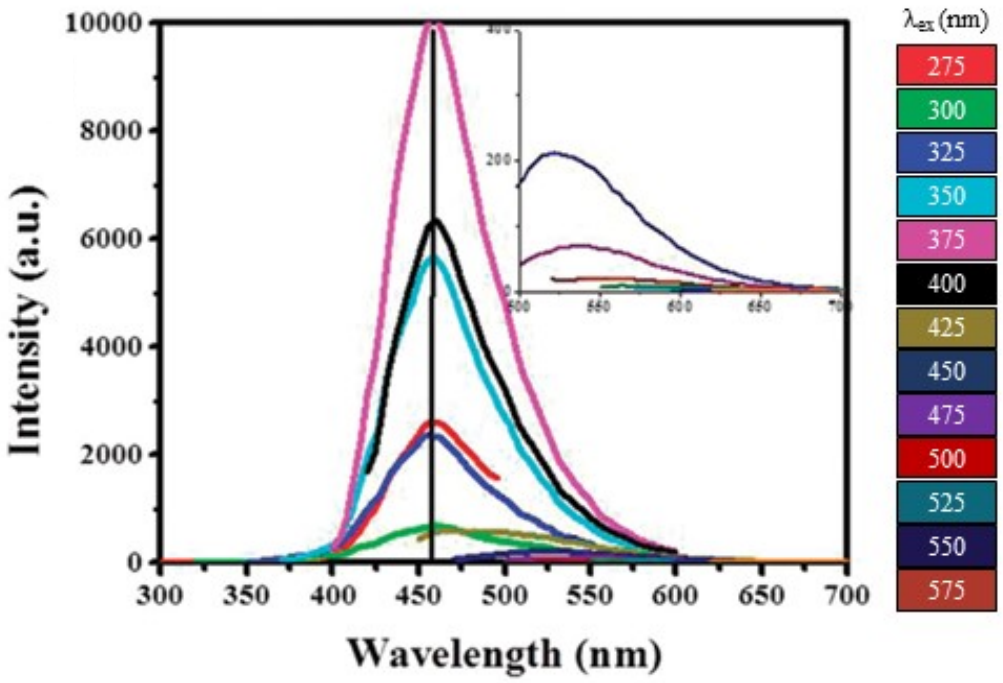

Figure 2.11: Fluorescence spectrum of an aqueous CNP dispersion (modified from Krysmann et al., 2012). The x-axis represents λ_{em}.

The microplate reader was programmed to calculate the gain setting from the sample well with the highest CNP concentration and to collect a certain number of fluorescence intensity measurements per sample well. Based on this programming, each sample well was divided into a circular grid of 24 cells from which ten CNP fluorescence intensity measurements were collected. Each sample well's reported CNP fluorescence intensity, in relative fluorescence units (RFU), represents the average of these 240 measurements. Analyzed microplates were repackaged in plastic wrap and aluminum foil and stored in a sealed bag at room temperature pending data processing and confirmation of successful CNP concentration estimations.

Stage 4: Data Processing and Inverse Modeling

Following sample analysis, Br and CNP concentration data were processed and analyzed using BTCs and inverse modeling to estimate transport parameters and compare tracer performance. A regression analysis was performed after each column experiment to mathematically define the linear relationship between CNP standard concentration and measured CNP standard fluorescence intensity. The resulting calibration curves were used to estimate effluent CNP concentrations from sample fluorescence intensity measurements. While the Br ISE directly measures electric potential, this device was calibrated to automatically estimate sample Br concentrations. Effluent tracer concentrations (C) were normalized to their respective influent concentration (C_0) and converted to a dimensionless relative concentration (C/C_0).

Prior to generating BTCs, each sample's representative t_c was converted to the dimensionless analog of time, PV [E2.07]. Normalizing sample concentration and time data accounts for slight differences in Q and C_0 and enables direct comparisons of CNP and Br transport among multiple column experiments. Breakthrough curves facilitated such comparisons and enabled transport behaviors of individual tracers to be evaluated. In this study, BTCs conveniently illustrate how relative CNP and Br concentrations change over the duration of a column experiment as a constant finite pulse of dual-tracer solution is injected and then flushed with background solution. Breakthrough curves graphically display key effluent characteristics (e.g. arrival times, peak effluent concentrations, elution tailing, etc.) that enable qualitative and quantitative descriptions of solute and particle transport mechanisms (e.g. retardation, (de)sorption, diffusion, etc.) (Figure 2.12). Furthermore, BTC data associated with conservative tracers can be used to estimate groundwater flow properties (e.g. average pore water velocity, dispersion, etc.).

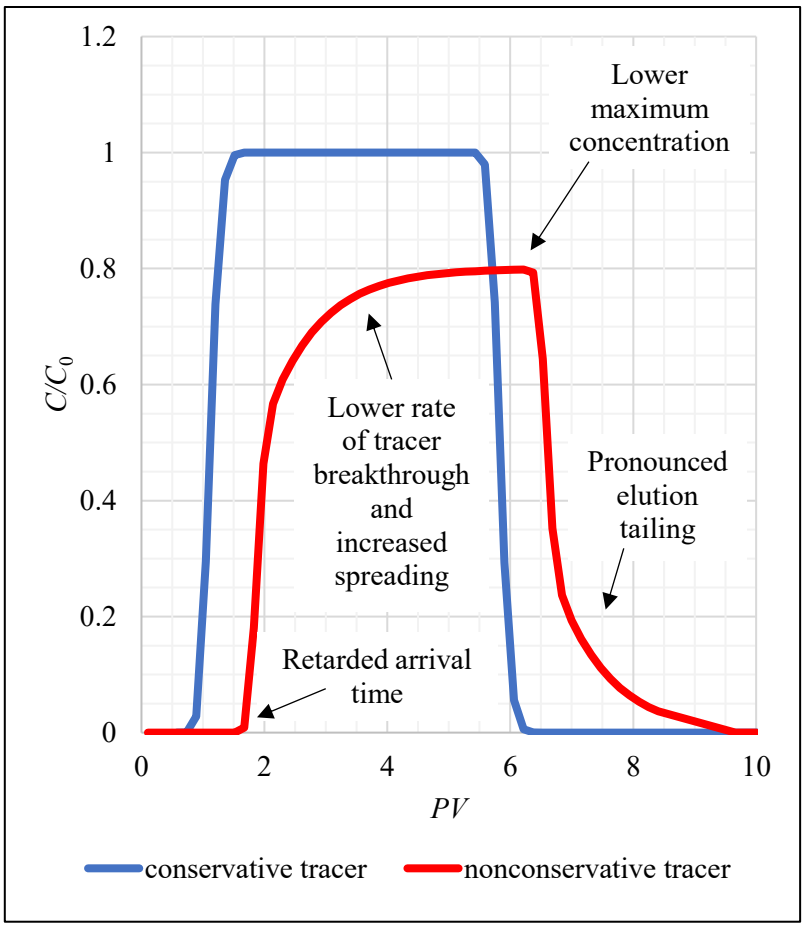

Figure 2.12: Conceptual BTCs depicting unimpeded transport of a conservative tracer (blue) and retarded transport of a nonconservative tracer (red) associated with sorption and diffusion.

Temporal Moment Methods

Transport properties were estimated by analyzing observed and modeled BTCs with TMMs. These methods are commonly used to analyze tracer transport because they do not rely on a physical model. Therefore, TMMs can directly estimate transport parameters without fitting an analytical solution of the ADE to BTC data (Wolff et al., 1979; Goltz and Roberts, 1987; Maloszewski et al., 1994; Das and Kluitenberg, 1996; Pang et al., 1998; Yu et al., 1999; Divine et al., 2003; Pang et al., 2003). Furthermore, unlike the ADE, TMMs do not require the assumptions of homogeneous and isotropic porous media and fluid content (Yu et al., 1999). A temporal moment of the i^{th} order

(m_i) depends on effluent concentration (C) as a function of sample time (t) and distance from the column inlet (x) [E2.09] (Wolff et al., 1979). In this study, C is dimensionless (C/C_0), x is a constant position at the column outlet (L=12.3 cm), and t_f represents the final sample time for each column experiment.

$$m_i = \int_0^{t_f} t^i C(x,t)dt \quad \text{[E2.09]}$$

A given tracer's zeroth temporal moment (m_0) is defined as the integral of its BTC with respect to time. Therefore, m_0 represents the amount of tracer mass recovered during a column experiment as estimated by the trapezoid rule [E2.10]. The percentages of injected tracer masses (m_{inj}) recovered during column experiments are calculated from m_0 (%MR) [E2.11].

$$m_0 = \int_0^{t_f} C(x,t)dt \cong \sum_{n=0}^{f} \left(\frac{C_n + C_{n-1}}{2}\right)(t_n - t_{n-1}) \quad \text{[E2.10]}$$

$$\%MR = \frac{m_0}{m_{inj}} \times 100 \quad \text{[E2.11]}$$

The trapezoid rule was also used to estimate the first (m_1) and second (m_2) temporal moments for CNP and Br transport. The normalized first temporal moment (M_1) was calculated [E2.12] to estimate the average tracer arrival time (t_{ar}) [E2.13] and average tracer transport velocity (v) [E2.14], where t_{inj} represents the dual-tracer solution injection time (Wolff et al., 1979; Yu et al., 1999; Devine et al., 2003).

$$M_1 = \frac{m_1}{m_0} = \frac{\int_0^{t_f} tC(x,t)dt}{\int_0^{t_f} C(x,t)dt} \cong \frac{\sum_{n=0}^{f}\left(\frac{t_n C_n + t_{n-1} C_{n-1}}{2}\right)(t_n - t_{n-1})}{\sum_{n=0}^{f}\left(\frac{C_n + C_{n-1}}{2}\right)(t_n - t_{n-1})} \quad \text{[E2.12]}$$

$$t_{ar} = M_1 - \frac{t_{inj}}{2} \quad \text{[E2.13]}$$

$$v = \frac{L}{t_{\mathrm{ar}}} \qquad \text{[E2.14]}$$

Tracer retardation factors (R) were estimated for Br and CNPs as the ratio of average pore water velocity (v_{w}) [E2.15] to the average tracer transport velocity (v) [E2.16]. Since Br is a conservative tracer ($R \approx 1$), its average rate of transport should be similar to water ($v_{\mathrm{w}} \approx v$). Any retarded solute or particle will have an average transport velocity less than that of water ($R > 1$).

$$v_{\mathrm{w}} = \frac{Q}{A\phi} \qquad \text{[E2.15]}$$

$$R = \frac{v_{\mathrm{w}}}{v} \qquad \text{[E2.16]}$$

The second central moment (μ_2) represents the variance of tracer arrival times [E2.17] (Wolff et al., 1979; Yu et al., 1999). For constant finite pulse tracer injections, like those used in this study, a tracer's μ_2 is related to the dispersion coefficient (D) [E2.18] (Wolff et al., 1979; Yu et al., 1999).

$$\mu_2 = \frac{\int_0^{t_{\mathrm{f}}} (t - M_1)^2 C(x,t)\,dt}{\int_0^{t_{\mathrm{f}}} C(x,t)\,dt} \cong \frac{\sum_{\mathrm{n}=0}^{\mathrm{f}} \left(\frac{(t_{\mathrm{n}} - M_1)^2 C_{\mathrm{n}} + (t_{\mathrm{n}-1} - M_1)^2 C_{\mathrm{n}-1}}{2} \right) (t_{\mathrm{n}} - t_{\mathrm{n}-1})}{\sum_{\mathrm{n}=0}^{\mathrm{f}} \left(\frac{C_{\mathrm{n}} + C_{\mathrm{n}-1}}{2} \right) (t_{\mathrm{n}} - t_{\mathrm{n}-1})} \qquad \text{[E2.17]}$$

$$D = \frac{v^3}{2L} \left(\mu_2 - \frac{t_{\mathrm{inj}}^2}{12} \right) \qquad \text{[E2.18]}$$

This equation for D assumes that all tracer spreading can be attributed to dispersion and does not account for reversible sorption processes. Since $v < v_{\mathrm{w}}$ for retarded solutes and particles, D will only be accurately estimated from μ_2 and v of nonretarded conservative tracers. One-dimensional D is a function of aquifer and tracer properties, where α_{L} and D_{m} represent longitudinal dispersivity and the molecular diffusion coefficient, respectively [E2.19]. However, considering the flow rates and

assumed homogeneous matrices used in this study, D_m is assumed to minimally influence D, and D is essentially a result of tortuous flow through interconnected matrix pores. Therefore, if CNP transport is similar to Br transport, D estimates from both tracers' BTCs should be approximately equal for any given column experiment.

$$D = \alpha_L v + D_m \quad \text{[E2.19]}$$

According to Yu and others (1999), the TMM discussed hitherto (TMM1) can produce inaccurate parameter estimates when pulse injections are "long." Estimation inaccuracies are commonly related to tracer elution tailing (Wolff et al., 1979; Yu et al., 1999). Furthermore, errors associated with lower-order moments are exacerbated in higher-order moment analyses since μ_2 depends on the squared difference of sample time and the normalized first temporal moment [E2.17] (Yu et al., 1999). To address potential parameter estimation errors associated with the pulse injection times used in this study, a second TMM approach, TMM2, was used.

As developed by Yu and others (1999), TMM2 is capable of estimating transport parameters from BTCs generated from long pulse, or step, injections. Unlike TMM1, this TMM involves integrating BTCs with respect to effluent concentration rather than time. Similar to TMM1, M_1 and μ_2 were estimated with TMM2 using the trapezoid rule [E2.20, E2.21] (Yu et al., 1999). These temporal moment values were used to estimate v [2.22] and D [E2.23] (Yu et al., 1999). For comparison, CNP and Br R were also estimated from TMM2-derived v values.

$$M_1 = \int_0^1 t dC \cong \sum_{n=0}^{f} \left(\frac{t_n + t_{n-1}}{2}\right)(C_n - C_{n-1}) \quad \text{[E2.20]}$$

$$\mu_2 = \int_0^1 (t - M_1)^2 dC \cong \sum_{n=0}^{f} \left(\frac{(t_n - M_1)^2 + (t_{n-1} - M_1)^2}{2}\right)(C_n - C_{n-1}) \quad \text{[E2.21]}$$

$$v = \frac{L}{M_1} \quad \text{[E2.22]}$$

$$D = \frac{\mu_2 v^3}{2L} \quad \text{[E2.23]}$$

Since TMM2 integrates BTC data with respect to concentration from C/C_0=0 to C/C_0=1, tracer BTCs were divided into input and output steps at t=t_{inj} (i.e. time at which the dual-tracer injection ends and the background solution flush begins). For additional comparison of TMM parameter estimates, input and output steps were analyzed independently. While TMM1 was capable of estimating transport parameters for observed and modeled tracer BTCs, slightly erratic tracer concentration measurements near C/C_0=1 prevented application of TMM2 to observed BTC data. Unacceptable transport parameter estimates resulted from applying the trapezoid rule to observed data in which tracer concentrations are not consistently increasing or decreasing. However, since CXTFIT 2.1 does not allow modeled concentration data to erratically fluctuate above and below C/C_0=1, TMM2 was capable of analyzing modeled tracer BTC data. In summary, TMM1 and TMM2 produced four independent sets of transport parameter estimates (i.e. v, R, and D) for each experiment: TMM1 was applied to observed and modeled tracer BTCs, while TMM2 was applied to input and output steps of modeled tracer BTCs.

Inverse Modeling

Breakthrough curve data were inversely modeled with CXTFIT 2.1 to estimate tracer transport parameters. The CXTFIT 2.1 code is commonly used to match observed solute BTCs with fitted BTCs that represent analytical solutions to the governing ADE. This curve fitting is optimized by an iterative nonlinear least-squares regression method and user-supplied transport parameter estimates (Toride et al., 1995). The version of the ADE presented here describes non-reactive

solute transport during 1D steady-state flow in saturated, homogeneous, isotropic porous media [E2.24] (van Genuchten and Alves, 1982; Toride et al., 1995; Yu et al., 1999).

$$\frac{\partial C}{\partial t} = D\frac{\partial^2 C}{\partial x^2} - v_{\mathrm{w}}\frac{\partial C}{\partial x} \qquad \text{[E2.24]}$$

The CXTFIT 2.1 program can also be used to model transport of reactive solutes by including terms that account for linear equilibrium adsorption, degradation, and production, where μ_{d} is the first-order decay coefficient and γ is the zero-order production term [E2.25]. According to Toride and others (1995), R depends on volumetric water content. However, since this study deals exclusively with saturated conditions, volumetric water content is equal to and has been replaced with ϕ in all forms of the ADE discussed herein. Therefore, in this study, R is defined as a function of ϕ, ρ_{b}, and the empirical distribution constant (K_{d}) that represents the ratio of solute concentrations in liquid and adsorbed phases [E2.26] (van Genuchten and Alves, 1982; Toride et al., 1995). Since no mechanisms for tracer degradation or production exist in this study, μ_{d} and γ are ignored and the modified equilibrium ADE is reduced [E2.27].

$$R\frac{\partial C}{\partial t} = D\frac{\partial^2 C}{\partial x^2} - v_{\mathrm{w}}\frac{\partial C}{\partial x} - \mu_{\mathrm{d}}C + \gamma(x) \qquad \text{[E2.25]}$$

$$R = 1 + \frac{\rho_{\mathrm{b}}K_{\mathrm{d}}}{\phi} \qquad \text{[E2.26]}$$

$$R\frac{\partial C}{\partial t} = D\frac{\partial^2 C}{\partial x^2} - v_{\mathrm{w}}\frac{\partial C}{\partial x} \qquad \text{[E2.27]}$$

Additionally, CXTFIT 2.1 can incorporate terms that account for chemical nonequilibrium transport conditions. The chemical nonequilibrium, or two-site, model considers two types of sorption sites (Type 1 and Type 2). Type 1 sites are associated with equilibrium, or instantaneous,

sorption, while Type 2 sites are associated with first-order kinetic, or time-dependent, sorption (van Genuchten and Wagenet, 1989; Toride et al., 1995). As included in the two-site chemical nonequilibrium ADE, f is the fraction of equilibrium adsorption sites (i.e. Type 1 sites), α is a first-order kinetic rate coefficient, and s_k is the concentration of a given tracer adsorbed to Type 2 sites [E2.28] (Toride et al., 1995).

$$\left(1+\frac{f\rho_b K_d}{\phi}\right)\frac{\partial C}{\partial t} = D\frac{\partial^2 C}{\partial x^2} - v_w\frac{\partial C}{\partial x} - \frac{\alpha\rho_b}{\phi}[(1-f)K_d C - s_k] \qquad \text{[E2.28]}$$

As required for CXTFIT 2.1 modeling operations, any dimensional input parameters are automatically converted to their dimensionless equivalents. Table 2.05 summarizes the equations used by CXTFIT 2.1 to perform such internal conversions. These converted parameters are then applied to dimensionless versions of the equilibrium ADE [E2.29] and nonequilibrium ADE [E2.30]. The dimensionless equilibrium ADE includes terms for the Peclet number (P) and dimensionless time (T_d), length (X), and concentration (C_1) [E2.29] (Table 2.05). As defined in Table 2.05, P represents the ratio of advective to dispersive tracer transport. The dimensionless nonequilibrium ADE incorporates variables for C adsorbed to equilibrium and nonequilibrium sites (C_1 and C_2, respectively), a tracer partitioning coefficient (β), and a tracer mass transfer coefficient (ω) [E2.30] (Table 2.05) (Toride et al., 1995).

$$R\frac{\partial C_1}{\partial T_d} = \frac{1}{P}\frac{\partial^2 C_1}{\partial X^2} - \frac{\partial C_1}{\partial X} \qquad \text{[E2.29]}$$

$$\beta R\frac{\partial C_1}{\partial T_d} = \frac{1}{P}\frac{\partial^2 C_1}{\partial X^2} - \frac{\partial C_1}{\partial X} - \omega(C_1 - C_2) \qquad \text{[E2.30]}$$

Table 2.05: Dimensionless parameters included in [E2.29] and [E2.30] (Toride et al., 1995)

Parameter	T_d	X	P	R	β	ω	C_1	C_2
Equation	$\frac{v_w t}{L}$	$\frac{x}{L}$	$\frac{v_w L}{D}$	$1+\frac{\rho_b K_d}{\phi}$	$\frac{\phi + f\rho_b K_d}{\phi + \rho_b K_d}$	$\frac{\alpha(1-\beta)RL}{v}$	$\frac{C}{C_0}$	$\frac{s_k}{(1-f)K_d C_0}$

To generate representative tracer transport models, the appropriate form of the ADE was selected for each column experiment. The deterministic equilibrium ADE [E2.27, E2.29] was initially used to model Br and CNP transport. Similar to BTC modeling performed by King (2015), Br transport was successfully modeled using this governing equation. However, due to the equilibrium ADE's neglect of apparent CNP adsorption processes, CNP transport was modeled with the deterministic two-site chemical nonequilibrium ADE [E2.28, E2.30].

The same concentration mode, initial conditions, and boundary conditions apply to all column experiments. A flux-averaged concentration mode was chosen, as is appropriate for modeling BTCs representing column effluent sample concentrations (Toride et al., 1995). Since columns were saturated with tracer-free background solutions prior to the dual-tracer injection start time (t=0), the models' initial conditions are defined by [E2.31]. The inlet boundary condition reflects the use of a finite dual-tracer pulse injection from t=0 to t=t_{inj}, followed by a tracer-free background solution flush (C_0=0) [E2.32] (van Genuchten and Alves, 1982). The outlet boundary condition, selected for tracer pulse injections, assumes a semi-infinite column length [E2.33] (van Genuchten and Alves, 1982; Toride et al., 1995). As shown in [E2.31], [E2.32], and [E2.33], C represents tracer concentration as a function of column length (x) and transport time (t).

$$C(x,0) = 0 \qquad (t = 0) \qquad \text{[E2.31]}$$

$$C(0,t) = \begin{cases} C_0 & 0 < t < t_{\text{inj}} \\ 0 & t > t_{\text{inj}} \end{cases} \qquad (x = 0) \qquad \text{[E2.32]}$$

$$\frac{\partial C}{\partial x}(\infty, t) = 0 \qquad (x = \infty) \qquad \text{[E2.33]}$$

Initial transport parameter estimates were determined prior to inverse modeling. For all models, the calculated v_w [E2.15] and TMM1-derived estimates of D and R were input to CXTFIT 2.1. While v_w was input as a known parameter, D and R were subject to parameter estimation. For CNP models, which were governed by the chemical nonequilibrium ADE [E2.28, E2.30], estimates of β and ω were also produced after reasonable initial estimates were provided. Finally, observed CNP and Br BTC data were input, and analytical solutions were generated for each column experiment.

CHAPTER 3: RESULTS

Four column experiments were conducted to observe and model carbon nanoparticle (CNP) transport in saturated homogeneous porous media under controlled pHs and dissolved organic matter (DOM) concentrations. To compare CNP transport to that of bromide (Br), a known conservative tracer, effluent tracer concentrations (C) were presented as breakthrough curves (BTCs). These BTC data were analyzed with temporal moment methods (TMMs) and modeled with CXTFIT 2.1 to estimate tracer transport parameters. Each modeled BTC's goodness of fit was quantified as the coefficient of determination (r^2) and mean squared error (MSE). Observed and modeled BTCs and resultant transport estimates are presented herein for each column experiment.

Experiment 1

Experiment 1 (E1) was conducted with acidic solutions (pH 4) containing DOM (4 parts per million (ppm) Pahokee Peat humic acid (PPHA)). As evidenced by their similarly shaped BTCs, Br and CNPs transport comparably under these conditions (Figure 3.01). Observed Br and CNP concentrations begin to sharply increase once 0.68 and 0.83 pore volumes (PVs) of dual-tracer solution had been injected ($PV \approx 0.68$ and $PV \approx 0.83$), respectively. Concentrations of Br and CNPs responded similarly to the tracer-free background solution flush by rapidly declining at $PV \approx 5.4$ and $PV \approx 5.6$, respectively. While each tracer's BTCs plateau after reaching their maximum concentrations, CNPs were observed reaching a peak concentration approximately 1.8 PVs after Br. (As observed in multiple experiments, ratios of C to influent tracer concentrations (C_0) exceeding $C/C_0=1$ are most likely analytical artifacts.) Tracer transport is also distinguished by a

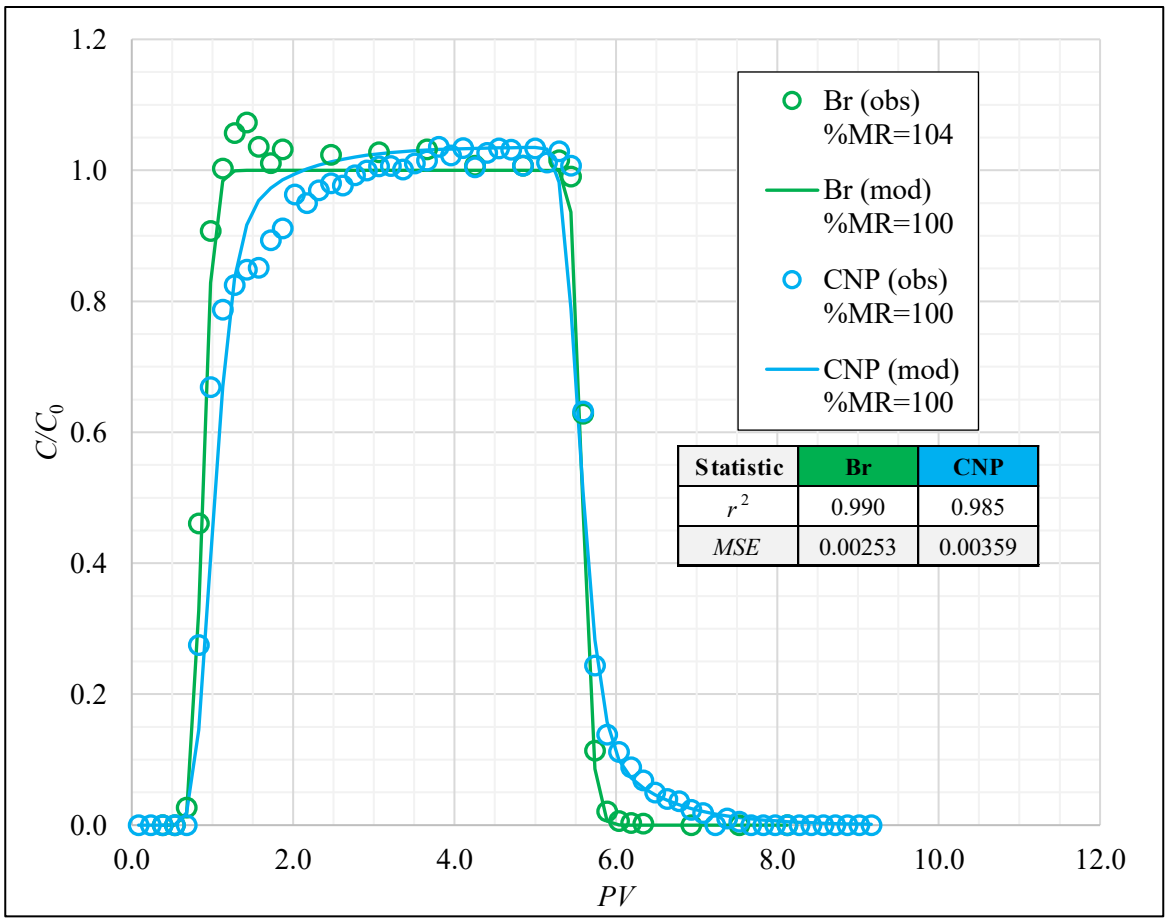

Figure 3.01: Observed ("obs", hollow circles) and modeled ("mod", solid lines) BTCs for E1 (pH 4, 4 ppm PPHA). A statistical summary (table, right of the BTCs) describes the modeled data's goodness of fit. The %MR values calculated from each BTC are included in the legend.

slightly more pronounced CNP elution tail. While complete Br elution was observed by $PV \approx 6.9$, CNP concentrations declined more gradually until returning to $C/C_0=0$ at $PV \approx 7.2$. Modeled BTCs fit observed data well as indicated by r^2 values near unity ($r^2_{Br}=0.990$, $r^2_{CNP}=0.985$) and low MSE values ($MSE_{Br}=0.00253$, $MSE_{CNP}=0.00359$) (Figure 3.01).

In addition to fitting BTCs, inverse modeling produced estimates of CNP and Br transport parameters (Table 3.01). As shown in Table 3.01, average pore water velocity (v_w) was input as calculated from the measured flow rate, column cross-sectional area, and porosity [E2.15]. Conversely, tracer retardation (R), dispersion (D), partitioning (β), and mass transfer (ω) coefficients are estimated transport parameters. Under these experimental conditions, CNP

transport is minimally retarded (R_{CNP}=1.10 ± 0.06) and Br transport is unimpeded (R_{Br}=0.857 ± 0.017). While estimates of CNP and Br D are within an order of magnitude, CNP D is 170% greater than that of Br (D_{CNP}=0.0460 ± 0.0317 cm^2/min, D_{Br}=0.0172 ± 0.0084 cm^2/min). Modeling CNP transport with the chemical nonequilibrium advection-dispersion equation (ADE) [E2.30] enabled estimation of β (β_{CNP}=0.910 ± 0.068) and ω (ω_{CNP}=0.145 ± 0.258). Like all other experiments in this study, β and ω estimates were not produced for Br since this known conservative tracer was appropriately modeled using the equilibrium ADE [E2.29] (i.e. β_{Br}=1, ω_{Br}=0).

Table 3.01: Summary of E1 transport parameters estimated via CXTFIT 2.1 inverse modeling

Parameter	**Br**			**CNP**		
	Estimate	**95% confidence interval**		**Estimate**	**95% confidence interval**	
v_w (cm/min)	0.198			0.198		
R*	0.857	0.840	0.873	1.10	1.04	1.16
D* (cm^2/min)	0.0172	0.00880	0.0255	0.0460	0.0143	0.0777
β*				0.910	0.842	0.978
ω*				0.145	-0.113	0.403

*fitted parameter

Multiple TMM analyses were performed to estimate tracer mass recovery (%MR) and transport parameters (i.e. v, R, and D) for all experiments (Figure 3.01, Table 3.02). According to the zeroth temporal moment analyses for observed and modeled CNP and Br BTCs [E2.10, E2.11], approximately 100% of tracer masses were recovered in E1 (Figure 3.01). In Table 3.02, methods "TMM1$_{obs}$" and "TMM1$_{mod}$" refer to TMM1 analyses performed on observed and modeled BTCs, respectively [E2.10, E2.12-2.14, E2.16-2.18]. Additionally, "TMM2$_{in}$" and "TMM2$_{out}$" refer to TMM2 analyses performed on modeled input (i.e. dual-tracer solution injection) and output (i.e. background solution flush) steps, respectively [E2.16, E2.20-E2.23]. In E1, all TMM-derived estimates for any individual transport parameter are within one order of magnitude. In comparing mean TMM-derived parameter values, CNPs were transported 18% slower than Br (v_{CNP}=0.191 ±

0.0102 cm/min, v_{Br}=0.232 ± 0.00100 cm/min). Additionally, CNP transport is associated with 21% more retardation (R_{CNP}=1.04 ± 0.0579, R_{Br}=0.857 ± 0.00367) and an 87% higher dispersion coefficient than Br transport (D_{CNP}=0.160 ± 0.0791 cm^2/min, D_{Br}=0.0855 ± 0.0619 cm^2/min).

Table 3.02: Summary of E1 transport parameters estimated via TMM1 and TMM2

Tracer	**Method**	**Parameter estimate**		
		***v* (cm/min)**	***R***	***D* (cm^2/min)**
Br	$TMM1_{obs}$	0.233	0.850	0.185
	$TMM1_{mod}$	0.231	0.859	0.0894
	$TMM2_{in}$	0.231	0.859	0.0336
	$TMM2_{out}$	0.231	0.859	0.0337
	mean	**0.232**	**0.857**	**0.0855**
	SD	**0.00100**	**0.00367**	**0.0619**
	***RSD* (%)**	**0.430**	**0.428**	**72.4**
CNP	$TMM1_{obs}$	0.194	1.02	0.117
	$TMM1_{mod}$	0.194	1.03	0.0843
	$TMM2_{in}$	0.175	1.14	0.147
	$TMM2_{out}$	0.203	0.979	0.291
	mean	**0.191**	**1.04**	**0.160**
	SD	**0.0102**	**0.0579**	**0.0791**
	***RSD* (%)**	**5.34**	**5.57**	**49.5**

SD=standard deviation; *RSD*=relative standard deviation

As discussed in the previous chapter, TMM1 can produce erroneous results in column experiments conducted with "long" tracer injection times (Yu et al., 1999). Therefore, to increase confidence in TMM-derived parameter estimates, modeled BTC data were also analyzed with TMM2. Low standard deviation (*SD*) and relative standard deviation (*RSD*) values indicate TMM1 and TMM2 precisely estimated CNP and Br *v* and *R* in E1 (Table 3.02). Nonetheless, CNP *v* and *R* estimates were less precise; their associated *RSD* values were approximately an order of magnitude greater than those of Br. This lower CNP precision is partially attributed to differences between $TMM2_{in}$ and $TMM2_{out}$ parameter estimates resulting from asymmetric BTCs. Precision was substantially

lower for CNP and Br *D* estimates. Such estimate variability results from asymmetric BTCs and the inherent exacerbation of analytical errors in higher-order temporal moment analyses (Yu et al., 1999). While TMM2 did not fully resolve this issue as desired, this method provided additional estimates of tracer *D* and more-robust statistics.

Experiment 2

Experiment 2 (E2) was conducted with acidic (pH 4), DOM-free (0 ppm PPHA) solutions. Under these experimental conditions, Br and CNPs transport comparably as indicated by their approximately matching BTCs (Figure 3.02). Observed tracer concentrations begin rapidly

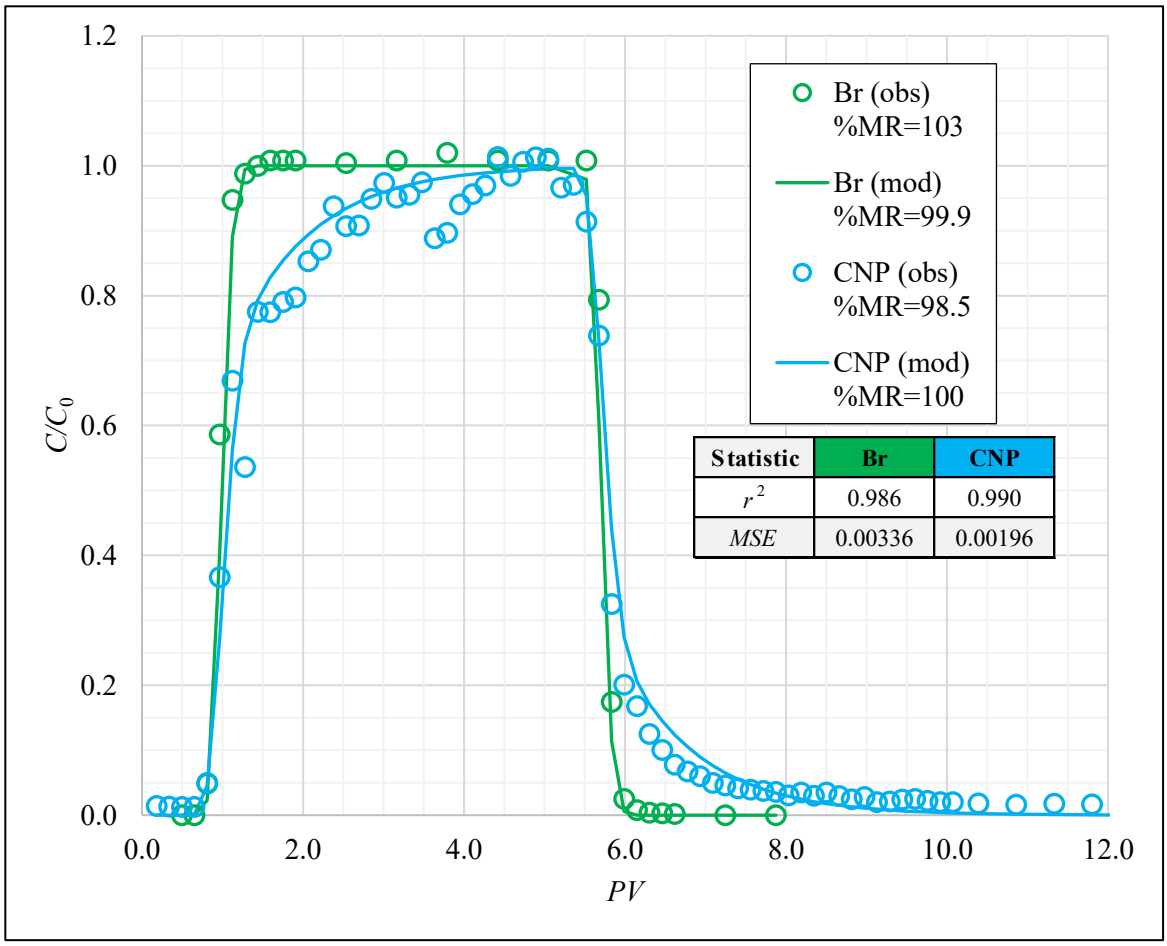

Figure 3.02: Observed ("obs", hollow circles) and modeled ("mod", solid lines) BTCs for E2 (pH 4, 0 ppm PPHA). A statistical summary (table, right of the BTCs) describes the modeled data's goodness of fit. The %MR values calculated from each BTC are included in the legend.

increasing at $PV \approx 0.81$ in response to the dual-tracer solution injection. Additionally, Br and CNP concentrations begin decreasing at $PV \approx 5.7$ and $PV \approx 5.5$, respectively, in response to the background solution injection. Both tracers reach $C/C_0=1$, but the rate at which CNP concentration peaks is slower than Br. While Br reaches $C/C_0=1$ at $PV \approx 1.4$, CNPs reach maximum concentration 3 PVs later at $PV \approx 4.4$. This difference is highlighted by the vertical displacement between Br and CNP BTCs as CNPs approach maximum concentration. Furthermore, both tracers return to $C/C_0=0$, but CNP elution tailing is more prominent. In fact, CNP elution continues for approximately 3.7 PVs after Br reaches $C/C_0=0$. Regardless of such observed differences, modeled tracer BTCs fit observed data well as indicated by r^2 values near unity ($r^2_{Br}=0.986$, $r^2_{CNP}=0.990$) and low *MSE* values ($MSE_{Br}=0.00336$, $MSE_{CNP}=0.00196$) (Figure 3.02).

Transport parameters estimated by modeling observed Br and CNP BTC data are summarized in Table 3.03. Like all experiments in this study, R and D were estimated for Br and CNPs; β and ω were estimated for CNPs only; and v_w was input as calculated prior to executing the column experiment [E2.15]. According to E2 inverse modeling results, Br transport is unimpeded and CNP transport is slightly retarded. More specifically, CNP R exceeds that of Br by 33% ($R_{CNP}=1.28 \pm 0.05$, $R_{Br}=0.965 \pm 0.020$). Estimates of D are also comparable (i.e. within an order of magnitude), but CNP D is 110% greater than that of Br ($D_{CNP}=0.0262 \pm 0.0166$ cm^2/min, $D_{Br}=0.0123 \pm 0.00753$

Table 3.03: Summary of E2 transport parameters estimated via CXTFIT 2.1 inverse modeling

Parameter	**Br**			**CNP**		
	Estimate	**95% confidence interval**		**Estimate**	**95% confidence interval**	
v_w (cm/min)	0.192			0.192		
R*	0.965	0.945	0.984	1.28	1.23	1.33
D* (cm^2/min)	0.0123	0.00477	0.0198	0.0262	0.00960	0.0428
β*				0.782	0.743	0.821
ω*				0.350	0.201	0.499

*fitted parameter

cm^2/min). Using the chemical nonequilibrium ADE, CNP β (β_{CNP}=0.782 ± 0.039) and ω (ω_{CNP}=0.350 ± 0.149) were also estimated (Table 3.03).

Nearly all injected tracer mass was recovered for Br and CNPs in E2 (Figure 3.02). Estimates of v, R, and D generated with TMM analyses are summarized in Table 3.04. For each tracer, mean estimates for any given transport parameter are within one order of magnitude. Relative to TMM-derived Br transport parameter estimates, CNP v is 26% less (v_{CNP}=0.148 ± 0.00673 cm/min, v_{Br}=0.199 ± 0.000697 cm/min); CNP R is 35% greater (R_{CNP}=1.30 ± 0.0617, R_{Br}=0.966 ± 0.00340); and CNP D is 590% greater (D_{CNP}=0.367 ± 0.194 cm^2/min, D_{Br}=0.0530 ± 0.0445 cm^2/min). While TMM analyses precisely estimated v and R for each tracer, *RSD* values for CNP v and R exceed those for Br by more than an order of magnitude. Estimates of Br and CNP D are much less precise (Table 3.04).

Table 3.04: Summary of E2 transport parameters estimated via TMM1 and TMM2

Tracer	**Method**	**Parameter estimate**		
		***v* (cm/min)**	***R***	***D* (cm^2/min)**
Br	$TMM1_{obs}$	0.198	0.972	0.134
	$TMM1_{mod}$	0.199	0.965	0.0588
	$TMM2_{in}$	0.199	0.966	0.0229
	$TMM2_{out}$	0.200	0.963	0.0272
	mean	**0.199**	**0.966**	**0.0530**
	SD	**0.000697**	**0.00340**	**0.0445**
	***RSD* (%)**	**0.350**	**0.351**	**73.3**
CNP	$TMM1_{obs}$	0.137	1.40	0.702
	$TMM1_{mod}$	0.150	1.28	0.270
	$TMM2_{in}$	0.155	1.24	0.222
	$TMM2_{out}$	0.151	1.27	0.275
	mean	**0.148**	**1.30**	**0.367**
	SD	**0.00673**	**0.0617**	**0.194**
	***RSD* (%)**	**4.54**	**4.74**	**52.9**

Experiment 3

Experiment 3 (E3) was conducted with neutral solutions (pH 7) containing DOM (4 ppm PPHA). Considering their BTCs mostly overlap, Br and CNP transport is comparable under these experimental conditions (Figure 3.03). Observed tracer concentrations sharply increase at $PV \approx 0.89$. However, while Br concentration peaks at $PV \approx 1.8$, CNP concentration increases gradually until reaching $C/C_0=1$ at $PV \approx 4.0$. This difference in rates of increasing tracer concentrations is highlighted by the vertical offset of BTCs as CNPs approach maximum concentration. Similarly, CNP and Br concentrations begin rapidly declining at $PV \approx 5.7$ and

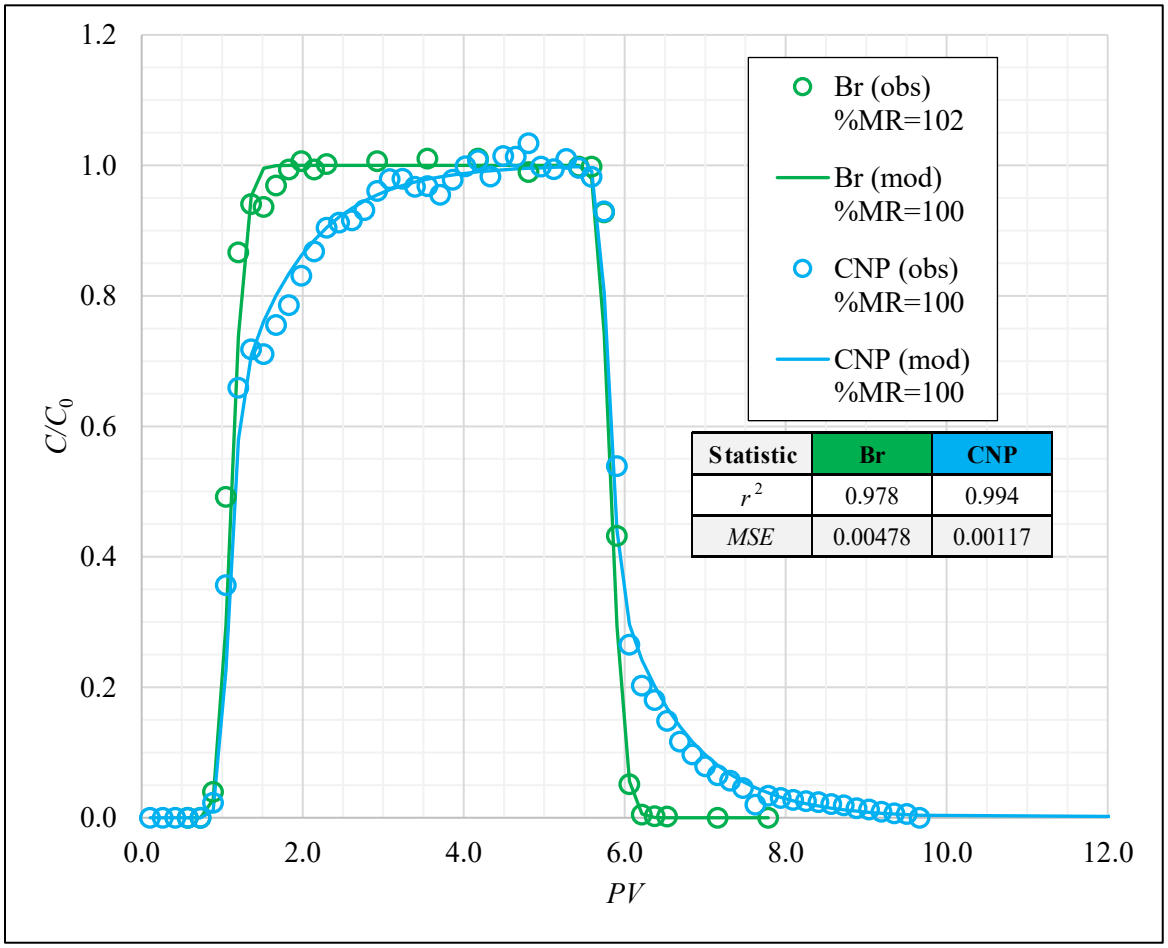

Figure 3.03: Observed ("obs", hollow circles) and modeled ("mod", solid lines) BTCs for E3 (pH 7, 4 ppm PPHA). A statistical summary (table, right of the BTCs) describes the modeled data's goodness of fit. The %MR values calculated from each BTC are included in the legend.

PV≈5.6, respectively. However, CNPs are eluted more gradually than Br. While Br concentrations return to C/C_0=0 at PV≈7.2, CNP elution continues for 2.5 PVs until CNPs reach C/C_0=0 at PV≈9.7. Regardless of these apparent differences, r^2 values near unity (r^2_{Br}=0.978, r^2_{CNP}=0.994) and low MSE values (MSE_{Br}=0.00478, MSE_{CNP}=0.00117) indicate modeled Br and CNP BTCs fit their observed data well (Figure 3.03).

Modeled transport parameter estimates are summarized in Table 3.05. These estimated parameters indicate that, under E3 conditions, Br and CNP transport is minimally retarded and tracer dispersion is similar. While neither tracer is substantially retarded, CNP transport is 27% more retarded than Br transport (R_{CNP}=1.38 ± 0.04, R_{Br}=1.09 ± 0.03). Additionally, CNP D is 37% less than that of Br (D_{CNP}=0.0109 ± 0.00713 cm^2/min, D_{Br}=0.0174 ± 0.0102 cm^2/min). Estimates of CNP β (β_{CNP}=0.770 ± 0.025) and ω (ω_{CNP}=0.487 ± 0.126) are also included in Table 3.05.

Table 3.05: Summary of E3 transport parameters estimated via CXTFIT 2.1 inverse modeling

Parameter	**Br**			**CNP**		
	Estimate	**95% confidence interval**		**Estimate**	**95% confidence interval**	
v_w (cm/min)	0.201			0.201		
R*	1.09	1.06	1.12	1.38	1.34	1.42
D* (cm^2/min)	0.0174	0.00724	0.0275	0.0109	0.00377	0.0180
β*				0.770	0.745	0.794
ω*				0.487	0.361	0.613

*fitted parameter

According to TMM analyses of observed and modeled BTCs, all injected Br and CNP mass was recovered in E3 (Figure 3.03). Table 3.06 summarizes TMM-derived estimates of tracer v, R, and D for E3. For each tracer, mean estimates for any given transport parameter are within one order of magnitude. Relative to transport parameter estimates for Br, estimated CNP v is 21% less (v_{CNP}=0.146 ± 0.00146 cm/min, v_{Br}=0.184 ± 0.000360 cm/min); CNP R is 26% greater (R_{CNP}=1.37 ± 0.0136, R_{Br}=1.09 ± 0.00214); and CNP D is 290% greater (D_{CNP}=0.209 ± 0.0243 cm^2/min,

D_{Br}=0.0530 ± 0.0366 cm^2/min). As evidenced by *RSD* values less than 1%, TMM analyses precisely estimate Br and CNP *v* and *R* under E3 conditions. However, tracer *D* estimates are much more variable (Table 3.06).

Table 3.06: Summary of E3 transport parameters estimated via TMM1 and TMM2

Tracer	Method	Parameter estimate		
		***v* (cm/min)**	***R***	***D* (cm^2/min)**
Br	$TMM1_{obs}$	0.183	1.09	0.113
	$TMM1_{mod}$	0.184	1.09	0.0526
	$TMM2_{in}$	0.184	1.09	0.0233
	$TMM2_{out}$	0.184	1.09	0.0233
	mean	**0.184**	**1.09**	**0.0530**
	SD	**0.000360**	**0.00214**	**0.0366**
	***RSD* (%)**	**0.196**	**0.196**	**68.9**
CNP	$TMM1_{obs}$	0.147	1.37	0.200
	$TMM1_{mod}$	0.145	1.39	0.217
	$TMM2_{in}$	0.149	1.35	0.177
	$TMM2_{out}$	0.145	1.38	0.244
	mean	**0.146**	**1.37**	**0.209**
	SD	**0.00146**	**0.0136**	**0.0243**
	***RSD* (%)**	**0.996**	**0.991**	**11.6**

Experiment 4

Experiment 4 (E4) was conducted with neutral solutions (pH 7) absent DOM (0 ppm PPHA). Under these experimental conditions, Br and CNPs first arrive at $PV \approx 0.89$ and $PV \approx 1.0$, respectively (Figure 3.04). As highlighted by the significant vertical displacement of BTCs, Br and CNPs approach maximum concentrations at different rates. While Br concentration rapidly increases to C/C_0=1 over 1.1 PVs, CNP concentration sharply, then gradually increases for 4.5 PVs until peaking at C/C_0=0.95. Observed and modeled CNP BTC trends suggest CNPs might

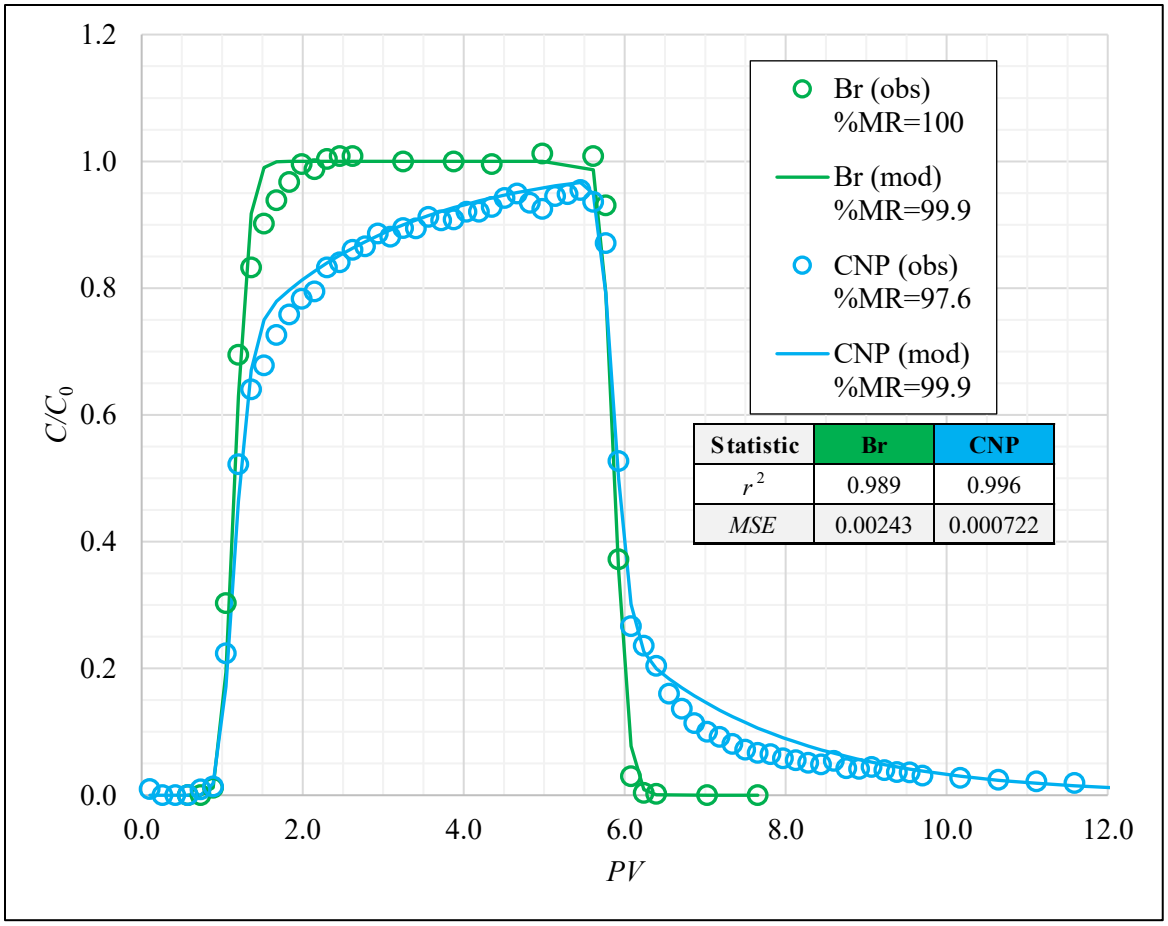

Figure 3.04: Observed ("obs", hollow circles) and modeled ("mod", solid lines) BTCs for E4 (pH 7, 0 ppm PPHA). A statistical summary (table, right of the BTCs) describes the modeled data's goodness of fit. The %MR values calculated from each BTC are included in the legend.

have reached C/C_0=1 at PV≈7 with an extended dual-tracer injection. As clearly displayed by overlying BTCs, CNP elution tailing is much more prominent than that of Br in E4. In fact, CNP elution continued for 6.5 PVs beyond the time at which Br returned to C/C_0=0. Modeled Br and CNP BTCs fit their respective observed data well, as indicated by r^2 values near unity (r^2_{Br}=0.989, r^2_{CNP}=0.996) and low MSE values (MSE_{Br}=0.00243, MSE_{CNP}=0.000722) (Figure 3.04).

Modeled Br and CNP transport parameter estimates are summarized in Table 3.07. Under E4 experimental conditions, CNP transport is 49% more retarded than Br transport (R_{CNP}=1.68 ± 0.06, R_{Br}=1.13 ± 0.02). Additionally, CNP D is 31% greater than that of Br (D_{CNP}=0.0217 ± 0.007

cm^2/min, D_{Br}=0.0166 ± 0.0068 cm^2/min). According to the chemical nonequilibrium ADE, CNP β (β_{CNP}=0.677 ± 0.022) and ω (ω_{CNP}=0.328 ± 0.042) were also estimated (Table 3.07).

Table 3.07: Summary of E4 transport parameters estimated via CXTFIT 2.1 inverse modeling

Parameter	**Br**			**CNP**		
	Estimate	**95% confidence interval**		**Estimate**	**95% confidence interval**	
v_w (cm/min)	0.198			0.198		
R*	1.13	1.11	1.15	1.68	1.62	1.73
D* (cm^2/min)	0.0166	0.00978	0.0234	0.0217	0.0147	0.0287
β*				0.677	0.655	0.699
ω*				0.328	0.286	0.370

*fitted parameter

As estimated for observed and modeled tracer BTCs, nearly all injected Br and CNP mass was recovered in E4 (Figure 3.04). However, this study's lowest %MR was observed in E4 as 97.6% of CNP mass was recovered. Estimates of v, R, and D derived from TMM analyses are summarized in Table 3.08. All TMM-derived estimates of v and R are within an order of magnitude. In this

Table 3.08: Summary of E4 transport parameters estimated via TMM1 and TMM2

Tracer	**Method**	**Parameter estimate**		
		***v* (cm/min)**	***R***	***D* (cm^2/min)**
Br	$TMM1_{obs}$	0.173	1.15	0.0543
	$TMM1_{mod}$	0.175	1.13	0.0425
	$TMM2_{in}$	0.175	1.13	0.0213
	$TMM2_{out}$	0.176	1.13	0.0250
	mean	**0.175**	**1.13**	**0.0358**
	SD	**0.00107**	**0.00699**	**0.0134**
	***RSD* (%)**	**0.612**	**0.616**	**37.4**
CNP	$TMM1_{obs}$	0.120	1.65	0.511
	$TMM1_{mod}$	0.119	1.66	0.438
	$TMM2_{in}$	0.145	1.36	0.241
	$TMM2_{out}$	0.126	1.58	0.484
	mean	**0.128**	**1.56**	**0.419**
	SD	**0.0105**	**0.120**	**0.106**
	***RSD* (%)**	**8.27**	**7.67**	**25.2**

experiment, CNP transport is 27% slower (v_{CNP}=0.128 ± 0.0105 cm/min, v_{Br}=0.175 ± 0.00107 cm/min) and 38% more retarded than Br transport (R_{CNP}=1.56 ± 0.120, R_{Br}=1.13 ± 0.00699). While *v* and *R* estimates are similar, CNP *D* is over an order of magnitude (1,100%) greater than that of Br (D_{CNP}=0.419 ± 0.106 cm^2/min, D_{Br}=0.0358 ± 0.0134 cm^2/min). Excluding *D*, TMM analyses precisely estimated tracer transport parameters as indicated by low *RSD* values (Table 3.08).

Summary of Results

Generally, CNPs and Br were transported similarly in all experiments of this study. Nonetheless, transport distinctions are evident when observed and modeled BTCs from multiple experiments are plotted concurrently. As shown in Figure 3.05, Br BTCs are nearly identical under all

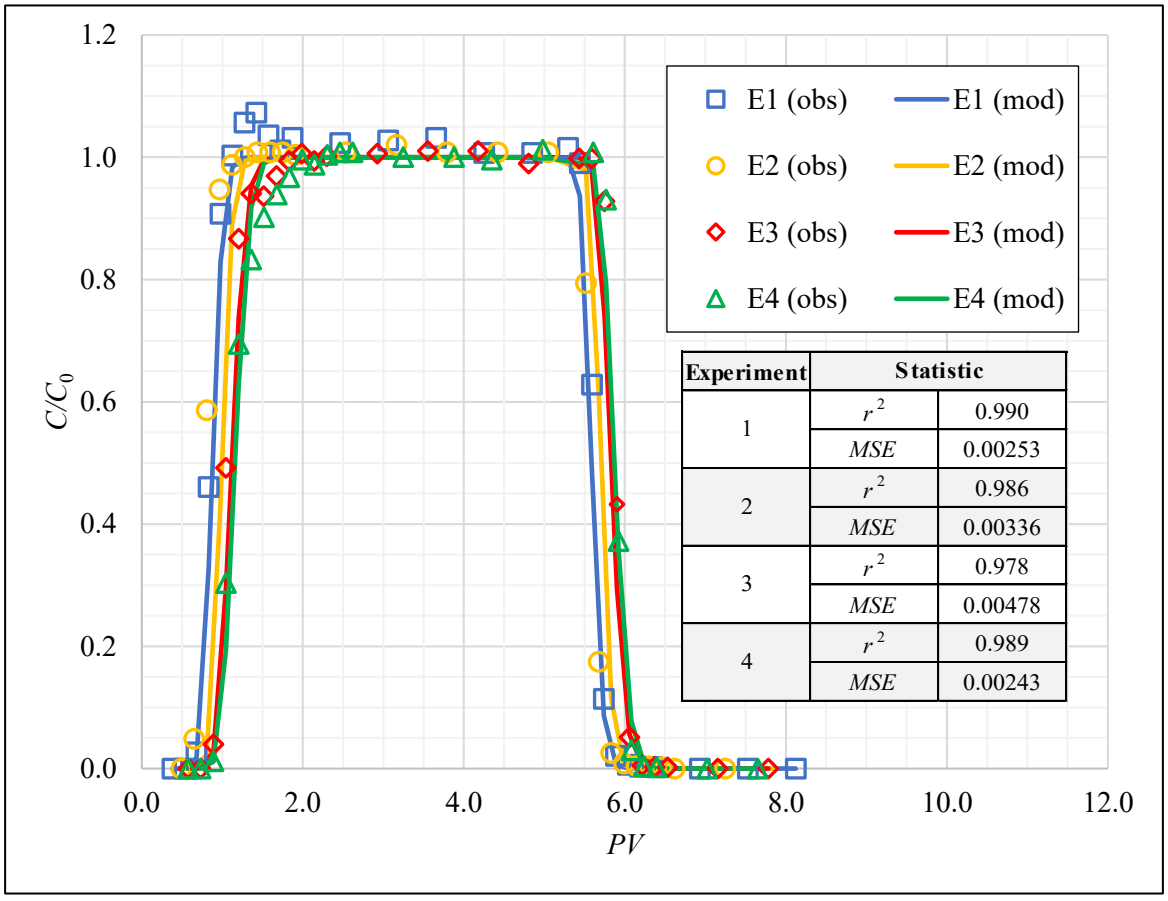

Experiment	Statistic	
1	r^2	0.990
	MSE	0.00253
2	r^2	0.986
	MSE	0.00336
3	r^2	0.978
	MSE	0.00478
4	r^2	0.989
	MSE	0.00243

Figure 3.05: Observed ("obs", hollow shapes) and modeled ("mod", solid lines) Br BTCs for E1-E4. A statistical summary (table, right of the BTCs) describes the modeled data's goodness of fit.

experimental conditions. However, slight differences are apparent: Br BTCs are separated in the x-direction, and observed and modeled data are vertically offset between approximately C/C_0=0.9 and maximum concentrations (Figure 3.05). More prominent transport differences are observed among overlain CNP BTCs (Figure 3.06). In addition to being slightly separated in the x-direction, observed and modeled CNP BTCs are distinguished by varying degrees of vertical offset as they approach maximum concentration and as CNPs are eluted from the column. Nonetheless, the apparent representativeness of fitted BTCs and strong goodness-of-fit values (i.e. $r^2 \approx 1$, low *MSE*) indicate CNP transport might be accurately modeled as solutes using CXTFIT 2.1. However,

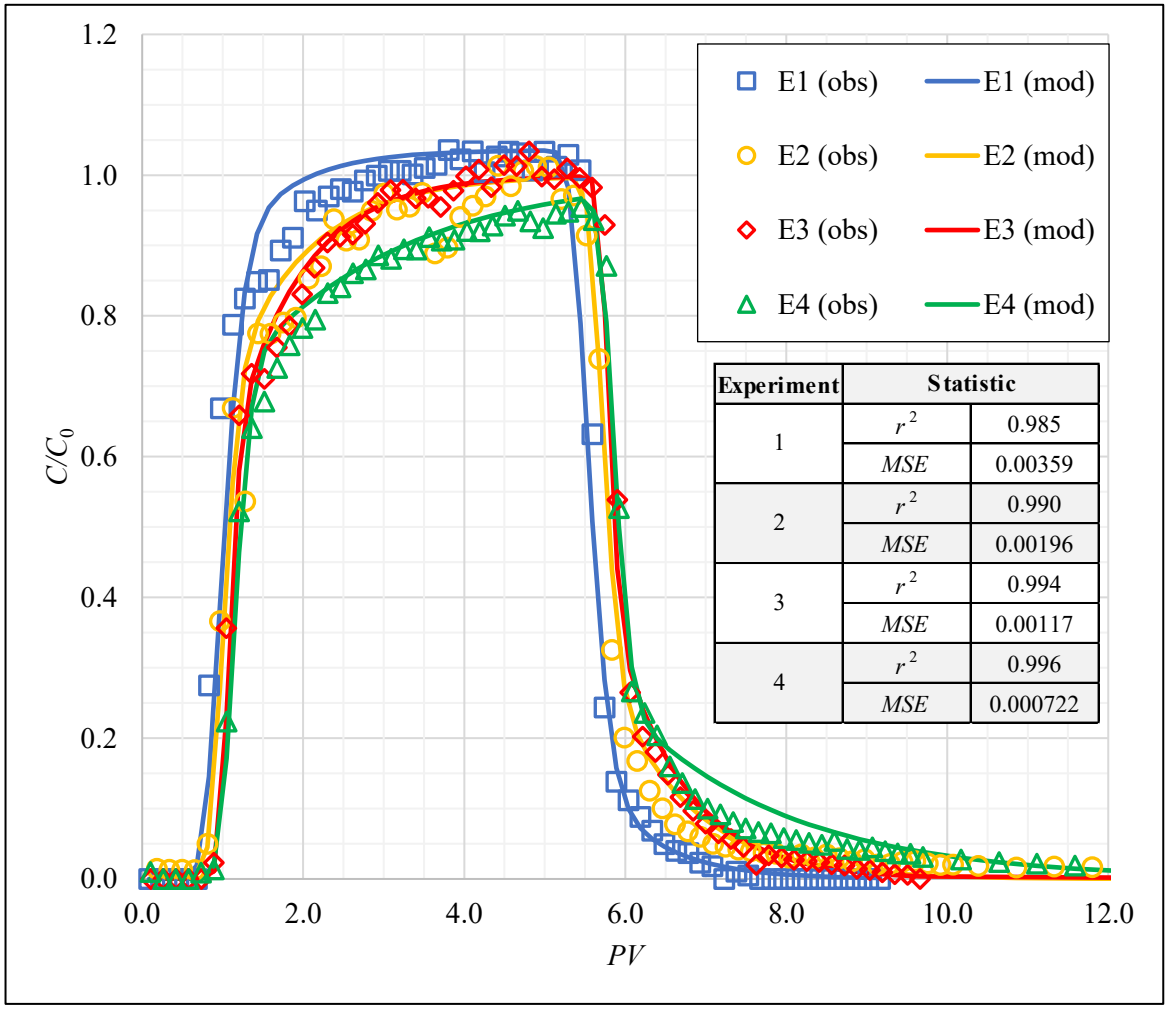

Experiment	Statistic	
1	r^2	0.985
	MSE	0.00359
2	r^2	0.990
	MSE	0.00196
3	r^2	0.994
	MSE	0.00117
4	r^2	0.996
	MSE	0.000722

Figure 3.06: Observed ("obs", hollow shapes) and modeled ("mod", solid lines) CNP BTCs for E1-E4. A statistical summary (table, right of the BTCs) describes the modeled data's goodness of fit.

determining the accuracy of this modeling method requires assessing the physical significance and appropriateness of CNP transport parameter estimates.

Tracer transport can be distinguished more quantitatively by comparing estimated transport parameters (Tables 3.09 and 3.10). As shown in Table 3.09, TMM-derived estimates of Br v exceed the calculated v_w in experiments with acidic solutions (i.e. E1 and E2). Conversely, Br v estimates are less than the calculated v_w in experiments with neutral solutions (i.e. E3 and E4). Relative to calculated v_w, CNP v is underestimated by TMM analyses in all experiments. Considering the inverse relationship between tracer v and R, these tracer velocity estimates are supported by corresponding estimates of Br and CNP R. For a given tracer and experiment, modeled and TMM-derived estimates of R are similar. While unimpeded in E1 and E2, Br transport is minimally retarded in E3 and E4. Similar to Br, CNP R estimates increase from E1 to E4. Therefore, while CNP transport is minimally retarded throughout all experiments, CNP R is slightly greater in

Table 3.09: Summary of transport parameter estimates for E1-E4

Tracer	Experiment (conditions)	Method	Parameter		
			v (cm/min)	R	D (cm^2/min)
Br	1 (pH 4, 4 ppm PPHA)	inverse modeling	0.198*	0.857	0.0172
		TMM (mean)	0.232	0.857	0.0855
	2 (pH 4, 0 ppm PPHA)	inverse modeling	0.192*	0.965	0.0123
		TMM (mean)	0.199	0.966	0.0607
	3 (pH 7, 4 ppm PPHA)	inverse modeling	0.201*	1.09	0.0174
		TMM (mean)	0.184	1.09	0.0530
	4 (pH 7, 0 ppm PPHA)	inverse modeling	0.198*	1.13	0.0166
		TMM (mean)	0.175	1.10	0.0358
CNP	1 (pH 4, 4 ppm PPHA)	inverse modeling	0.198*	1.10	0.0460
		TMM (mean)	0.191	1.04	0.160
	2 (pH 4, 0 ppm PPHA)	inverse modeling	0.192*	1.28	0.0262
		TMM (mean)	0.148	1.30	0.367
	3 (pH 7, 4 ppm PPHA)	inverse modeling	0.201*	1.38	0.0109
		TMM (mean)	0.146	1.37	0.209
	4 (pH 7, 0 ppm PPHA)	inverse modeling	0.198*	1.68	0.0217
		TMM (mean)	0.128	1.56	0.419

*calculated v_w

Table 3.10: Summary of chemical nonequilibrium CNP transport parameters modeled with CXTFIT 2.1 for E1-E4

Experiment (conditions)	Parameter	
	β	ω
1 (pH 4, 4 ppm PPHA)	0.910	0.145
2 (pH 4, 0 ppm PPHA)	0.782	0.350
3 (pH 7, 4 ppm PPHA)	0.770	0.487
4 (pH 7, 0 ppm PPHA)	0.677	0.328

neutral solutions (i.e. E3 and E4) and experiments without DOM (i.e. E2 and E4) (Table 3.09). As summarized in Table 3.10, modeled estimates of chemical nonequilibrium transport parameters indicate CNP β is greater in experiments with DOM (i.e. E1 and E3) and acidic solutions (i.e. E1 and E2). However, the relationship between CNP ω and experimental conditions is unclear. In experiments with acidic solutions (i.e. E1 and E2), CNP ω decreases in the presence of DOM. The opposite is true in experiments with neutral solutions (i.e. E3 and E4) (Table 3.10).

Modeled estimates of Br and CNP *D* are similar for all experiments (Table 3.09). Additionally, Br *D* estimates produced by inverse modeling and TMM analyses are similar for each experiment. However, TMM-derived estimates of CNP *D* exceed modeled estimates by more than an order of magnitude for three of four experiments (i.e. E2, E3, and E4). While this study's inverse modeling and TMM analyses are proven methods for characterizing conservative solute (e.g. Br) transport, these large discrepancies in tracer *D* estimates suggest at least one of these methods is incapable of accurately estimating CNP *D*. Overall, the apparent differences in BTCs and parameter estimates suggest CNP transport is influenced by DOM.

CHAPTER 4: DISCUSSION

This study primarily aims to assess the influence of dissolved organic matter (DOM) on carbon nanoparticle (CNP) transport and how CNP transport compares to that of bromide (Br), a conservative solute tracer. Such assessments are based on qualitative and quantitative comparisons of CNP and Br breakthrough curve (BTC) data and analyses. As shown in Figures 3.05 and 3.06, Br and CNPs were transported similarly in all experiments. While all Br BTCs are nearly identical, DOM-related distinctions are evident among CNP BTCs. Notably, CNP BTCs are vertically offset as effluent concentrations (C) approach influent concentrations (C_0) (i.e. $C/C_0 \approx 1$). Furthermore, CNP BTC elution tailing signatures vary. Generally, the rising and falling limbs of CNP BTCs are sharpest in Experiment 1 (E1) (pH 4, 4 parts per million (ppm) Pahokee Peat humic acid (PPHA)) and most rounded in Experiment 4 (E4) (pH 7, 0 ppm PPHA). Such BTC comparisons enable qualitative interpretations of CNP and Br retardation factors (R), which represent the degree to which tracer transport is impeded relative to average pore water velocity (v_w). Nonetheless, analyzing tracer BTC data with temporal moment methods (TMMs) and inverse modeling via the CXTFIT 2.1 code enables more-robust interpretations of how DOM influences CNP transport and how CNP and Br transport compare in the presence of DOM.

By analyzing BTC data with TMMs, the percentage of a tracer's injected mass that was recovered during column experiments (%MR) can be estimated. Nearly 100% of injected CNP and Br mass was recovered in all experiments. Nonetheless, in the absence of DOM, CNPs exhibited the study's two lowest mass recovery rates: 97.6% in E4 and 98.5% in Experiment 2 (E2). The following transport parameters are also estimated by TMMs: tracer velocity (v), dispersion coefficient (D), and R. In addition to these transport parameters, CXTFIT 2.1 is capable of estimating tracer

partitioning (β) and mass transfer (ω) coefficients, which describe nonequilibrium adsorption processes affecting reactive tracers (Toride et al., 1995). As summarized in Table 3.09, R estimates for Br and CNPs are similar, but CNPs are consistently more retarded than Br (R_{CNP}=1.04 to 1.68; R_{Br}=0.857 to 1.13). Estimates of CNP D derived from these methods are more variable and indicate TMMs and (or) CXTFIT 2.1 might be limited in their abilities to accurately characterize CNP dispersion. Ultimately, the observed differences in BTCs and parameter estimates suggest CNP transport depends on the presence of DOM.

Confirming the Suitability of Modeling CNP Transport with CXTFIT 2.1

While qualitatively comparing BTCs only necessitates the proper execution of column experiments, meaningful quantitative comparisons of tracer transport are predicated on a reliable parameter estimation method. Therefore, this study must also determine if the popular solute transport modeling code, CXTFIT 2.1, can be used to effectively model CNP BTCs and estimate transport parameters.

As evidenced by robust goodness-of-fit indicators and a reasonable agreement between modeled and TMM-derived R estimates, this study demonstrates that CNP transport can be effectively modeled with CXTFIT 2.1. Fitted CNP and Br BTCs produced by this inverse modeling method accurately represent observed data (Figures 3.05 and 3.06). Furthermore, r^2 and MSE values for modeled CNP BTCs range from 0.985 to 0.996 and 0.000722 to 0.00359, respectively (Figure 3.06). Modeled Br BTCs also match observed data well, but their slightly lower r^2 values and slightly higher MSE values indicate observed CNP BTCs are better represented by modeled data (Figure 3.05). Additionally, modeled estimates of CNP R are within 8% of those estimated by TMM analyses (Table 3.09). Considering TMM analyses involve direct integration of BTC data

and are not governed by a transport equation, this agreement indicates that modeled CNP R estimates are appropriate for this study's physical systems.

While inversely modeled estimates of CNP and Br D and TMM-derived estimates of Br D are similar for all experiments, TMM-derived estimates of CNP D are uniquely and significantly overestimated (Table 3.09). The TMM-derived estimates of CNP D are likely unreasonably high due to TMMs' neglect of chemical nonequilibrium transport mechanisms. However, as represented by β and ω, such transport processes are accounted for by CXTFIT 2.1 [E2.30]. According to TMMs [E2.18, E2.23], D is only a function of tracer velocity (v), column length (L), the degree of tracer spreading (i.e. tracer arrival time variance, μ_2), and tracer injection time (t_{inj}). While a conservative tracer's degree of spreading is governed exclusively by mechanical dispersion and diffusion, reversible adsorption retards transport and increases spreading of reactive solutes and particles. As indicated by this study's inverse modeling based on the chemical nonequilibrium ADE [E2.28, E2.30], CNP transport is retarded by reversible equilibrium and nonequilibrium adsorption which effectively promotes CNP spreading. Therefore, since TMM analyses, unlike CXTFIT 2.1 modeling, are incapable of distinguishing adsorption- and dispersion-related spreading, TMM-derived estimates of CNP D are considered unrealistically high.

Considering the one-dimensional column design, flow rate, and homogeneous coarse-grained sediment used in each experiment, D primarily depends on a column's longitudinal dispersivity (α_L) and average tracer velocity (v) [E2.19]. Since CNPs were transported alongside Br in the same porous media, differences in tracer D for any single experiment are mostly attributed to differences in v. Therefore, since tracer R estimates are similar in all experiments (Table 3.09), reasonable estimates of tracer D should also be similar in all experiments. Table 3.09 shows that inversely modeled estimates of CNP D are expectedly similar to inversely modeled and TMM-derived

estimates of Br D. Such similarities and the ability of CXTFIT 2.1 to specifically account for chemical nonequilibrium transport suggest this inverse modeling method is capable of producing reasonable estimates of CNP D. Nonetheless, slight differences in inversely modeled estimates of tracer D might reveal a limitation of modeling CNP transport with CXTFIT 2.1 under these experimental conditions. Considering CXTFIT 2.1 assumes that all adsorption processes are linear, differences between modeled Br and CNP D estimates could be explained by nonlinear CNP adsorption to matrix grains (Toride et al., 1995).

Assessing the Influence of DOM on CNP Transport

Since CNP transport can be effectively modeled with CXTFIT 2.1, fitted BTCs and estimates of v, R, D, β, and ω can be used to elucidate CNP transport in saturated porous media. To evaluate how CNP transport is influenced by DOM, BTCs and transport parameter estimates from experiments incorporating DOM (i.e. E1 and Experiment 3 (E3)) are compared to those from DOM-free experiments (i.e. E2 and E4). To isolate DOM as the only independent variable, experiments of equal pH are compared.

Experiments 1 and 2 (pH 4)

As demonstrated in Figure 4.01, E2 CNP BTCs are slightly translated in the positive x-direction relative to E1 BTCs. This shift is explained by 14% less CNP retardation in the presence of DOM (Table 4.01). As CNPs approach maximum concentration, E2 BTCs separate from E1 BTCs. Furthermore, E2 BTCs exhibit slightly more-pronounced elution tailing. This spreading is quantified by comparing CNP emergence and elution durations (Table 4.02). In this context, emergence refers to the duration (in PV) over which tracer concentration increases from a tracer's initial arrival to C/C_0=1, and elution refers to the duration over which tracer concentration

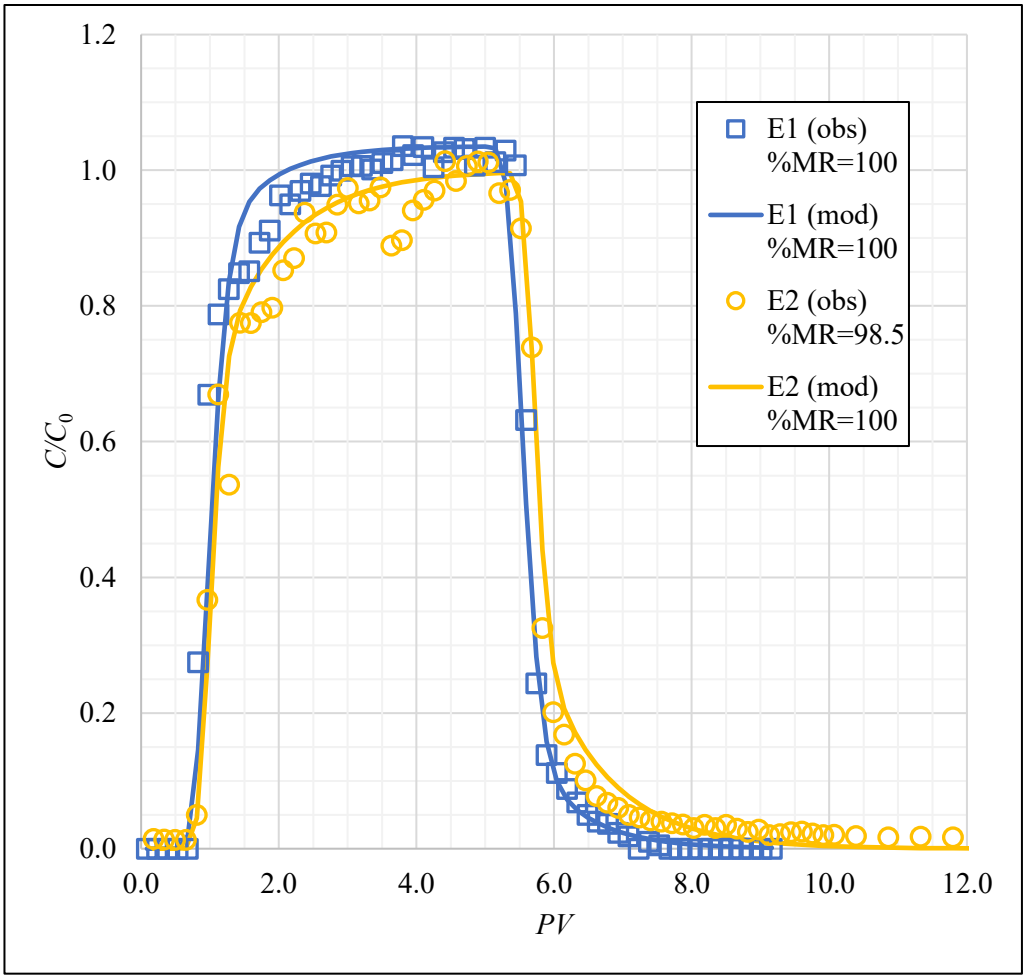

Figure 4.01: Observed ("obs", hollow shapes) and modeled ("mod", solid lines) CNP BTCs for E1 (blue; pH 4, 4 ppm PPHA) and E2 (yellow; pH 4, 0 ppm PPHA). The %MR values calculated from each BTC are included in the legend.

decreases from a BTC peak to C/C_0=0. Relative to E2 (absent DOM), CNP emergence and elution periods are 1.5 PVs and 3.8 PVs shorter, respectively, in the presence of DOM (Table 4.02). Such distinctions correspond to CNP transport being less retarded in E1. Additionally, the CNP partitioning coefficient, β, is 16% greater in the presence of DOM (Table 4.01). Considering this partitioning coefficient is directly proportional to the fraction of equilibrium adsorption sites (f) (Table 2.05), E1 and E2 CNP β estimates indicate that a greater fraction of equilibrium adsorption sites exists in the presence of DOM.

Table 4.01: Comparing CXTFIT 2.1 tracer transport parameter estimates* for experiments with and without DOM

Tracer	Compared experiments (pH)	%Difference** (relative to estimate for experiment without DOM)			
		R	***D***	***β***	***ω***
Br	E1 & E2 (pH 4)	-11	36		
	E3 & E4 (pH 7)	-4	4		
CNP	E1 & E2 (pH 4)	-14	71	16	-59
	E3 & E4 (pH 7)	-18	51	14	48

*Table 3.09

**$\%Difference = \frac{(estimate\ for\ experiment\ \mathbf{with}\ DOM) - (estimate\ for\ experiment\ \mathbf{without}\ DOM)}{(estimate\ for\ experiment\ \mathbf{without}\ DOM)} \times 100$

Table 4.02: Summary of observed tracer emergence and elution durations for E1-E4

Tracer	Experiment (conditions)	Approximate duration of event (PV)	
		Emergence	Elution
Br	1 (pH 4, 4 ppm PPHA)	0.42	1.5
	2 (pH 4, 0 ppm PPHA)	0.59	1.5
	3 (pH 7, 4 ppm PPHA)	0.91	1.5
	4 (pH 7, 0 ppm PPHA)	1.1	1.2
CNP	1 (pH 4, 4 ppm PPHA)	2.1	1.6
	2 (pH 4, 0 ppm PPHA)	3.6	5.4
	3 (pH 7, 4 ppm PPHA)	3.1	4.1
	4 (pH 7, 0 ppm PPHA)	4.5	7.9

Generally, reactive tracer spreading can be elucidated by mass transfer coefficient (ω) estimates. For example, considering ω is directly proportional to the first-order kinetic rate coefficient (α), reduced tracer spreading can stem from faster kinetic adsorption (Toride et al., 1995). While less spreading was observed in E1 than E2 (Figure 4.01), CNP ω is 59% less in the presence of DOM

(Table 4.01). However, as indicated by a large 95% confidence interval (Table 3.01), the estimate of CNP ω in E1 is less certain than in all other experiments and could be misleading. Regardless, the retarding effect of the CNP ω estimate in question is likely insignificant considering the relatively small fraction of nonequilibrium adsorption sites in E1, as indicated by a β estimate near unity (Table 3.10). Finally, as indicated by incomplete mass recovery (%MR=98.5), a minor amount of irreversible CNP adsorption was observed in E2 (Figure 4.01).

This study hypothesizes that DOM will enable conservative, unimpaired CNP transport in E1, and CNP transport will be slightly impeded in E2 (Table 1.01). Considering CNP transport was minimally retarded (Table 3.09) and 100% of injected CNP mass was recovered (Figure 3.01), the E1 hypothesis is confirmed. The results of E2 indicate that adsorption processes retained CNPs and retarded CNP transport relative to E1. Therefore, the E2 hypothesis is also confirmed. In solutions at pH 4, CNPs likely have a small positive surface charge and, therefore, will be attracted to negatively charged silica sand grains and (or) other CNPs. Attraction to sediment and other CNPs would lead to CNP adsorption and dispersion destabilization, respectively. These transport-limiting processes would be evidenced by retardation and mass retention. However, humic acid can increase the stability of NP dispersions by imparting negative surface charges on NPs below their points of zero charge (PZC) (Christian et al., 2008; Wagner et al., 2014). While additional research is needed to confirm these physical phenomena occurred in this study, CNP transport is apparently enhanced by the presence of humic acid (4 ppm PPHA) in acidic solutions.

Experiments 3 and 4 (pH 7)

Similar differences between E3 and E4 BTCs suggest DOM also enhances CNP transport in neutral solutions. Although to a lesser degree than observed in E1 and E2 BTCs, CNP BTCs for

E4 lag behind those for E3 (Figure 4.02). This lag corresponds to CNP transport being 18% less retarded in neutral solutions containing DOM than in E4 absent DOM (Table 4.01). Such CNP retardation is clearly demonstrated by the vertical offset of E3 and E4 BTCs during CNP emergence and elution periods (Figure 4.02). This BTC separation indicates CNPs experience less spreading in neutral solutions containing DOM (i.e. E3). Similar to E1 and E2, CNP emergence and elution periods are 1.4 PVs and 3.8 PVs shorter, respectively, in E3 than in E4 (Table 4.02). Considering these differences in CNP emergence and elution are nearly identical to those observed between E1 and E2, the influence of DOM on CNP transport may be independent of solution pH.

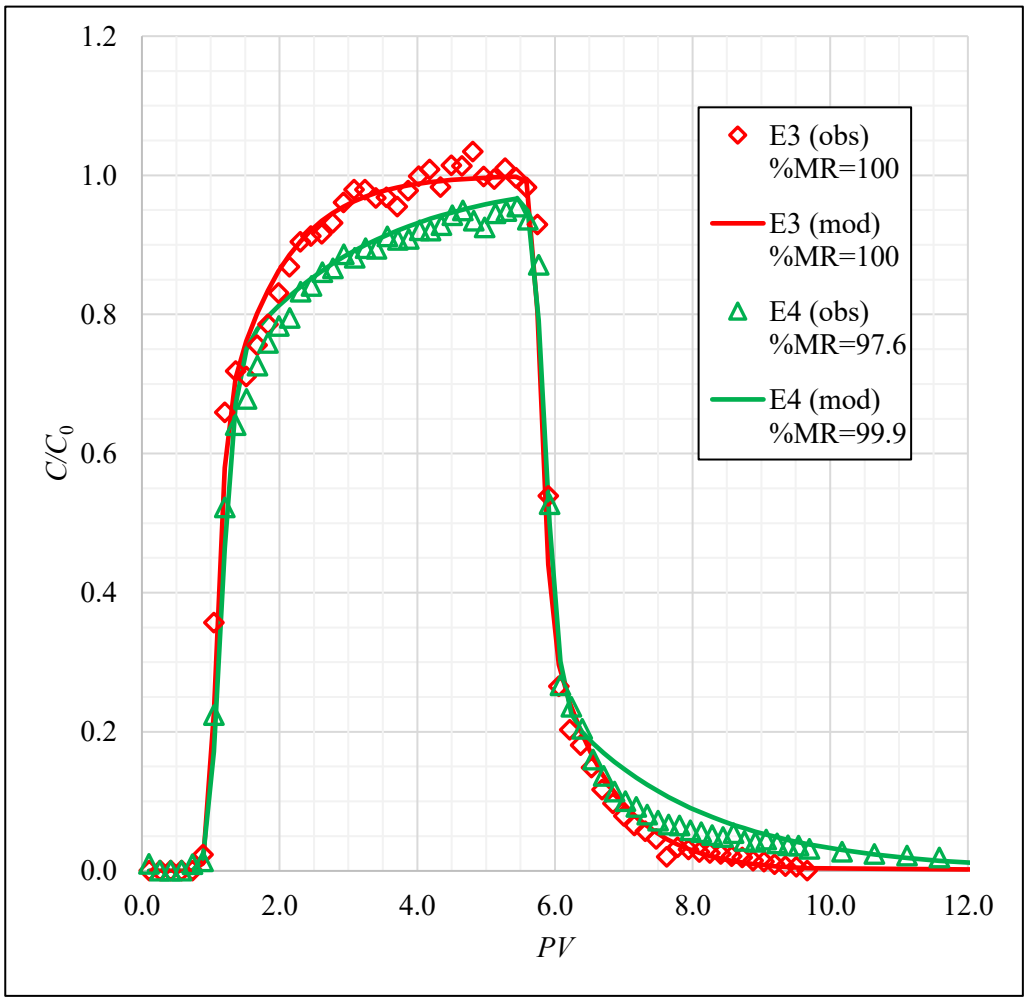

Figure 4.02: Observed ("obs", hollow shapes) and modeled ("mod", solid lines) CNP BTCs for E3 (red; pH 7, 4 ppm PPHA) and E4 (green; pH 7, 0 ppm PPHA). The %MR values calculated from each BTC are included in the legend.

The confirmed accuracy of inversely modeled CNP transport via CXTFIT 2.1 indicates observed CNP retardation and spreading result from equilibrium and nonequilibrium, or kinetic, adsorption. Similar to E1 and E2, CNP β is 14% greater in E3 than in E4 (Table 4.01). Therefore, DOM consistently increases the fraction of equilibrium adsorption sites (f) in acidic and neutral solutions. While CNP ω is unexpectedly less in E1 than in E2, DOM increases the rate of kinetic adsorption in neutral solutions, as indicated by a 48% greater ω estimate for E3. This relationship is supported by less observed CNP spreading in E3 relative to E4. Finally, similar to E2, a small fraction of injected CNP mass was likely retained in E4 absent DOM, but confirming this retention would necessitate additional research. Nonetheless, such retention would stem from irreversible CNP adsorption to matrix grains.

This study hypothesizes that CNP transport will be conservative and unimpaired in E3 and E4 (Table 1.01). Considering CNP transport in E3 was minimally retarded (Table 3.09) and conservative (Figure 4.02), the E3 hypothesis is confirmed. However, since CNP transport was retarded in E4 relative to E3 (Table 4.01) and some CNP mass was retained in E4 (Figure 4.02), the E4 hypothesis is rejected. Considering CNP transport in homogeneous silica sand with near-neutral, DOM-free solutions was unimpaired in King's (2015) column experiments, this rejected hypothesis is intriguing and could relate to interference from acid-washed sand (see "Additional Consideration: Influence of Acid-Washed Sand" below).

Comparing CNP and Br Transport

Chemical inertness is a critical quality of ideal groundwater tracers. To build on previous research that demonstrates CNP transport is conservative and unimpeded in saturated homogeneous porous media (Kanj et al., 2011; Subramanian et al., 2013; Li et al., 2014; King, 2015), this study

compares CNP transport to that of Br in solutions with and without DOM. The minimal retardation and complete mass recovery of Br observed throughout this study confirm that Br transport is unimpeded and conservative under these experimental conditions. (In E1 and E2, R<1 might indicate the presence of preferential flow paths.) Based on comparisons of tracer BTCs (Figures 3.01-3.04), CNP BTCs lag slightly behind Br BTCs in the x-direction. Furthermore, vertical BTC displacement is observed during CNP emergence and elution periods (Figures 3.01-3.04). These BTC differences indicate that CNP spreading is generally greater than that of Br. In fact, for all experiments conducted in this study, CNP emergence and elution periods last, on average, 2.6 ± 0.68 PVs and 3.3 ± 2.4 PVs longer than Br emergence and elution periods (Table 4.02).

These tracer transport differences are supported by comparisons of estimated CNP and Br transport parameters (Table 4.03). For all experiments, CNP transport is more retarded than Br transport. This is likely a result of mostly reversible CNP adsorption to equilibrium and nonequilibrium sites on sand grains. Therefore, under these experimental conditions, CNPs will underestimate average pore water velocity and produce less-reliable estimates of aquifer dispersivity than Br. Nonetheless, these distinctions were not witnessed by King (2015) or Li and others (2014) and could relate to potential interference from acid-washed sand. Furthermore, given the limited range of considered experimental conditions and the general similarity between Br and CNP transport in this study, such tracer transport differences might not be realized in natural, heterogeneous settings. Finally, despite being slightly impeded relative to a known conservative solute tracer, the observed efficiency of CNP transport will be valuable in elucidating the fate and transport of NPs that are more prone to adsorption or other filtering mechanisms.

Table 4.03: Comparing modeled CNP and Br transport parameter estimates* for E1-E4

Experiment	**%Difference (relative to Br estimate)	
	R	***D*** **(cm²/min)**
1	28	170
2	33	110
3	27	-37
4	49	31

*Table 3.09

**$\%Difference = \frac{(CNP\ estimate)-(Br\ estimate)}{(Br\ estimate)} \times 100$

Additional Consideration: Influence of Acid-Washed Sand

A key distinction between the methods of King (2015) and this study is the use of acid-washed sand. The cation-exchange capacity of the acid-washed sand (CEC_{aws}) used in this study is approximately one order of magnitude less than that of the water-rinsed sand used by King (2015) (CEC_s) (CEC_{aws}=0.4 milliequivalent per 100 grams; CEC_s=3.9 milliequivalent per 100 grams). The less-negative surface charge of acid-washed sand resulting from the dissolution of bound metal oxides likely reduces the repulsion of negatively charged CNPs. Furthermore, previously collected images from a scanning electron microscope revealed that this dissolution creates cavities in sand surfaces (Li et al., 2017). These cavities, as well as decreased sand surface charges, could retard CNP transport by promoting CNP adsorption and (or) filtration. While additional research is needed to confirm such physical phenomena occur in this study, modeled and observed CNP transport is significantly different in acid-washed and water-rinsed sands, yet Br transport appears unaffected (Figure 4.03).

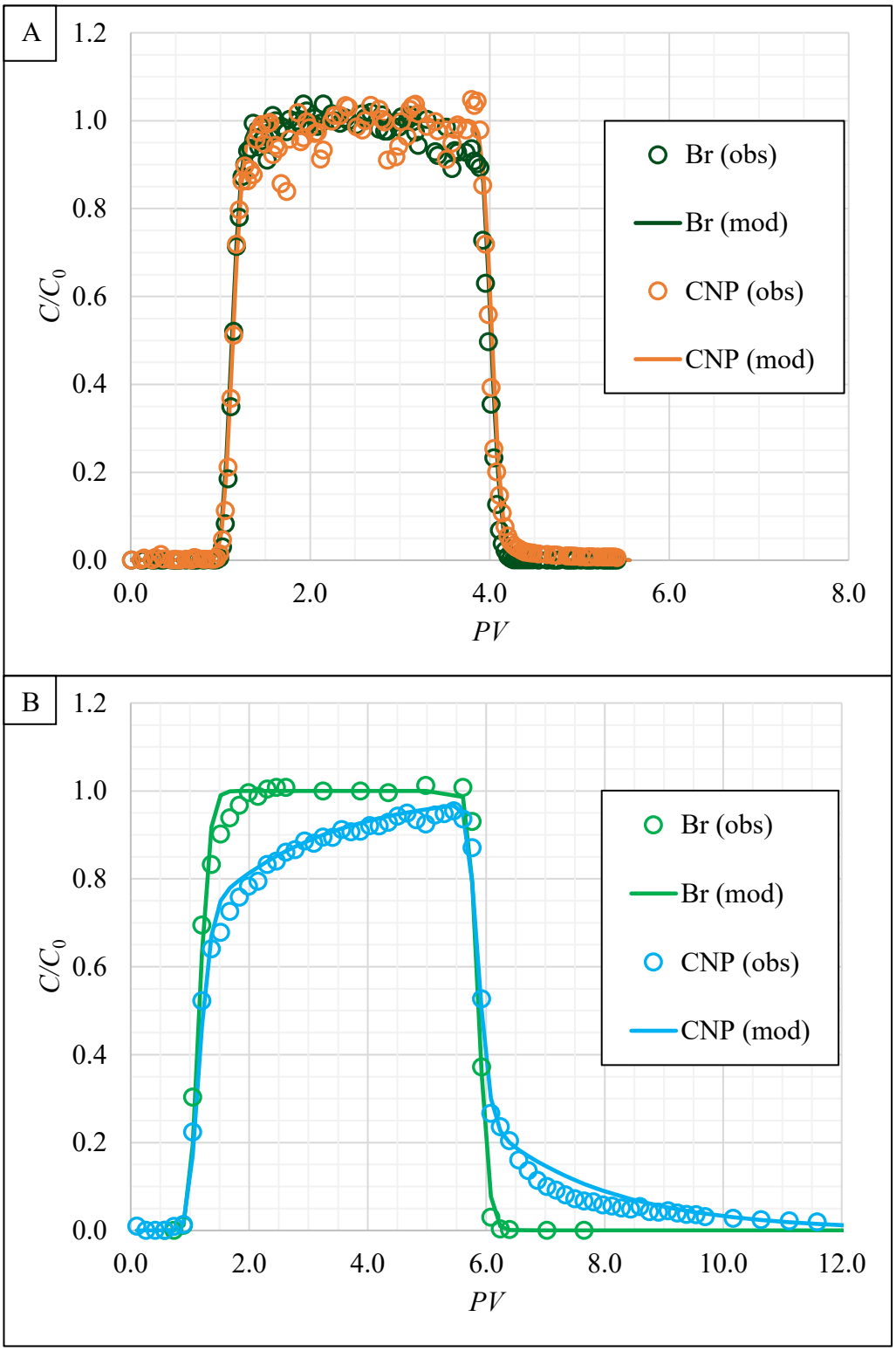

Figure 4.03: Comparing tracer BTCs for experiments using (A) sand rinsed with deionized water (King, 2015) and (B) acid-washed sand (E4). Both experiments were conducted in homogeneous silica sand without DOM and solutions at neutral pH.

CHAPTER 5: CONCLUSIONS AND RECOMMENDATIONS

Conclusions

The ubiquity of natural nanoparticles (NPs) and significant rate at which anthropogenic NPs are being engineered and released to the environment demands a thorough understanding of fate and transport processes. Whether they are released to atmospheric, terrestrial, or aquatic environments, NPs are subject to various transport mechanisms that can ultimately introduce them to groundwater systems. Due to their ability to facilitate contaminant transport and bioavailability, some NPs pose threats to groundwater supplies and dependent ecosystems (Hochella Jr., 2002; Hochella Jr. et al., 2008; Klaine et al., 2008; Hartland et al., 2013). Their unique size-dependent physicochemical properties often confound expectations of how a given type of NP will transport in aquatic environments. Therefore, identifying a NP with the characteristics of an ideal groundwater tracer that can elucidate NP fate and transport is critical.

Recent studies have shown that carbon nanoparticles (CNPs) are groundwater tracer candidates partially due to being inexpensive, nontoxic, readily dispersible in water, detectable over a wide concentration range, and easily sampled and analyzed (Kanj et al., 2011; Subramanian et al., 2013; Li et al., 2014; King, 2015). Owing to their size, stability, and inertness, CNPs are transported conservatively in saturated homogeneous glass beads, calcium carbonate sand, and silica sand. Carbon NP transport is also unimpeded in brine solutions, dual-porosity systems, positively charged sediment, and high pressures and temperatures. In one-dimensional (1D) column tests, CNPs have transported more efficiently than a common dye tracer (i.e. Rhodamine 6G), several types of engineered nanoparticles (ENPs), and a conservative solute tracer (i.e. bromide (Br)) (Kanj et al., 2011; Subramanian et al., 2013; Li et al., 2014; King, 2015). Furthermore, the majority

of injected CNPs were recovered during a field application in an oil-bearing formation (Kanj et al., 2011). While such results indicate CNP transport is conservative under broad environmental conditions, an adequate understanding of CNP transport in natural systems requires evaluating the influence of dissolved organic matter (DOM).

To understand how CNP transport in saturated homogeneous porous media is influenced by DOM, this study conducted four 1D column experiments. Such experiments were designed to enable comparison of CNP and Br transport, breakthrough curve (BTC) analyses, and transport parameter estimation. Experiments 1 and 2 (E1 and E2, respectively) incorporated acidic solutions with and without DOM, respectively. Additionally, Experiments 3 and 4 (E3 and E4, respectively) incorporated neutral solutions with and without DOM, respectively. For all experiments, Br BTCs are nearly identical with slight separation in the x-direction indicating minor transport retardation differences (Figure 3.05). Relative to Br, CNP BTCs are more distinct regarding their horizontal and vertical offset and elution tailing signatures (Figure 3.06). These BTC features qualitatively suggest the degrees of CNP retardation and dispersion are influenced by DOM.

Tracer transport was analyzed quantitatively by comparing transport parameter estimates produced by temporal moment methods (TMMs) and inverse modeling using CXTFIT 2.1, a code developed to solve the advection-dispersion equation (ADE) for solute transport. Mass recovery estimates from TMM analyses indicate Br and CNPs transported conservatively in all experiments. For each experiment, estimated CNP and Br velocities were slightly different than the measured average pore water velocity. This corresponds to estimated retardation factors that are consistently near unity. While TMM-derived estimates of CNP dispersion coefficients are considered inaccurate, modeled estimates are considered reasonable and indicate CNP dispersion was similar to Br in each experiment. Successfully modeling CNP transport with the chemical nonequilibrium ADE

[E2.30] indicates CNPs are subject to equilibrium and nonequilibrium, or kinetic, adsorption under all experimental conditions. However, equilibrium adsorption is more prevalent in the presence of DOM and acidic solutions. In neutral solutions (i.e. E3 and E4), kinetic adsorption occurred at a substantially higher rate in the presence of DOM (i.e. E3).

Generally, CNP transport is conservative and minimally impeded regardless of DOM. As hypothesized, CNP transport was unimpaired and conservative in acidic and neutral solutions containing DOM (i.e. E1 and E3, respectively) and slightly retarded in acidic solutions without DOM (i.e. E2). Contrary to the E4 hypothesis, CNPs were slightly retarded and retained by sand in neutral solutions without DOM. Independent of solution pH, CNP transport was enhanced by DOM. Considering the natural prevalence of DOM, these findings increase confidence that CNPs will transport conservatively in natural aquatic systems.

This study also concludes that CNP transport can be characterized with the proven solute transport modeling code CXTFIT 2.1. Using this inverse modeling method, representative BTCs were fit to observed CNP and Br concentration data, and transport parameters were accurately estimated. The ability to model CNPs as pseudo-solutes with CXTFIT 2.1 presents a convenient and accurate method for characterizing and comparing the transport of CNPs, and possibly other less-understood nanoscale objects, to that of conservative solute tracers. Furthermore, especially when considering the diameters of CNPs and Br are within an order of magnitude, successfully modeling CNPs with CXTFIT 2.1 blurs the distinction between NPs and solutes.

According to transport parameter estimates, CNP transport was slightly impeded relative to Br in all column experiments. Under this study's experimental conditions and compared to Br, a groundwater tracer test using CNPs would slightly underestimate average pore water velocity and

overestimate aquifer dispersivity. However, as suggested by the unexpected retardation of CNPs in E4 and similar differences between CNP and Br transport in all experiments of this study, the acid-washed sand might have inadvertently influenced CNP transport. Regardless of their ability to characterize aquifers and groundwater flow, CNPs can advance the understanding of how reactive or otherwise less-mobile nanoscale objects are transported in saturated systems. Considering no simulated natural hydrogeologic conditions, including the presence of DOM, have significantly retarded CNP transport, CNPs are tentatively regarded as a reference NP, or ideal NP tracer.

Recommendations

Determining whether CNPs represent an ideal groundwater or NP tracer will require additional research. Excluding the lone field trial (Kanj et al., 2011), CNP transport research has been restricted to simple 1D column experiments that have investigated a limited number of environmental conditions and lacked natural heterogeneity. Advancing the understanding of CNP transport will require thorough material property analyses and a diverse suite of increasingly complex laboratory transport experiments. However, fully understanding the suitability of using CNPs as applied tracers will necessitate transport studies in heterogeneous field-scale settings. To guide future research and progress the scientific comprehension of CNP transport in groundwater systems, this study provides the following recommendations.

General Recommendations for Future Studies

- This study should be expanded to incorporate other types of DOM (i.e. fulvic acid).
- Additional 1D column experiments should further investigate the influence of solution pH and temperature (i.e. low temperatures); various monovalent and divalent ions; dissolved

metals, clays and other fine-grained sediments; CNP concentration; and flow rate on CNP transport.

- While other studies have independently considered the influence of solution ionic strength and compared CNP transport to that of other ENPs (Kanj et al., 2011; Subramanian et al., 2013; Li et al., 2014), ionic strength was held constant in this study, and CNPs were only studied alongside Br. Therefore, the influence of ionic strength and other ENPs should be studied in the presence of DOM.
- Once the influence of additional individual environmental conditions is understood, column experiments should be conducted with natural sediment (or fractured rock cores) and groundwater samples. Such samples should be physically and chemically characterized prior to use.
- The point of zero charge (PZC) of CNPs should be determined prior to additional pH experiments.
- In addition to 1D column experiments, CNP transport should be studied in two- and three-dimensional systems.
- Ultimately, CNPs should be employed in field-scale studies to adequately understand their ability to transport conservatively in natural saturated heterogeneous settings.
- For concurrent use with other fluorescent tracers, an effort should be made to engineer different versions of CNPs with unique fluorescence signatures.

Recommendations for Future Studies Conducted in the Author's Laboratory

- To better simulate 1D flow, columns with greater length-to-radius ratios should be used.

- If the same type of column is used in the future, the influent end should be fitted with a frit to evenly distribute flow.
- Considering the potential interference from and unrealistic nature of acid-washed sand, water-rinsed sand is preferred.
- An improved magnetic stir plate would prevent heat transfer to solutions as they are being prepared and analyzed.
- For the sake of time and accuracy, effluent Br samples should be analyzed via ion chromatography. Analyzing Br samples with an ISE is cumbersome and risks introducing an unnecessary amount of experimental error.
- A programmable syringe pump or inline flow meter would enable more-accurate flow rate measurements.
- The better understand CNP-sediment interactions, sediment zeta potential should be analyzed before each experiment.
- To study DOM adsorption to CNPs, CNP dispersions containing DOM should undergo centrifugation, and the supernatant should be analyzed for DOM concentration. Additionally, CNP zeta potential should be measured in the presence of DOM.
- Additional glassware (i.e. test tube) drying racks are needed.
- A UVA light can be used to visually inspect or photograph the distribution of CNPs during column experiments. To refine the time correction process, this light could be used to track the leading edge of a CNP injection from its reservoir to the column and from the column to the fraction collector.

REFERENCES

Adair, J.H., Suvaci, E., & Sindel, J. (2001). Surface and Colloid Chemistry. In J.K.H. Buschow, R.W. Cahn, M.C. Flemings, B. Ilschner, E.J. Kramer, S. Mahajan, & P. Veyssière (Eds.), *Encyclopedia of Materials: Science and Technology* (pp. 1-10). New York: Elsevier. https://doi.org/10.1016/B0-08-043152-6/01622-3.

Aiken, G.R., Hsu-Kim, H., & Ryan, J.R. (2011). Influence of dissolved organic matter on the environmental fate of metals, nanoparticles, and colloids. *Environmental Science and Technology, 45*(8), pp. 3196-3201. https://doi.org/10.1021/es103992s.

ASTM Standard E2456, 2006 (2012). "Standard Specification for Standard Sand." ASTM International, West Conshohocken, PA, 2006. Retrieved from: http://www.astm.org/cgi-bin/resolver.cgi?E2456.

ASTM Standard C778, 2009. "Standard Terminology Relating to Nanotechnology." ASTM International, West Conshohocken, PA, 2009. Retrieved from: https://www.astm.org/Standards/C778.htm.

Auffan, M., Rose, J., Bottero, J.-Y., Lowry, G.V., Jolivet, J.-P., & Wiesner, M.R. (2009). Towards a definition of inorganic nanoparticles from an environmental, health and safety perspective. *Nature Nanotechnology, 4*, pp. 634-641. https://doi.org/10.1038/nnano.2009.242.

Baalousha, M. & Lead, J.R. (2007). Characterization of natural aquatic colloids (<5 nm) by flow-field flow fractionation and atomic force microscopy. *Environmental Science and Technology, 41*(4), pp. 1111-1117. https://doi.org/10.1021/es061766n.

Baalousha, M., Manciulea, A., Cumberland, S., Kendall, K., & Lead, J. (2008). Aggregation and surface properties of iron oxide nanoparticles: Influence of pH and natural organic matter. *Environmental Toxicology and Chemistry, 27*(9), pp. 1875-1882. https://doi.org/10.1897/07-559.1.

Baumann, T. (2010). Nanoparticles in groundwater – occurrence and applications. In F.H. Frimmel & R. Niessner (Eds.), *Nanoparticles in the Water Cycle – Properties, Analysis and Environmental Relevance* (pp. 23-34). Berlin: Springer-Verlag. https://doi.org/10.1007/978-3-642-10318-6.

Bergmann, C.P., Machado, F.M., & Lima, E.C. (2015). Introduction. In C.P. Bergmann & F.M. Machado (Eds.), *Carbon Nanomaterials as Adsorbents for Environmental and Biological Applications* (pp. 1-9). Switzerland: Springer International Publishing. https://doi.org/10.1007/978-3-319-18875-1.

Bourlinos A.B., Stassinopoulos, A., Anglos, D., Zboril, R., Karakassides, M., & Giannelis, E.P. (2008). Surface functionalized carbogenic quantum dots. *Small, 4*(4), pp. 455-458. https://doi.org/10.1002/smll.200700578.

Boverhof, D.R., Bramante, C.M., Butala, J.H., Clancy, S.F., Lafranconi, M., West, J., & Gordon, S.C. (2015). Comparative assessment of nanomaterial definitions and safety evaluation considerations. *Regulatory Toxicology and Pharmacology, 73*(1), pp. 137-150. https://doi.org/10.1016/j.yrtph.2015.06.001.

British Standards Institution (2011). PAS 71: Nanoparticles – Vocabulary. Retrieved from: https://shop.bsigroup.com/Browse-By-Subject/Nanotechnology/Terminologies-for-nanotechnologies-/PAS-71/.

Chen K.L., Mylon, S.E., & Elimelech, M. (2007). Enhanced aggregation of alginate-coated iron oxide (hematite) nanoparticles in the presence of calcium, strontium, and barium cations. *Langmuir, 23*(11), pp. 5920-5928. https://doi.org/10.1021/la063744k.

Chen, G., Liu, X., & Su, C. (2012). Distinct effects of humic acid on transport and retention of TiO_2 rutile nanoparticles in saturated sand columns. *Environmental Science and Technology, 46*(13), pp. 7142-7150. https://doi.org/10.1021/es204010g.

Chen, K.L. & Elimelech, M. (2008). Interaction of fullerene (C_{60}) nanoparticles with humic acid and alginate coated silica surfaces: measurements, mechanisms, and environmental implications. *Environmental Science and Technology, 42*(20), pp. 7607-7614. https://doi.org/10.1021/es8012062.

Christian, P., von der Kammer, F., Baalousha, M., & Hofmann, T. (2008). Nanoparticles: structure, properties, preparation and behaviour in environmental media. *Ecotoxicology, 17*(5), pp. 326-343. https://doi.org/10.1007/s10646-008-0213-1.

Coelho, M.C., Torrão, G., Emami, N., & Grácio, J. (2012). Nanotechnology in automotive industry: research strategy and trends for the future – small objects, big impacts. *Journal of Nanoscience and Nanotechnology, 12*(8), pp. 6621-6630. https://doi.org/10.1166/jnn.2012.4573.

Cullen, E., O'Carroll, D.M., Yanful, E.K., & Sleep, B. (2010). Simulation of the subsurface mobility of carbon nanoparticles at the field scale. *Advances in Water Resources, 33*(4), pp. 361-371. https://doi.org/10.1016/j.advwatres.2009.12.001.

Davis, S.N. & de Wiest, R.J.M. (1967). *Hydrogeology.* New York: John Wiley and Sons, Incorporated.

Das, B.S. & Kluitenberg, G.J. (1996). Moment analyses to estimate degradation rate constants from leaching experiments. *Soil Science Society of America Journal, 60*(6), pp. 1724-1731. https://doi.org/10.2136/sssaj1996.03615995006000060017x.

de Mello Donegá, C. (2014). The Nanoscience Paradigm: "Size Matters!". In C. de Mello Donegá (Ed.), *Nanoparticles: Workhorses of Nanoscience* (pp. 1-12). Berlin: Springer-Verlag. https://doi.org/10.1007/978-3-662-44823-6_1.

Derjaguin, B. & Landau, L. (1941). Theory of the stability of strongly charged lyophobic sols and of the adhesion of strongly charged particles in solutions of electrolytes. *Acta Physicochimica URSS, 14*, pp 633-662. https://doi.org/10.1016/0079-6816(93)90013-L.

Diallo, M.S., Christie, S., Swaminathan, P., Johnson Jr., J.H., & Goddard III, W.A. (2005). Dendrimer enhanced ultrafiltration. 1. Recovery of Cu(II) from aqueous solutions using PAMAM dendrimers with ethylene diamine core and terminal NH_2 groups. *Environmental Science and Technology, 39*(5), pp. 1366-1377. https://doi.org/10.1021/es048961r.

Divine, C.E., Sanford, W.E., & McCray, J.E. (2003). Helium and neon groundwater tracers to measure residual DNAPL: Laboratory investigation. *Vadose Zone Journal, 2*(3), pp. 382-388. https://doi.org/10.2136/vzj2003.3820.

Elimelech, M. & O'Melia, C.R. (1990). Kinetics of deposition of colloidal particles in porous media. *Environmental Science and Technology, 24*(10), pp. 1528-1536. https://doi.org/10.1021/es00080a012.

Frimmel, F.H. & Delay, M. (2010). Introducing the "nano-world". In F.H. Frimmel & R. Niessner (Eds.), *Nanoparticles in the Water Cycle – Properties, Analysis and Environmental Relevance* (pp. 1-11). Berlin: Springer-Verlag. https://doi.org/10.1007/978-3-642-10318-6.

Fu, F., Han, W., Tang, B., Hu, M., & Cheng, Z. (2013). Insights into environmental remediation of heavy metal and organic pollutants: simultaneous removal of hexavalent chromium and dye from wastewater by zero-valent iron with ligand-enhanced reactivity. *Chemical Engineering Journal, 232*, pp. 534-540. https://doi.org/10.1016/j.cej.2013.08.014.

Ghosh, S., Mashayekhi, H., Pan, B., Bhowmik, P., & Xing, B. (2008). Colloidal behavior of aluminum oxide nanoparticles as affected by pH and natural organic matter. *Langmuir, 24*(21), pp. 12385-12391. https://doi.org/10.1021/la802015f.

Gilbert, B. & Banfield, J. (2005). Molecular-scale processes involving nanoparticulate minerals in biogeochemical systems. *Reviews in Mineralogy and Geochemistry, 59*(1), pp. 109-155. https://doi.org/10.2138/rmg.2005.59.6.

Goltz, M.N. & Roberts, P.V. (1987). Using the method of moments to analyze three-dimensional diffusion-limited solute transport from temporal and spatial perspectives. *Water Resources Research, 23*(8), pp. 1575-1585. https://doi.org/10.1029/WR023i008p01575.

Grasso, D., Subramaniam, K., Butkus, M., Strevett, K., & Bergendahl, J. (2002). A review of non-DLVO interactions in environmental colloidal systems. *Reviews in Environmental Science and Biotechnology, 1*(1), pp. 17-38. https://doi.org/10.1023/A:1015146710500.

Gruère, G.P. (2012). Implications of nanotechnology growth in food and agriculture in OECD countries. *Food Policy, 37*(2), pp. 191-198. https://doi.org/10.1016/j.foodpol.2012.01.001.

Hartland, A., Lead, J.R., Slaveykova, V.I., O'Carroll, D., & Valsami-Jones, E. (2013). The environmental significance of natural nanoparticles. *Nature Education Knowledge, 4*(8), 15

pp. https://www.nature.com/scitable/knowledge/library/the-environmental-significance-of-natural-nanoparticles-105737311.

Hochella Jr., M.F. (2002). There's plenty of room at the bottom: nanoscience in geochemistry. *Geochimica et Cosmochimica Acta, 66*(5), pp. 735-743. https://doi.org/10.1016/S0016-7037(01)00868-7.

Hochella Jr., M.F., Lower, S.K., Maurice, P.A., Penn, R.L., Sahai, N., Sparks, D.L., & Twining, B.S. (2008). Nanominerals, mineral nanoparticles, and earth systems. *Science, 319*(5870), pp. 1631-1635. https://doi.org/10.1126/science.1141134.

Hofmann, T. & von der Kammer, F. (2009). Estimating the relevance of engineered carbonaceous nanoparticle facilitated transport of hydrophobic organic contaminants in porous media. *Environmental Pollution, 157*(4), pp. 1117-1126. https://doi.org/10.1016/j.envpol.2008.10.022.

Hyung, H., Fortner, J.D., Hughes, J.B., & Kim, J.-H. (2007). Natural organic matter stabilizes carbon nanotubes in the aqueous phase. *Environmental Science and Technology, 41*(1), pp. 179-184. https://doi.org/10.1021/es061817g.

International Union of Pure and Applied Chemistry (2014). *Compendium of Chemical Terminology Gold Book, Version, 2.3.3*. A.D. McNaught & A. Wilkinson (Eds.). Oxford: Blackwell Scientific Publications. https://doi.org/10.1351/goldbook.

Jada, A., Akbour, R.A., & Douch, J. (2006). Surface charge and adsorption from water onto quartz sand of humic acid. *Chemosphere, 64*(8), pp. 1287-1295. https://doi.org/10.1016/j.chemosphere.2005.12.063.

Jekel, M.R. (1986). The stabilization of dispersed mineral particles by adsorption of humic substances. *Water Research, 20*(12), pp. 1543-1554. https://doi.org/10.1016/0043-1354(86)90119-3.

Kanj, M.Y., Rashid, H., & Giannelis, E.P. (2011). Industry first field trial of reservoir nanoagents. *Society of Petroleum Engineers International Middle East Oil and Gas Show and Conference*, Manama, Bahrain, 25-28 September, SPE-142592-MS, 10 pp. https://doi.org/10.2118/142592-MS.

Karathanasis, A.D. (2010). Composition and transport behavior of soil nanocolloids in natural porous media. In F.H. Frimmel & R. Niessner (Eds.), *Nanoparticles in the Water Cycle – Properties, Analysis and Environmental Relevance* (pp. 35-54). Berlin: Springer-Verlag. https://doi.org/10.1007/978-3-642-10318-6.

Keller, A.A., Wang, H., Zhou, D., Lenihan, H.S., Cherr, G., Cardinale, B.J., Miller, R., & Ji, Z. (2010). Stability and aggregation of metal oxide nanoparticles in natural aqueous matrices. *Environmental Science and Technology, 44*(6), pp. 1962-1967. https://doi.org/10.1021/es902987d.

Keller, A.A., McFerran, S., Lazareva, A., & Suh, S. (2013). Global life cycle releases of engineered nanomaterials. *Journal of Nanoparticle Research, 15*, 17 pp. https://doi.org/10.1007/s11051-013-1692-4.

Khan, I., Saeed, K., & Khan, I. (2019). Nanoparticles: properties, applications and toxicities. *Arabian Journal of Chemistry, 12*(7), pp. 908-931. https://doi.org/10.1016/j.arabjc.2017.05.011.

King, C.N. (2015). *Fluorescent nanosphere transport: groundwater tracing and implications for nanoparticle migration through groundwater systems* (Unpublished master's thesis). Colorado State University, Fort Collins, CO, 132 pp.

Klaine, S.J., Alvarez, P.J.J., Batley, G.E., Fernandes, T.F., Handy, R.D., Lyon, D.Y., Mahendra, S., McLaughlin, M.J., & Lead, J.R. (2008). Nanomaterials in the environment: behavior, fate, bioavailability, and effects. *Environmental Toxicology and Chemistry, 27*(9), pp. 1825-1851. https://doi.org/10.1897/08-090.1.

Krysmann, M.J., Kelarakis, A., Dallas, P., & Giannelis, E.P. (2012). Formation mechanism of carbogenic nanoparticles with dual photoluminescence emission. *Journal of the American Chemical Society, 134*(2), pp. 747-750. https://doi.org/10.1021/ja204661r.

Kumar, N. & Kumbhat, S. (2016). *Essentials in Nanoscience and Nanotechnology*. New Jersey: John Wiley and Sons, Incorporated. Retrieved from: https://ebookcentral.proquest.com/lib/csu/detail.action?docID=4499667.

Lee., J., Mahendra, S., & Alvarez, P.J.J. (2010). Nanomaterials in the construction industry: a review of their applications and environmental health and safety considerations. *American Chemical Society Nano, 4*(7), pp. 3580-3590. https://doi.org/10.1021/nn100866w.

Li, T., Jin, Y., Huang, Y., Li, B., & Shen, C. (2017). Observed dependence of colloid detachment on the concentration of initially attached colloids and collector surface heterogeneity in porous media. *Environmental Science and Technology, 51*(5), pp. 2811-2820. https://doi.org/10.1021/acs.est.6b06264.

Li, Y.V., Cathles, L.M., & Archer, L.A. (2014). Nanoparticle tracers in calcium carbonate porous media. *Journal of Nanoparticle Research, 16*, pp. 2540-2541. https://doi.org/10.1007/s11051-014-2541-9.

Lin, D. & Xing, B. (2008). Root uptake and phytotoxicity of ZnO nanoparticles. *Environmental Science and Technology, 42*(15), pp. 5580-5585. https://doi.org/10.1021/es800422x.

Logan, B.E. (2012). *Environmental Transport Processes*. New Jersey: John Wiley and Sons, Incorporated. Retrieved from: https://ebookcentral.proquest.com/lib/csu/detail.action?docID=818175.

Maloszewski, P., Benischke, R., Harum, T., & Zojer, H. (1994). Estimation of solute transport parameters in heterogen groundwater system of a karstic aquifer using artificial tracer experiments. *Water Down Under*, Adelaide, Australia, 21-25 November, IAH Congress, pp. 105-111, IAH – Publication NCP 94/14. Retrieved from:

https://graz.pure.elsevier.com/en/publications/estimation-of-solute-transport-parameters-in-the-heterogeneous-gr.

Malvern Instruments Limited (2017). Zeta potential – An introduction in 30 minutes. Malvern Instruments Limited Technical Note. Retrieved from: https://www.malvernpanalytical.com/en/learn/knowledge-center/technical-notes/TN101104ZetaPotentialIntroduction.html.

McKay, L.D., Sanford, W.E., & Strong, J.M. (2000). Field-scale migration of colloidal tracers in a fractured shale saprolite. *Groundwater, 38*(1), pp. 139-147. https://doi.org/10.1111/j.1745-6584.2000.tb00211.x.

National Science and Technology Council (2016). *National Nanotechnology Initiative Strategic Plan* (National Nanotechnology Initiative Publications and Report). Washington, DC: National Science and Technology Council Committee on Technology, Subcommittee on Nanoscale Science, Engineering, and Technology. Retrieved from: https://www.nano.gov/sites/default/files/pub_resource/2016-nni-strategic-plan.pdf.

Niessner, R. (2010). Nanoparticles acting as condensation nuclei – water droplet formation and incorporation. In F.H. Frimmel & R. Niessner (Eds.), *Nanoparticles in the Water Cycle – Properties, Analysis and Environmental Relevance* (pp. 13-21). Berlin: Springer-Verlag. https://doi.org/10.1007/978-3-642-10318-6.

Njuguna, J., Ansari, F., Sachse, S., Zhu, H., & Rodriguez, V.M. (2014). Nanomaterials, nanofillers, and nanocomposites: Types and properties. In J. Njuguna, K. Pielichowski, & H. Zhu (Eds.), *Health and Environmental Safety of Nanomaterials: Polymer Nanocomposites and Other Materials Containing Nanoparticles* (pp. 3-27). Cambridge: Woodhead Publishing Limited. https://doi.org/10.1533/9780857096678.1.3.

Nowack, B. & Bucheli, T.D. (2007). Occurrence, behavior and effects of nanoparticles in the environment. *Environmental Pollution, 150*(1), pp. 5-22. https://doi.org/10.1016/j.envpol.2007.06.006.

Pang, L., Close, M., & Noonan, M. (1998). Rhodamine WT and Bacillus subtilis transport through an alluvial gravel aquifer. *Groundwater, 36*(1), pp. 112-122. https://doi.org/10.1111/j.1745-6584.1998.tb01071.x.

Pang, L., Goltz, M., & Close, M. (2003). Application of the method of temporal moments to interpret solute transport with sorption and degradation. *Journal of Contaminant Hydrology, 60*(1-2), pp. 123-134. https://doi.org/10.1016/S0169-7722(02)00061-X.

Petosa, A.R., Jaisi, D.P., Quevedo, I.R., Elimelech, M., & Tufenkji, N. (2010). Aggregation and deposition of engineered nanomaterials in aquatic environments: Role of physicochemical interactions. *Environmental Science and Technology, 44*(17), pp. 6532-6549. https://doi.org/10.1021/es100598h.

Pitoniak, E., Wu, C.-Y., Mazyck, D.W., Powers, K.W., & Sigmund, W. (2005). Adsorption enhancement mechanisms of silica-titania nanocomposites for elemental mercury vapor

removal. *Environmental Science and Technology, 39*(5), pp. 1269-1274. https://doi.org/10.1021/es049202b.

Prathna, T.C., Sharma, S.K., & Kennedy, M. (2018). Nanoparticles in household level water treatment: An overview. *Separation and Purification Technology, 199*, pp. 260-270. https://doi.org/10.1016/j.seppur.2018.01.061.

Raliya, R., Saharan, V., Dimkpa, C., & Biswas, P. (2018). Nanofertilizer for precision and sustainable agriculture: Current state and future perspectives. *Journal of Agricultural and Food Chemistry, 66*(26), pp. 6487-6503. https://doi.org/10.1021/acs.jafc.7b02178.

Roduner, E. (2006). Size matters: Why nanomaterials are different. *Chemical Society Reviews, 35*(7), pp. 583-592. https://doi.org/10.1039/b502142c.

Sánchez, A., Recillas, S., Font, X., Casals, E., González, E., & Puntes, V. (2011). Ecotoxicity of, and remediation with, engineered inorganic nanoparticles in the environment. *Trends in Analytical Chemistry, 30*(3), pp. 507-516. https://doi.org/10.1016/j.trac.2010.11.011.

Sanford, W.E., Shropshire, R.G., & Solomon, D.K. (1996). Dissolved gas tracers in groundwater: Simplified injection, sampling, and analysis. *Water Resources Research, 32*(6), pp. 1635-1642. https://doi.org/10.1029/96WR00599.

Schwegmann, H. & Frimmel, F.H. (2010). Nanoparticles: Interaction with microorganisms, In F.H. Frimmel & R. Niessner (Eds.), *Nanoparticles in the Water Cycle – Properties, Analysis and Environmental Relevance* (pp. 165-182). Berlin: Springer-Verlag. https://doi.org/10.1007/978-3-642-10318-6.

Skubal, L.R., Meshkov, N.K., Rajh, T., & Thurnauer, M. (2002). Cadmium removal from water using thiolactic acid-modified titanium dioxide nanoparticles. *Journal of Photochemistry and Photobiology A: Chemistry, 148*(1-3), pp. 393-397. https://doi.org/10.1016/S1010-6030(02)00069-2.

Subramanian, S.K., Li, Y., & Cathles, L.M. (2013). Assessing preferential flow by simultaneously injecting nanoparticle and chemical tracers. *Water Resources Research, 49*(1), pp. 29-42. https://doi.org/10.1029/2012WR012148.

Toride, N., Leij, F.J., & van Genuchten, M.T. (1995). *The CXTFIT Code for Estimating Transport Parameters from Laboratory or Field Tracer Experiments: Version 2.0* (Research Report No. 137). Riverside, California: US Department of Agriculture, Agricultural Research Service, US Salinity Laboratories. Retrieved from: https://www.ars.usda.gov/arsuserfiles/20360500/pdf_pubs/P1444.pdf.

Trujillo-Reyes, J., Peralta-Videa, J.R., & Gardea-Torresdey, J.L. (2014). Supported and unsupported nanomaterials for water and soil remediation: Are they a useful solution for worldwide pollution? *Journal of Hazardous Materials, 280*, pp., 487-503. https://doi.org/10.1016/j.jhazmat.2014.08.029.

Tufenkji, N. & Elimelech, M. (2004). Correlation equation for predicting single-collector efficiency in physicochemical filtration in saturated porous media. *Environmental Science and Technology, 38*(2), pp. 529-536. https://doi.org/10.1021/es034049r.

US Environmental Protection Agency (2007). *Nanotechnology White Paper* (EPA 100/B-07/001). Washington DC: Science Policy Council, Office of the Science Advisor. https://cfpub.epa.gov/si/si_public_record_report.cfm?Lab=OSA&dirEntryID=146066.

US Silica Company (1997). ASTM 20/30 Unground Silica (US Silica Product Data). Retrieved from: https://www.ussilica.com/.

van Genuchten, M.T. & Alves, W.J. (1982). *Analytical Solutions of the One-Dimensional Convective-Dispersive Solute Transport Equation* (Technical Bulletin No. 1661). Washington DC: US Department of Agriculture, Agricultural Research Service. Retrieved from: https://naldc.nal.usda.gov/download/CAT82780278/PDF.

van Genuchten, M.T. & Wagenet, R.J. (1989). Two-site/two-region models for pesticide transport and degradation: Theoretical development and analytical solutions. *Soil Science Society of America Journal, 53*(5), pp. 1303-1310. Retrieved from: https://www.ars.usda.gov/arsuserfiles/20360500/pdf_pubs/P1060.pdf.

Verwey, E.J.W. & Overbeek, J.T.G. (1948). *Theory of the Stability of Lyophobic Colloids: The Interaction of Sol Particles Having an Electric Double Layer*. Amsterdam: Elsevier Publishing Company.

Wagner, S., Gondikas, A., Neubauer, E., Hofmann, T., & von der Kammer, F. (2014). Spot the difference: Engineered and natural nanoparticles in the environment – release, behavior, and fate. *Angewandte Chemie, International Edition, 53*(46), pp. 12398-12419. https://doi.org/10.1002/anie.201405050.

Wolff, H.-J., Radeke, K.-H., & Gelbin, D. (1979). Use of weighted moments to determine axial dispersion coefficients. *Chemical Engineering Science, 34*(1), pp. 101-107. https://doi.org/10.1016/0009-2509(79)85181-7.

Wong, M.S. (2013). CdSe Quantum Dots [image/jpeg]. Retrieved from https://commons.wikimedia.org/wiki/File:CdSe_Quantum_Dots.jpg#metadata.

Wilson, B., Dewers, T., Reches, Z., & Brune, J. (2005). Particle size and energetics of gouge from earthquake rupture zones. *Nature, 434*, pp. 749-752. https://doi.org/10.1038/nature03433.

Yang, L. & Watts, D.J. (2005). Particle surface characteristics may play an important role in phytotoxicity of alumina nanoparticles. *Toxicology Letters, 158*(2), pp. 122-132. https://doi.org/10.1016/j.toxlet.2005.03.003.

Yao, K.-M., Habibian, M.T., & O'Melia, C.R. (1971). Water and waste water filtration: concepts and applications. *Environmental Science and Technology, 5*(11), pp. 1105-1112. https://doi.org/10.1021/es60058a005.

Yu, C., Warrick, A.W., & Conklin, M.H. (1999). A moment method for analyzing breakthrough curves of step inputs. *Water Resources Research, 35*(11), pp. 3567-3575. https://doi.org/10.1029/1999WR900225.

Zhang, W.-x. (2003). Nanoscale iron particles for environmental remediation: An overview. *Journal of Nanoparticle Research, 5*(3-4), pp. 323-332. https://doi.org/10.1023/A:1025520116015.

APPENDIX A: RAW COLUMN EXPERIMENT DATA

E1			
Br			
Time (min)	**Time (PV)**	**Observed C/C_0**	**CXTFIT Modeled C/C_0**
0.00	0.00	0.00	0.00
23.12	0.38	0.00	0.00
32.12	0.53	0.00	0.00
41.12	0.68	0.03	0.02
50.12	0.83	0.46	0.33
59.12	0.98	0.91	0.83
68.12	1.13	1.00	0.98
77.12	1.28	1.06	1.00
86.12	1.42	1.07	1.00
95.12	1.57	1.04	1.00
104.12	1.72	1.01	1.00
113.12	1.87	1.03	1.00
149.12	2.47	1.02	1.00
185.12	3.06	1.03	1.00
221.12	3.66	1.03	1.00
257.12	4.25	1.01	1.00
293.12	4.85	1.01	1.00
320.12	5.29	1.02	1.00
329.12	5.44	0.99	0.94
338.12	5.59	0.63	0.48
347.12	5.74	0.11	0.09
356.12	5.89	0.02	0.01
365.12	6.04	0.01	0.00
374.12	6.19	0.00	0.00
383.12	6.34	0.00	0.00
419.12	6.93	0.00	0.00
455.12	7.53	0.00	0.00
491.12	8.12	0.00	0.00
845.61	13.99	0.00	0.00
CNP			
Time (min)	**Time (PV)**	**Observed C/C_0**	**CXTFIT Modeled C/C_0**
0.00	0.00	0.00	0.00
5.12	0.08	0.00	0.00
14.12	0.23	0.00	0.00
23.12	0.38	0.00	0.00

32.12	0.53	0.00	0.00
41.12	0.68	0.00	0.02
50.12	0.83	0.27	0.15
59.12	0.98	0.67	0.41
68.12	1.13	0.79	0.67
77.12	1.28	0.82	0.84
86.12	1.42	0.85	0.92
95.12	1.57	0.85	0.95
104.12	1.72	0.89	0.97
113.12	1.87	0.91	0.99
122.12	2.02	0.96	0.99
131.12	2.17	0.95	1.00
140.12	2.32	0.97	1.01
149.12	2.47	0.98	1.01
158.12	2.62	0.98	1.02
167.12	2.76	0.99	1.02
176.12	2.91	1.00	1.02
185.12	3.06	1.01	1.03
194.12	3.21	1.01	1.03
203.12	3.36	1.00	1.03
212.12	3.51	1.01	1.03
221.12	3.66	1.01	1.03
230.12	3.81	1.04	1.03
239.12	3.95	1.02	1.03
248.12	4.10	1.03	1.03
257.12	4.25	1.00	1.03
266.12	4.40	1.03	1.03
275.12	4.55	1.03	1.03
284.12	4.70	1.03	1.03
293.12	4.85	1.01	1.03
302.12	5.00	1.03	1.03
311.12	5.15	1.01	1.03
320.12	5.29	1.03	0.98
329.12	5.44	1.01	0.79
338.12	5.59	0.63	0.51
347.12	5.74	0.24	0.28
356.12	5.89	0.14	0.16
365.12	6.04	0.11	0.10
374.12	6.19	0.09	0.07
383.12	6.34	0.07	0.06
392.12	6.49	0.05	0.05
401.12	6.63	0.04	0.04
410.12	6.78	0.04	0.03
419.12	6.93	0.02	0.03

428.12	7.08	0.02	0.02
437.12	7.23	0.00	0.02
446.12	7.38	0.01	0.01
455.12	7.53	0.01	0.01
464.12	7.68	0.00	0.01
473.12	7.83	0.00	0.01
482.12	7.97	0.00	0.01
491.12	8.12	0.00	0.01
500.12	8.27	0.00	0.00
509.12	8.42	0.00	0.00
518.12	8.57	0.00	0.00
527.12	8.72	0.00	0.00
536.12	8.87	0.00	0.00
545.12	9.02	0.00	0.00
554.12	9.16	0.00	0.00
845.61	13.99	0.00	0.00

E2			
Br			
Time (min)	**Time (PV)**	**Observed C/C_0**	**CXTFIT Modeled C/C_0**
0.00	0.00	0.00	0.00
30.67	0.49	0.00	0.00
40.42	0.65	0.00	0.00
50.17	0.81	0.05	0.02
59.92	0.97	0.59	0.40
69.67	1.12	0.95	0.89
79.42	1.28	0.99	0.99
89.17	1.44	1.00	1.00
98.92	1.59	1.01	1.00
108.67	1.75	1.01	1.00
118.42	1.91	1.01	1.00
157.42	2.54	1.00	1.00
196.42	3.16	1.01	1.00
235.42	3.79	1.02	1.00
274.42	4.42	1.01	1.00
313.42	5.05	1.01	1.00
342.67	5.52	1.01	0.98
352.42	5.68	0.79	0.61
362.17	5.83	0.17	0.11
371.92	5.99	0.03	0.01
381.67	6.15	0.01	0.00
391.42	6.30	0.00	0.00
401.17	6.46	0.00	0.00
410.92	6.62	0.00	0.00
449.92	7.25	0.00	0.00
488.92	7.87	0.00	0.00
922.80	14.86	0.00	0.00
CNP			
Time (min)	**Time (PV)**	**Observed C/C_0**	**CXTFIT Modeled C/C_0**
0.00	0.00	0.00	0.00
11.17	0.18	0.01	0.00
20.92	0.34	0.01	0.00
30.67	0.49	0.01	0.00
40.42	0.65	0.01	0.00
50.17	0.81	0.05	0.05
59.92	0.97	0.37	0.27
69.67	1.12	0.67	0.56
79.42	1.28	0.54	0.73
89.17	1.44	0.78	0.79

98.92	1.59	0.77	0.83
108.67	1.75	0.79	0.85
118.42	1.91	0.80	0.88
128.17	2.06	0.85	0.89
137.92	2.22	0.87	0.91
147.67	2.38	0.94	0.92
157.42	2.54	0.91	0.93
167.17	2.69	0.91	0.94
176.92	2.85	0.95	0.95
186.67	3.01	0.97	0.96
196.42	3.16	0.95	0.97
206.17	3.32	0.96	0.97
215.92	3.48	0.97	0.98
225.67	3.63	0.89	0.98
235.42	3.79	0.90	0.98
245.17	3.95	0.94	0.98
254.92	4.11	0.96	0.99
264.67	4.26	0.97	0.99
274.42	4.42	1.01	0.99
284.17	4.58	0.98	0.99
293.92	4.73	1.01	0.99
303.67	4.89	1.01	0.99
313.42	5.05	1.01	1.00
323.17	5.20	0.97	1.00
332.92	5.36	0.97	1.00
342.67	5.52	0.91	0.95
352.42	5.68	0.74	0.73
362.17	5.83	0.33	0.44
371.92	5.99	0.20	0.27
381.67	6.15	0.17	0.21
391.42	6.30	0.13	0.17
401.17	6.46	0.10	0.15
410.92	6.62	0.08	0.12
420.67	6.77	0.07	0.11
430.42	6.93	0.06	0.09
440.17	7.09	0.05	0.08
449.92	7.25	0.05	0.07
459.67	7.40	0.04	0.06
469.42	7.56	0.04	0.05
479.17	7.72	0.04	0.04
488.92	7.87	0.04	0.03
498.67	8.03	0.03	0.03
508.42	8.19	0.03	0.02
518.17	8.35	0.03	0.02

527.92	8.50	0.04	0.02
537.67	8.66	0.03	0.02
547.42	8.82	0.02	0.01
557.17	8.97	0.03	0.01
566.92	9.13	0.02	0.01
576.67	9.29	0.02	0.01
586.42	9.44	0.02	0.01
596.17	9.60	0.03	0.01
605.92	9.76	0.02	0.00
615.67	9.92	0.02	0.00
625.42	10.07	0.02	0.00
644.92	10.39	0.02	0.00
674.17	10.86	0.02	0.00
703.42	11.33	0.02	0.00
732.67	11.80	0.02	0.00
761.92	12.27	0.02	0.00
791.17	12.74	0.02	0.00
820.42	13.21	0.02	0.00
849.67	13.68	0.02	0.00
878.92	14.15	0.02	0.00
922.80	14.86	0.00	0.00

E3			
Br			
Time (min)	**Time (PV)**	**Observed C/C_0**	**CXTFIT Modeled C/C_0**
0.00	0.00	0.00	0.00
34.24	0.58	0.00	0.00
43.56	0.73	0.00	0.00
52.88	0.89	0.04	0.03
62.20	1.05	0.49	0.29
71.52	1.20	0.87	0.74
80.84	1.36	0.94	0.95
90.16	1.52	0.94	1.00
99.48	1.67	0.97	1.00
108.80	1.83	0.99	1.00
118.12	1.99	1.01	1.00
127.44	2.14	0.99	1.00
136.76	2.30	1.00	1.00
174.04	2.93	1.01	1.00
211.32	3.55	1.01	1.00
248.60	4.18	1.01	1.00
285.88	4.81	0.99	1.00
323.16	5.43	1.00	1.00
332.48	5.59	1.00	0.98
341.80	5.75	0.93	0.74
351.12	5.90	0.43	0.29
360.44	6.06	0.05	0.06
369.76	6.22	0.00	0.01
379.08	6.37	0.00	0.00
388.40	6.53	0.00	0.00
425.68	7.16	0.00	0.00
462.96	7.78	0.00	0.00
877.70	14.76	0.00	0.00
CNP			
Time (min)	**Time (PV)**	**Observed C/C_0**	**CXTFIT Modeled C/C_0**
0.00	0.00	0.00	0.00
6.28	0.11	0.00	0.00
15.60	0.26	0.00	0.00
24.92	0.42	0.00	0.00
34.24	0.58	0.00	0.00
43.56	0.73	0.00	0.00
52.88	0.89	0.02	0.01
62.20	1.05	0.36	0.23
71.52	1.20	0.66	0.58

80.84	1.36	0.72	0.71
90.16	1.52	0.71	0.76
99.48	1.67	0.76	0.80
108.80	1.83	0.79	0.83
118.12	1.99	0.83	0.86
127.44	2.14	0.87	0.89
136.76	2.30	0.90	0.90
146.08	2.46	0.91	0.92
155.40	2.61	0.92	0.93
164.72	2.77	0.93	0.95
174.04	2.93	0.96	0.95
183.36	3.08	0.98	0.96
192.68	3.24	0.98	0.97
202.00	3.40	0.97	0.97
211.32	3.55	0.97	0.98
220.64	3.71	0.95	0.98
229.96	3.87	0.98	0.99
239.28	4.02	1.00	0.99
248.60	4.18	1.01	0.99
257.92	4.34	0.98	0.99
267.24	4.49	1.01	0.99
276.56	4.65	1.01	0.99
285.88	4.81	1.03	1.00
295.20	4.96	1.00	1.00
304.52	5.12	0.99	1.00
313.84	5.28	1.01	1.00
323.16	5.43	1.00	1.00
332.48	5.59	0.98	0.99
341.80	5.75	0.93	0.81
351.12	5.90	0.54	0.44
360.44	6.06	0.27	0.30
369.76	6.22	0.20	0.24
379.08	6.37	0.18	0.20
388.40	6.53	0.15	0.17
397.72	6.69	0.12	0.14
407.04	6.84	0.10	0.12
416.36	7.00	0.08	0.10
425.68	7.16	0.06	0.08
435.00	7.31	0.06	0.07
444.32	7.47	0.05	0.06
453.64	7.63	0.02	0.05
462.96	7.78	0.03	0.04
472.28	7.94	0.03	0.03
481.60	8.10	0.03	0.03

490.92	8.25	0.03	0.02
500.24	8.41	0.02	0.02
509.56	8.57	0.02	0.01
518.88	8.72	0.02	0.01
528.20	8.88	0.01	0.01
537.52	9.04	0.01	0.01
546.84	9.19	0.01	0.01
556.16	9.35	0.01	0.01
565.48	9.51	0.01	0.00
574.80	9.66	0.00	0.00
877.70	14.76	0.00	0.00

E4			
Br			
Time (min)	**Time (PV)**	**Observed C/C_0**	**CXTFIT Modeled C/C_0**
0.00	0.00	0.00	0.00
34.62	0.57	0.00	0.00
44.10	0.73	0.00	0.00
53.58	0.89	0.01	0.01
63.06	1.05	0.30	0.19
72.54	1.20	0.69	0.63
82.02	1.36	0.83	0.92
91.50	1.52	0.90	0.99
100.98	1.68	0.94	1.00
110.46	1.83	0.97	1.00
119.94	1.99	1.00	1.00
129.42	2.15	0.99	1.00
138.90	2.30	1.00	1.00
148.38	2.46	1.01	1.00
157.86	2.62	1.01	1.00
195.78	3.25	1.00	1.00
233.70	3.88	1.00	1.00
262.14	4.35	1.00	1.00
300.06	4.98	1.01	1.00
337.98	5.61	1.01	0.99
347.46	5.77	0.93	0.79
356.94	5.92	0.37	0.36
366.42	6.08	0.03	0.08
375.90	6.24	0.00	0.01
385.38	6.40	0.00	0.00
423.30	7.02	0.00	0.00
461.22	7.65	0.00	0.00
892.56	14.81	0.00	0.00
CNP			
Time (min)	**Time (PV)**	**Observed C/C_0**	**CXTFIT Modeled C/C_0**
0.00	0.00	0.00	0.00
6.18	0.10	0.01	0.00
15.66	0.26	0.00	0.00
25.14	0.42	0.00	0.00
34.62	0.57	0.00	0.00
44.10	0.73	0.01	0.00
53.58	0.89	0.01	0.02
63.06	1.05	0.22	0.17
72.54	1.20	0.52	0.46

82.02	1.36	0.64	0.67
91.50	1.52	0.68	0.75
100.98	1.68	0.73	0.78
110.46	1.83	0.76	0.80
119.94	1.99	0.78	0.81
129.42	2.15	0.79	0.83
138.90	2.30	0.83	0.84
148.38	2.46	0.84	0.85
157.86	2.62	0.86	0.86
167.34	2.78	0.87	0.87
176.82	2.93	0.89	0.88
186.30	3.09	0.88	0.89
195.78	3.25	0.89	0.90
205.26	3.41	0.89	0.91
214.74	3.56	0.91	0.91
224.22	3.72	0.91	0.92
233.70	3.88	0.91	0.93
243.18	4.04	0.92	0.93
252.66	4.19	0.92	0.94
262.14	4.35	0.93	0.94
271.62	4.51	0.94	0.95
281.10	4.66	0.95	0.95
290.58	4.82	0.93	0.95
300.06	4.98	0.92	0.96
309.54	5.14	0.95	0.96
319.02	5.29	0.95	0.96
328.50	5.45	0.95	0.97
337.98	5.61	0.94	0.95
347.46	5.77	0.87	0.79
356.94	5.92	0.53	0.50
366.42	6.08	0.27	0.30
375.90	6.24	0.24	0.23
385.38	6.40	0.20	0.20
394.86	6.55	0.16	0.18
404.34	6.71	0.14	0.17
413.82	6.87	0.11	0.16
423.30	7.02	0.10	0.15
432.78	7.18	0.09	0.13
442.26	7.34	0.08	0.12
451.74	7.50	0.07	0.11
461.22	7.65	0.07	0.11
470.70	7.81	0.07	0.10
480.18	7.97	0.06	0.09
489.66	8.13	0.06	0.08

499.14	8.28	0.05	0.08
508.62	8.44	0.05	0.07
518.10	8.60	0.05	0.07
527.58	8.75	0.04	0.06
537.06	8.91	0.04	0.06
546.54	9.07	0.04	0.05
556.02	9.23	0.04	0.05
565.50	9.38	0.04	0.04
574.98	9.54	0.04	0.04
584.46	9.70	0.03	0.04
612.90	10.17	0.03	0.03
641.34	10.64	0.02	0.02
669.78	11.11	0.02	0.02
698.22	11.59	0.02	0.01
726.66	12.06	0.02	0.01
755.10	12.53	0.02	0.01
783.54	13.00	0.01	0.01
811.98	13.47	0.01	0.01
840.42	13.95	0.01	0.00
868.86	14.42	0.01	0.00
892.56	14.81	0.00	0.00